UNIVERSITÀ DEGLI STUDI DI CATANIA

Dottorato di Ricerca in Scienza e Tecnologia dei Materiali - XXVIII ciclo

Enrica Arcadipane

Titania Nanowires: synthesis, characterization and properties

Tutor: Prof.ssa L. Romano

Coordinatore: Prof.ssa M. G. Grimaldi

Tesi per il conseguimento del titolo

Titania Nanowires: synthesis, characterization and properties

Motivation

Why TiO$_2$ nanostructures for water treatment applications?

Titanium dioxide or titania (TiO$_2$) is a well-known material with increased interest since the pioneering work of Fujishima and Honda in 1972 [1], which demonstrated its advantageous photocatalytic proprieties in water splitting when used in an electrolytic cell under ultraviolet (UV) light. The so-called "Honda–Fujishima effect" represents one of the most important discoveries in chemistry and opened up and extensively promoted the research field of photocatalysis [2].

Titania is an earth abundant material with various advantageous features, such as optimal photo-catalytic properties, reasonable optical and electronic properties, long lifetime of excited electrons, hydrophobicity, non-toxicity, excellent long-term chemical stability, environmental safety, high corrosion resistance and relative low cost [3, 4]. On the other hand, TiO$_2$ has a large band gap (~3 eV) and can absorbs only ultraviolet (UV) light at a wavelength larger than ca. 390nm, corresponding to ca. 3-6% of the solar radiation [2].

Titanium dioxide occurs in three main crystalline phases: rutile (tetragonal), anatase (tetragonal) and brooklite (orthorhombic); among them, rutile appears the most stable one [3]. Rutile and anatase are the most studied phases and they present a bandgap energy of 3 eV and 3.2 eV, respectively. Nowadays, titania is widely applied in many sectors of industry like cosmetic, paints, food, and as a self-cleaning and whitening agent. It has shown particular promise in photovoltaic, chemical sensing, optical devices, and photocatalysis. In this dissertation we will focus on this last aspect, i.e. photocatalysis TiO$_2$, in particular for applications in water purification.

A ''photocatalytic reaction'' or "photocatalysis" can be defined as a chemical reaction induced by photoabsorption of a solid material, or ''photocatalyst,'' which remains unchanged during the reaction.
Nowadays many papers are related to photocatalysis in general since it is now recognized as one of the most important sciences in the development of technologies that can improve the quality of life. Photocatalysis can be applied for the decomposition of volatile organic compounds in water (or air) as much as for the self-cleaning of window glasses and walls. **Fig. 1** illustrates the process of TiO_2 photocatalysis under UV illumination [3].

$$e_{tr}^- + O_2 \rightarrow O_2^{\bullet-}$$
$$e_{tr}^- + H_2O_2 \rightarrow {}^\bullet OH_s + OH^-$$
$$e_{tr}^- + R^\bullet + H^+ \rightarrow RH$$

$$h_{tr}^+ + RH \rightarrow R^\bullet + H^+$$
$$h_{tr}^+ + H_2O \rightarrow {}^\bullet OH_s + H^+$$
$$h_{tr}^+ + O_2^{\bullet-} \rightarrow {}^1O_2$$

• = electron

o = hole
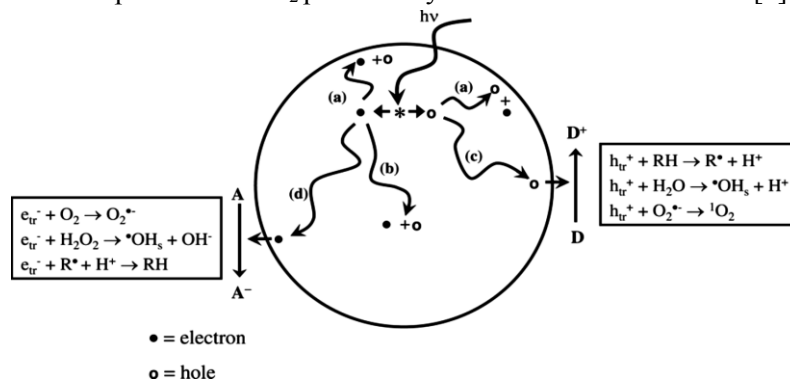
Figure 1 - TiO_2 photocatalysis processes under UV irradiation [3].

When the TiO_2 photocatalyst absorbs a photon with energy equal to or greater than its band-gap, an electron–hole pair is generated; subsequently, the pair is separated into a free electron and a free hole. The electron and hole "walk randomly" to the surface of the photocatalyst and are trapped there; the trapped electron e_{tr}^- and hole h_{tr}^+ react with acceptor (step c) or donor molecules (step d), respectively, or recombine at surface trapping sites (step a). The electron and hole can also be trapped at bulk trapping sites and recombine there with the release of heat (b). **Fig. 1** shows the characteristic surface reactions together with the back-reaction between the oxidized donor and electron, or reduced acceptor and hole, which can occur after the initial charge transfer, especially when the species are strongly adsorbed on the TiO_2 surface. The active intermediate species for titania photocatalytic reactions able to degrade organic matter, are believed to be hydroxyl radical ($^\bullet OH$), superoxide anion radical ($O_2^{\bullet-}$), hydroperoxy radical ($HO_2^\bullet$), hydrogen peroxide (H_2O_2), and singlet oxygen ($^1O_2$), also showed in **fig.1**.

2

Photocatalytic reaction by titania under ultraviolet irradiation in the presence of water (or air) decomposes organic compounds almost completely, i.e. the compounds are mineralized into carbon dioxide (and water). This high photocatalytic power is related to the high oxidation ability of the positive holes photoexcited in TiO_2 [2]. Considering the position of the
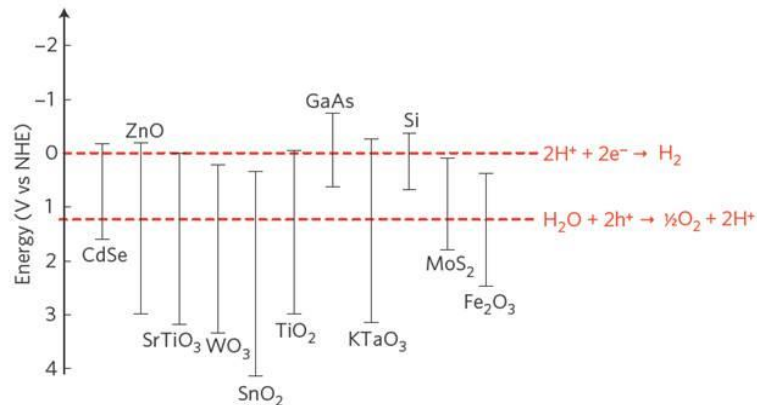
Figure 2 - Position of energy bands of various semiconductors on a potential scale (V) versus the normal hydrogen electrode (NHE) [5].

top of the valence band of titania, ca. 3V vs. NHE (Normal Hydrogen Electrode at pH 0) as showed in **fig. 2**, the potential of positive holes seems far more positive than that for oxidation of ordinary organic compounds. However, this is not the case for titania only, because all metal oxides have essentially the same oxidation ability (i.e. the same potential of the top of the valence band), since the valence bands of metal oxides are mainly composed of the same O 2p atomic orbitals; while the potential of the conduction band varies depending on the kind of metal. One of the possible reasons for the high activity of titania compared with that of other metal oxides is the high reduction ability to inject photoexcited electrons into molecular oxygen adsorbed on the surface of photocatalysts [2]. Since photocatalytic reactions must be completed with consumption of the same numbers of electrons and positive holes, even if the potential of the holes is sufficiently high, cannot be utilized when photoexcited electrons are not consumed. Among the various metal oxides, titania has a relatively high ability of reduction of oxygen under photoirradiation. In this sense, a plausible explanation is that

titania has sufficient ability for electron utilization to drive oxidation by positive holes (or intermediate species produced by them) of high oxidation ability, and other metal oxides with low photocatalytic activity may have low reduction ability even though they also have high oxidation ability [2].

Concerning the share of solar radiation absorbed by titania previously mentioned (3-6%), it is important to notice that the calculation has been made on the basis of energy of light, not on the basis of number of photons. In fact, regarding the energy conversion efficiency (e.g. for solar cells), content of light should be discussed on the basis of energy. Whereas, for photocatalytic reactions, which mostly do not convert energy (with some exceptions as for the photosplitting of water into hydrogen and oxygen), the content of light of the related wavelength region should be calculated on the basis of photon numbers. Thus, the energy conversion efficiency cannot be discussed and, instead, quantum efficiency becomes significant. Hence, since energy of a photon in the ultraviolet light region is larger than that in the visible light and infrared light regions, the portion of solar radiation calculated on the basis of number of photons must be much smaller than 3–6%[2], as depicted in **fig. 3.**

Solar spectrum plotted as photoirradiance and as photon flux. In photocatalysis (not applied for energy conversion), the relevant quantity is photon flux instead of energy, so the share of solar spectrum in the UV range <1% instead of 3-6% because UV photons have high energy.

Figure 3 - Solar spectrum plotted as photoirradiance and as photon flux. In photocatalysis (not applied for energy conversion), the relevant quantity is photon flux instead of energy, so the share of solar spectrum in the UV range <1% instead of 3-6% because UV photons have high energy.
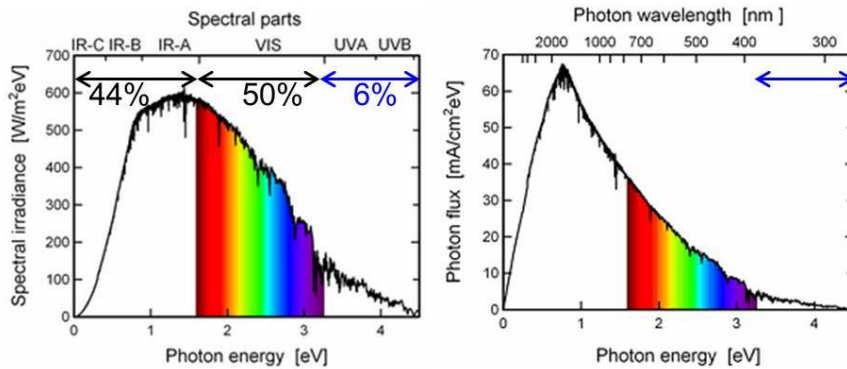
4

The photocatalytic reactions illustrated before, are surface mechanisms that strongly depend on the surface in contact with water (or air). Larger is the surface, higher will be the number of photocatalytic processes and hence the degradation reactions occurring. This is the main driving motivation underlying the broad studies and synthesis of nanostructures on the titania surface which can improve the photocatalytic final efficiency. In this sense, we also addressed the study presented in this dissertation, particulary focusing on nanowires structures.

Nanostructures are defined as having at least on dimension between 1 and 100nm. A nanowire is a wire shaped object whose radial dimension is in the nanometer regime. Nanowire is used extensively in this document and therefore will abbreviated NW. The plural form, nanowires, will be abbreviated NWs. It is worth to notice that the TiO_2 NWs we are dealing with, have minimum sizes of tens of nm in diameter and hundreds of nm in length. Therefore, they do not show bandgap variation due to the quantum–size effect, since the Bohr radius for anatase and that for rutile nanostructures have been estimated to be 2.5 and 0.3 nm, respectively [6]. Indeed, the quatum–size effect is the expansion of the band gap (i.e. a blue shift) obtained when the size of the nanostructures is smaller than its Bohr radius. Titania nanostructures claimed in papers to show a quantum-size effect might be larger than these sizes, since the synthesis of such small nanostructure is very difficult. A blue (shorter wavelength) shift, if observed, of the absorption edge of those samples might be due to the amorphous part of titania, not to the quantum-size effect. At least for TiO_2 photocatalyst, use of quantum-size effect for interpreting the results seems inappropriate [2].

The NWs structure can have also further advantages such as the fact that can be used to create nano-membranes (**fig. 4**) that can be applied both for water filtration and purification [7,8]. For instance, the ultrafiltration membrane made of TiO_2 NWs reported in **fig.4** has pore size of ca. 20nm, therefore it should be able to filtrate even bacteria cells (typical size from 0.5 to 5 μm) and virus cells (size from 50 nm onwards). In addition to the filtration mechanism, the membranes have proved to have also a good degradation effect (**fig. 5**): *E.coli* bacteria in aqueous medium was effectively filtered by the membrane which was afterward irradiated by UV
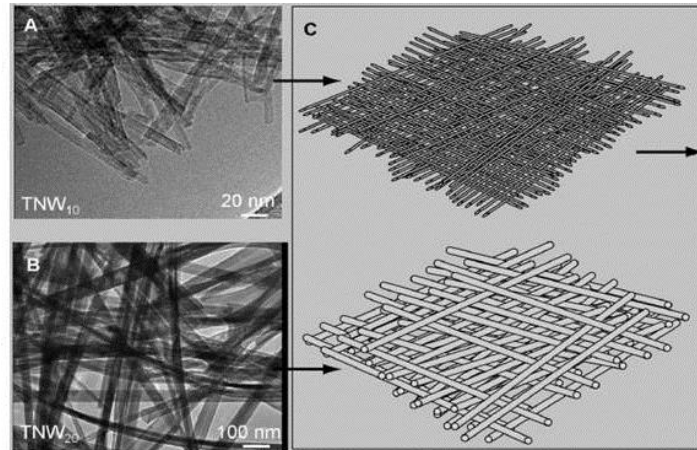
Figure 4 - TiO$_2$ ultrafiltration nanomembranes fabricated from TiO$_2$ NWs [7].

light showing a destruction of more than 99.9% of the E.coli colonies after 60 min of UV light exposure (plot on the left of **fig. 5) [7]**. Similarly, nanomembrane made of TiO$_2$ NWs was reported to degrade efficiently pharmaceutical pollutant, such as the trimethoprim (plot on the right of **fig. 5)** which also strongly decreased its concentration after 60 min of UV irradiation in contanct with the titania membrane (blue square) which displayed even a better degradation effect compared to the well known commercially available P25 TiO$_2$ nanoparticles [8].
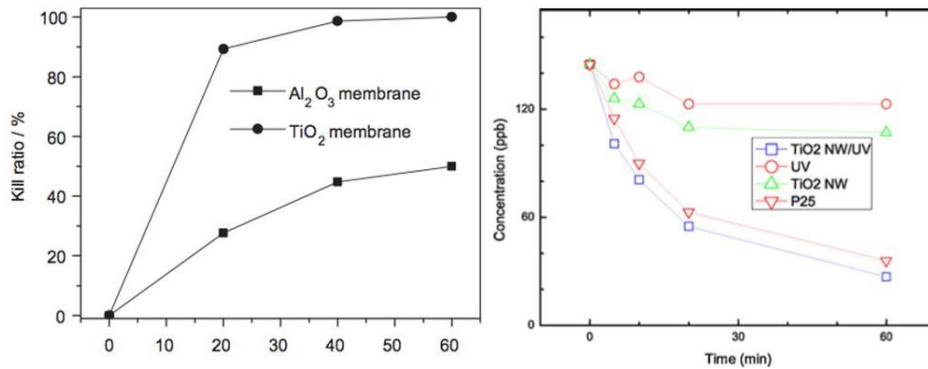
Figure 5 - Inactivation of *E. coli* bacteria by a TiO$_2$ NW ultrafiltration membrane [7] (left) and degradation of a pharmaceutical pollutant, the trimethoprim, by another TiO$_2$ membrane [8] (right), as a function of the time exposure to UV light.

In the followings chapters of this dissertation, we will report on the synthesis, modification and characterization of TiO_2 NWs. First, in Chapter 1 we will review different methods of TiO_2 NWs fabrication with a critical discussion on the actual processes underlying various methods, trying to shed some light on the detailed definitions of some mechanism as the well-known VLS (Vapour-Liquid-Solid) and seed assisted oxidation.

In chapter 2, we report an extended experimental work performed on NWs synthesis, carried out by seed assisted thermal growth, varying temperature, annealing duration, gas content and flow during the annealing in order to investigates and determine the process conditions, which optimize the NWs production in terms of NWs length, density and structure. Morphological characterization by Scanning Electron Microscopy (SEM) and Transmission Electron Microscopy (TEM) was performed on the synthetized TiO_2 NWs samples. The structural characterization was carried out by X-Ray diffraction (XRD) technique. Moreover, we employed a SEM with *in-situ* annealing to study the evolution of the NWs formation and to understand their growth dynamics as a function of temperature and time.

In order to improve the performance of TiO_2 NWs, we modified the samples applying two approach described in chapter 3: doping of the NWs by Ion Implantation of Fe ions; and annealing in forming gas (N_2 and H_2 at 5%). In particular, the samples processed in forming gas were performed in order to investigate the produced effect on TiO_2 electrical properties. Indeed, it has been reported [9,10] that an atmosphere of H_2 in N_2 can increase the photoefficiency of TiO_2 by the formation of oxygen vacancies, which increase the donor density, promoting the conductivity and improving the charge collection. Therefore, the study of the energy defects present on the nanostructures appeared crucial. Hence, we performed electrical characterization of the TiO_2 NWs illustrated in Chapetr 4, by using the very powerful technique of Deep Level Transient Spectroscopy (DLTS), which allowed us to identify the defects energy levels within the bandgap of the sample. Finally, Chapetr 5 reports the photocatalytic activity of the NWs investigated by using the dye degradation method of methylene blue following the ISO 10678:2010 standard protocol. The dissertation will be concluded by a final sum up of the main results of the work, significant comments and outlook for the next challenge of this research field.

References

[1] Fujishima A. and Honda K., Nature 238 (1972) 37-38.

[2] Ohtani B., Chem. Lett. 37, 3 (2008)

[3] Fujishima A., Zhang X., Tryk D. A., Surf. Sci. Rep. 63 (2008) 515-82.

[4] Chen X., Mao S. S., Chem. Rev. 107 (2007) 2891.

[5] Linic S., Christopher P. and Ingram D. B., Nature Mater. 10 (2011) 911.

[6] Y. Nosaka, A. Nosaka, Nyumon Hikarishokubai (Japanese), Tokyo Tosho, Tokyo, 2004, p. 59

[7] X. Zhang, T. Zhang, J. Ng and D.D. Sun, Adv. Funct. Mater. 19 (2009) 3731.

[8] A. Hu, X. Zhang, K. D. Oakes, P. Peng, Y. N. Zhou, M. R. Servos, J. Hazard. Mater. 189 (2011) 278.

[9] C. Fàbrega, T. Andreu, F. Guell, J.D. Prades, S. Estradé, J.M. Rebled, F. Peirò and J.R. Morante, Nanotechnology, 22 (2011) 235403.

[10] G. Wang, H. Wang, Y. Ling, Y. Tang, X. Yang, R. C. Fitzmorris, C. Wang, J. Z. Zhang and Y. Li, Nano Lett., 11 (2011) 3026-3033.

Chapter 1

How nanowires grow

Over the past two decades, great effort has been directed toward the synthesis of one-dimensional (1D) materials, whose unique chemical/physical properties can potentially be exploited in various fields.
The most successful example is provided by microelectronics, where "smaller" has meant greater performance ever since the invention of integrated circuits: more components per chip, faster operation, lower cost, and less power consumption.Synthesis of nanostructures has been carried out by means of many different techniques that can be divided considering two main approaches: top-down and bottom-up. The main methodologies for NWs growth are reviewed in the first section, while the second section is dedicated to the main topic of this dissertation: the thermal synthesis of titania nanowires on Ti foil substrate.

1.1 Top-down approach

The top-down approach is capable of producing NWs or any other nanostructure using the same techniques commonly employed in the production of microelectronic devices, such as atomic force microscopy (AFM), selective chemical etching and electron beam lithography [1, 2]. L. Francioso and P. Siciliano reported on the fabrication of TiO_2 NWs (with section of 90 - 180 nm and length of 1.4 mm) by a 365 nm UV photolithography from a TiO_2 thin film deposited on a silicon oxide substrate [2]. Some advantages of the top-down approach include:
- the accurate control of diameter and length of the nanostructures, i.e. the fabrication of 'tuned structures';

- the techniques involved are well established and understood;
- complex nanostructured patterns can be developed and used.

However, many of these techniques come with various drawbacks such as:

- the need of highly trained personnel;
- the use of very expensive equipment;
- the limitation of the employed materials for nanostructure production to those used in the microfabrication industry;
- the size scale limitation due, for instance, to the resolution of the lithography technique;
- the complexity of the procedures typically involved in these processes.

Because of these limitations, the wide spread implementation of lithography as a means of producing 1-D structures has been slow.

Instead, much of the focus has been on the production of 1-D nanostructured materials by the bottom-up approach.

1.2 Bottom-up approach

This section will trace the development of general models for understanding seed particle assisted growth, from early examples (of one-dimensional structures on the microscale) through to the most recent attempts to formulate a general understanding of these growth processes. One of the primary difficulties in understanding this technique is the incredible variety of materials, parameters and growth systems that are used to produce remarkably similar nanowire structures. This has required constant refinements and reconsiderations of growth models and the variety of data available increases. However, there remain significant areas of controversy, and conflicting models and results. [3].

Since Au catalyzed Si NWs growth is one of the most studied system, we will discuss it as a special model and some general conclusions will be drawn. It is useful to consider the thermodynamics of the crystal growth. For any reaction to occur, the chemical potential of certain components (reactants), must be greater than that of other components (products), in other words, a supersaturation must exist. The difference in chemical potential is the driving force for the reaction; kinetic factors may

determine the rate at which the reaction occurs. As the reaction approaches equilibrium, the chemical potential difference approaches zero, and the reaction stops. If, however, a constant supply of reactant is maintained, the reaction can proceed continuously under steady-state conditions.

Considering the case of Au assisted Si NWs growth, in order for Si to dissolve in the Au particle (that is, for binary liquid Au-Si to form), the chemical potential of the particle must at all times be lower than the surrounding vapour. However, the chemical potential of the particle must also eventually exceed that of the crystalline Si, so that this material forms by precipitation from the particle. This would lead to the conclusion that the chemical potential of the Au particle lies between that of the Si supply and the Si crystal being grown. However, since the chemical potential difference between the vapour and crystal would then be greater than the difference between the particle and crystal, this would lead to the conclusion that growth from the particle would be slower than growth from the vapour.

Clearly, such thermodynamic arguments are insufficient to explain the growth of whiskers from seed particles, and kinetics must be considered. Under equilibrium or stable steady state conditions, compositions can be considered to be uniform everywhere. However, physical processes like diffusion also occur in growth systems, and these occur at a finite rate that can lead to inhomogeneity in the materials in the system.

As described above, a local increase in the concentration of Si around the Au particle could lead to an enhanced growth rate near the particle surface. A simple possibility would be that the Au particles act as catalysts for precursor decomposition. A catalyst is a material that increases the rate of a reaction by lowering the activation barrier by changing the pathway by which it occurs without itself being consumed by the reaction. Catalyst materials react with the material being decomposed, but are then re-formed by secondary reactions and can thus react continuously with new material. If the reaction between the catalyst and the material being decomposed (the precursors in this case) has a lower activation energy than the decomposition without the catalyst, then the overall decomposition rate will increase.

1.2.1 - VLS method

Of the vapour phase growth methods, the VLS method is the most widely used and best understood. In general, a vaporized source material is introduced into a reaction chamber and flown by a carrier gas downstream. As this vaporized constituent deposits on a substrate surface also placed into the chamber, there must be a means of confining the deposition to limited surface locations for the process to produce nanostructures. Otherwise, only a uniform film would develop. One of the most successful ways to provide this confinement is through the use of a liquid metal catalyst, which is the basis of the VLS mechanism. A catalyst in the liquid phase, typically a metal, provides preferential deposition sites for the vaporized source material and gives the chemical adsorption confinement required for one dimensional growth [4].

With VLS, liquid droplets are formed by eutectic reactions between a source material and the catalyst. The liquid droplets have a finite solubility of the vaporized source material thus providing favourable sites for the adsorption on the surface and subsequent absorption into the catalyst droplet. Once this solubility limit is exceeded, the source material adsorbed on the droplet diffuses to the liquid-solid interface of the substrate creating nucleation sites for the 1-D growth of the nanostructures [4]. The confinement is provided by the enhanced adsorption and diffusion of the vapour species on and into liquid catalyst. This allows for a higher reaction rate of the nanostructure forming constituents at the liquid droplet than that of the surrounding area, resulting in the confinement of growth to one dimension. Upon cooling, the liquid catalyst solidifies, producing a cap on the tip of the nanostructure. The presence of this cap is the typical feature of the VLS mechanism. There have been a variety of nanomaterials with various morphologies produced by this technique, including TiO_2 [5, 6].

An example of one such structure, as presented by Wagner and Ellis who first reported the VLS mechanism in 1964, is Si nanowhiskers grown using Au as the catalyst. For this experiment, a small particle of Au was placed on a (111) silicon substrate. It was subsequently heated to 950°C where a liquid droplet of Si-Au formed (**Fig. 1.1 a**).

A gas mixture of H_2 and $SiCl_4$ was flown over the sample. The Si-Au liquid droplet allows for preferential adsorption of Si in the vapor phase. Once the alloy droplet reaches the saturation limit for Si, the Si solidifies at the droplet-substrate interface. As this process progresses, the Si-Au droplet is pushed up by the growing Si single crystal nanowhisker (**Fig. 1.1 b**). This process continues until either no more Si remains in the vapor phase [4].

However, Wagner et al. were able to demonstrate that the activation energy for the growth of their whiskers with Au particles was the same as that for growth of Si without Au [7]. This effectively suggested that Au was not catalytic in their system (although they did not state this explicitly). This led them to conclude that another process was leading to an increased local concentration at the surface of their particles, which they deemed an
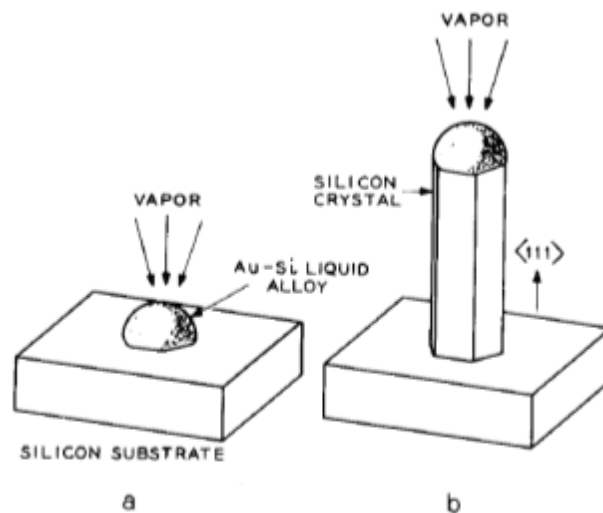

Figure 1.1 – Illustration of Si NWs growth by VLS process: first at the sites where there are the metal catalyst (Au) drops, an Au-Si alloy is formed (a); then, the nanowire start growing below the metallic alloy cap (b) [4].

enhanced accommodation probability of the liquid. In principle, an ideal liquid surface captures all impinging Si source atoms, while a solid surface of Si rejects almost all Si source atoms if the temperature is sufficiently high. In other words, kinetic surface processes were limiting in their model. It is not clear whether it is generally true that liquid surfaces have a higher accommodation coefficient than solid surfaces [8]. Nevertheless, it is still often assumed that the growth of Si nanowires occurs due to an enhanced concentration of Si that exceeds its solubility limit in the liquid alloy. The growth of compound nanowires, on the other hand, is complex and more difficult to understand than Si. The ratio of these two materials influences the growth, as the chemical potential difference between the vapour and crystal is determined by both materials. The thermodynamics is more complex and causes significant difficulty in defining a practical assessment. Another important question is whether the alloy particle must contain both materials for growth to be possible. Many binary compound materials (including many oxides, nitrides, and phosphides) do not form continuously miscible ternary liquid alloys with normal seed particle materials (typically transition metals, most often Au). Local eutectic points exist between several adjacent compounds, and supersaturated liquid alloys in these composition ranges could be made to precipitate different compounds. For this, ternary phase diagrams need to be used. Unfortunately, the number of potential ternary systems is enormous, and investigation of each requires detailed study over a four-dimensional parameter space (involving pressure, temperature, and two relative material compositions). Consequently, the amount of information on the relevant ternary systems is very limited, and it is difficult to predict or interpret nanowire growth based on this data.

The initial period before uniform growth commences is associated with any of a number of processes. In some cases, the catalytic particles must be formed by vapor phase and/or surface diffusion transport or else their surfaces have to be cleansed of impurities (oxides or terminating thiols). The particles may be deposited directly, for instance, from the evaporation of a colloidal solution with a well-defined size. Alternatively, a thin film of metal can be evaporated directly onto a substrate and if the metal does not wet the substrate, it will ball up into islands either immediately as the result of Volmer–Weber growth [9] or else subsequently when the

14

system is annealed, the onset of Ostwald ripening [9] will lead to a distribution of island sizes. For instance, the catalytic particle can lower the barrier that is present for the incorporation of new material at the growth interface as compared to the nucleation of an island on a sidewall or the substrate.

Fig. 1.2a and **b** also illustrate several dynamical process that can affect growth. Adsorption occurs from the fluid (whether gaseous, liquid or supercritical) phase. Adsorption might be molecular or dissociative and may either occur (vii) on the nanowire (viii) on the particle, (ix) on the substrate. A natural way for the catalytic particle to direct material to the growth interface is if the sticking coefficient (probability of adsorption) is higher on the particle and vanishingly small elsewhere. Diffusion of adatoms will occur (i) across the substrate (if the sticking probability is not negligible), (ii) across the particle and (iii) along the sidewalls. Diffusion across the substrate and along the sidewalls must be rapid and cannot lead to nucleation events.
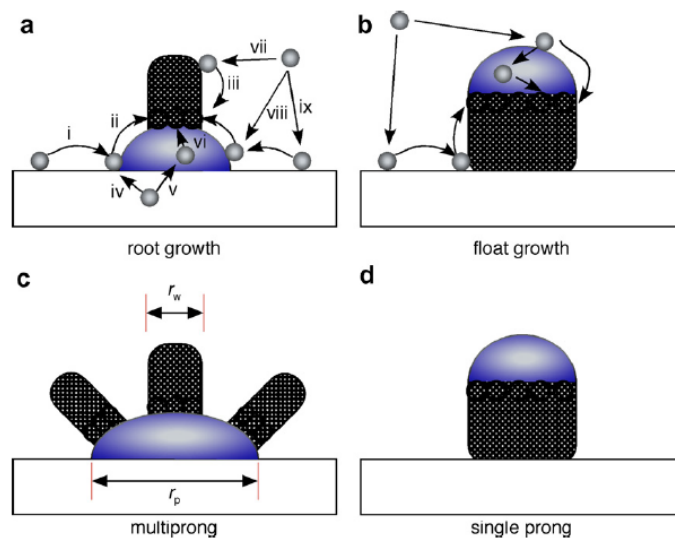
Figure 1.2 – The processes that occur during catalytic growth. (a) In root growth, the particle stays at the bottom of the nanowire. (b) In float growth, the particle remains at the top of the nanowire. (c) In multiple prong growth, more than one nanowire grows from one particle and the nanowires must necessarily have a smaller radius than the particle. (d) In single-prong growth, one nanowire corresponds to one particle. One of the surest signs of this mode is that the particle and nanowire have very similar radii. [8]

1.2.2 – Growth models of seed assisted growth

The actual role of the particle is still very much under debate. It appears that the driving force for the enhanced growth (compared to bulk semiconductor growth) is still an open question, since it has not been possible to explain it using thermodynamics or chemical reaction kinetics.

It should be emphasized that one-dimensional growth proceeds simply because growth in one direction is much faster than all others; the particle-wire interface is typically treated as a sink for material. Wagner and Ellis concluded in 1964 that the Au particles at the tips of their Si whiskers were in fact binary liquid AuSi alloy particles during growth. This conclusion was partly reached due to the shape of their particles, which were rounded with a hemispherical or truncated spherical shape. Additionally, the AuSi binary system exhibits a low-temperature eutectic (far below their growth temperatures), and growth at temperatures above this eutectic point could allow for precipitation of solid Si from a supersaturated liquid alloy.

More recently, observations of small particles at the tips of nanowires have often led to the conclusion that liquid alloy particles act as seeds for the growth of these wires by a mechanism similar to Wagner's VLS. However, in some cases the possible existence of such a liquid alloy has not been carefully considered. The state of the particle is an important question to answer, since many models of particle-assisted growth depend on the liquid phase of the particle. Determining whether the existence of this phase is universal will determine the validity of such models. An important point is that nanoparticles do not necessarily behave in the same way as bulk materials. The melting point of small nanoparticles has been investigated by many groups, all of which observed a strong depression in melting temperature at very small sizes. For Au, slight melting point depression occurs for particle diameters below about 20 nm; when particle diameters decrease below 5 nm, the melting points decrease very rapidly [10, 11]. As well, even solid Au nanoparticles have been shown to reshape at temperatures as low as 200 °C to form equilibrium shapes, without losing their crystal structure [12].

In other words, the mobility of atoms in small solid particles is high, and the distinction between solid and liquid particles is not always as clear.

16

Moreover, the mobility of atoms on the surface is typically much higher than within the bulk, and some degree of ''surface melting'' may occur in other solid particles with high curvature (in other words, very small diameter). Kamins et al. demonstrated in 2001 that Si nanowires can be grown from solid TiSi 650 K below the eutectic temperature [13], and the possibility of VSS growth (including the term) was first suggested 35 years ago by Bootsma et al. [14].

"Liquid or solid?": the problem with most investigations on this subject was that detailed structural analyses, for example, with electron diffraction methods, could only be performed after the growth had terminated, leading to additional uncertainties. Kodambaka et al. [15] investigated the growth of gold-catalyzed germanium nanowires in situ in a transmission electron microscope that allows for the supply of germanium vapor in the form of Ge_2H_6 gas. For the gold-germanium system, several reports have suggested nanowire growth below the eutectic temperature [14, 16]. A key indicator was the shape of the gold at the tip of the nanowire. A liquid gold droplet has a smooth, almost halfspherical shape, whereas solid gold shows planes, edges, and corners that may easily be identified. The mechanism by which Ge nanowires grow may depend not only on the temperature but also on the diameter of the nanowire (see **Fig. 1.3**). Above eutectic temperature T_E (left of **Fig. 1.3**), the nanowires have a liquid gold cap and grow via VLS growth.
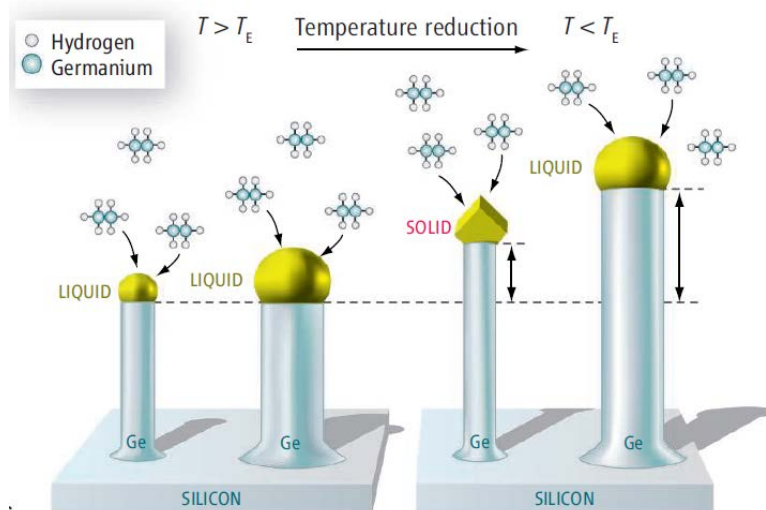
Figure 1.3 - Germanium nanowires. The mechanism by which Ge nanowires grow may depend not only on the temperature but also on the diameter of the nanowire, as shown by Kodambaka et al. Above T_E (left), the nanowires have a liquid gold cap and grow via VLS growth. Below T_E (right), the cap of relatively thick nanowires is liquid, whereas the cap of relatively thin nanowires becomes a crystalline solid. The latter nanowires grow via a different mechanism that is slower than VLS growth. [17]

17

Below T_E (right of **Fig. 1.3**), the cap of relatively thick nanowires is liquid, whereas the cap of relatively thin nanowires becomes a crystalline solid. The latter nanowires grow via a different mechanism that is slower than VLS growth.

The experiments of Kodambaka et al. clearly demonstrate that— even well below the eutectic temperature—the gold catalyst droplet can remain liquid, corresponding to VLS growth, and that solid gold particles can also catalyze nanowire growth. VLS and VSS are both very similar and entirely valid mechanisms. It may in the future be possible to describe these by a single model, without explicit reference to the state of the seed particle. Nanowire growth below the bulk eutectic temperature for the seed particle with the growth material has been reported for very many systems. Examples include Si nanowires with Cu particles [18,19], Si with Al [20], Si with PtSi [21], Ge nanowires with Au particles [22, 16], Si and Ge nanowires with Ni [23,24], GaN with Ni particles [25], ZnSe with Fe [26] and with Au [27], ZnO with Au [28] and GaAs with Fe particles [29].

Amorphous silicon nanowires a-SiNW with an average diameter of ca. 20 nm were synthesized at about 950°C under an Ar-H_2 atmosphere on a large area of a <111> Si substrate without supplying any gaseous or liquid Si sources. Under the present conditions, however, the Si concentration in the vapor phase is negligible at the growth temperature because the specific surface/volume ratio of bulk Si substrate is extremely low compared with that of the micro-sized Si powder target (powder can be a source material by using a furnce with temperature gradient where the substrate is located downstream at lower T with respect of the source, see section 1.4 for details), or in the case of laser ablation. On the other hand, the Si substrate was covered by a thin layer of Ni. Therefore, the only possible silicon source comes from the bulk silicon substrate because no extra Si source was introduced into the vapor phase.

Ni thin Film on Si (111)

(a)

Formation of Si-Ni liquid droplets

(b)

(c)

(d)
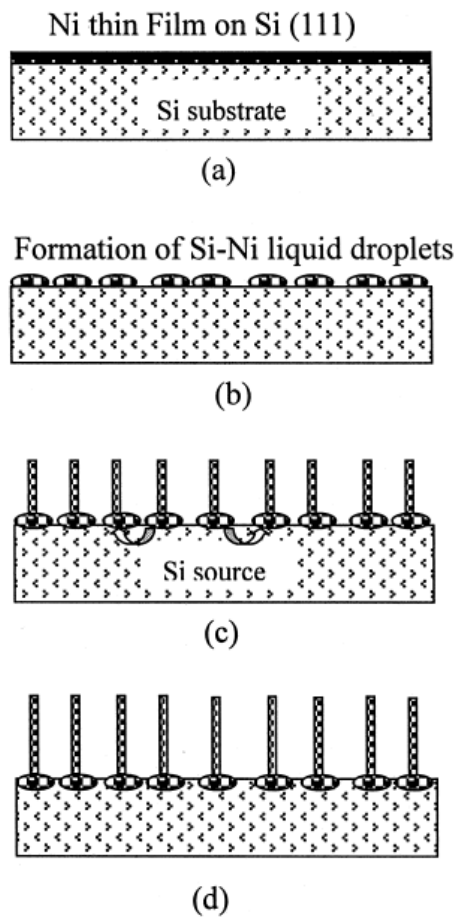
Figure 1.4 - Schematic depiction of SiNW growth by the SLS mechanism: a. deposition of a thin layer of Ni on the Si 111. substrate; b. formation of the Si–Ni eutectic liquid droplets; c. continuous diffusion of Si atoms through the substrate–liquid SL. Interface into the liquid droplets, and growth of SiNWs through the liquid–wire LS. interface; d. final state of SiNW growth. The smooth surface of the original substrate becomes rough at the end of SiNW growth. [30]

Whether a base or a top growth depend on the wetting condition between the catalyst droplets and the substrate. If the wetting is very good, the interaction force between the catalyst droplets and the substrate can be very strong and the nanoparticles will stay at the substrate as a base growth; otherwise if the wetting is bad, a top growth will work. [31]

Wang et al. [32] have shown that in some cases the nanowire growth may be controlled by surface diffusion. In their diffusion-induced VLS model, molecules in the vapor phase are considered to first fall on the liquid surface and then diffuse along the surface to the LS interface and finally incorporate into the solid wire (see **Fig. 1.5**b).
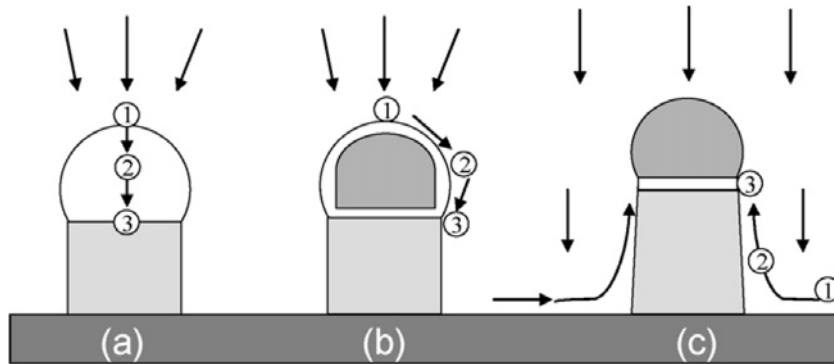

Figure 1.5 – Different diffusion models for the source atoms to incorporate into the growth front of the nanowire. (a) The classical VLS. (b) The metal droplet is in partially molten state. Its surface and interface are liquid, while the core of the droplet is solid. (c) The metal catalyst is solid, but the interface is liquid.[32]

The surface diffusion model becomes important for the growth at a low temperature. In addition to the direct impinging atoms, the source atoms may also arrive at the droplet by diffusion along the substrate surface and wire side surfaces (**Fig. 1.5**c). Nanowires formed by this model usually show tapering shape at their roots. At a relatively high growth temperature, however, this growth model should be inhibited because no adatom can stay at solid surfaces.

It should be pointed out that it is not only the seed particle that can exist in different states; numerous related mechanisms have been reported in which one of the states of the VLS systems is replaced with another phase. These ''VLS-like mechanisms'' include for examples: solution-liquid-solid (SLS) [33], where the growth medium is replaced by a liquid solution, solid-liquid-solid (SLS again) [34], supercritical fluid-liquid-solid (SFLS) [35], supercritical fluid-solid-solid (SFSS) [23].

Experimental observations and assessment of thermodynamic data have been used to explain the Solid-Vapor-Liquid-Solid (SVLS) mechanism for the growth of silica nanowires. The binary phase diagram of nanoparticle (Au-Si) systems has been evaluated from information on Gibbs energy of the bulk and surface tension of the liquid phase. At 1100 °C, temperature commonly used for the growth of nanowires by the SVLS mechanism, it has been shown that the nanometric decreases the melting point of pure Au and Si and more generally the liquidus temperatures. Moreover, the liquid phase region in the binary Au-Si phase diagram is enlarged as the particle size becomes smaller. The presence of SiO in the gaseous phase is a necessary but not sufficient condition for the formation of nanowires. The nanowires growth cannot be explained by the modification of the Au-Si phase diagram with the size of the particles, neither by the presence of SiO, but by the existence of a metastable equilibrium involving the silicon of the wafer, the deposit of vitreous silica and supersaturated SiO in the gaseous phase. [36]. From the thermodynamic point of view, the Solid-Liquid- Solid (SLS) mechanism involved in the growth of silicon nanowires is shown to be the net result of two consecutive reactions. The production of SiO by reacting an amorphous SiO_2 coating with the silicon of the wafer followed by the disproportionation reaction $2SiO \rightarrow SiO_2 + Si$ resulting in the formation of Si-SiO_2 nanowires. SiO will decompose on the surface of the Au droplets and silicon will dissolve until the liquid-gas equilibrium is reached. When the liquid is in equilibrium with the gaseous phase but supersaturated in silicon with respect to the wafer, the precipitation of silicon nanowires will be observed.

Although a fully-developed, universally-accepted explanation for nanowire growth from alloys or non-alloying elements has not yet been described, there are very interesting proposals that the main driving force for one-dimensional growth is the preferential nucleation of material at the particle/crystal interface, compared to elsewhere on the crystalline surface [8]. In other words, nucleation is kinetically hindered on the substrate and wire side facets, but the particle-wire interface acts as a sink. This means that the phase of the seed particle is less crucial than previously assumed in order to generate a nanowire. What these works have in common is emphasis on the boundary between the particle, wire and supply phase (that is, the perimeter of the base of the particle) as a preferential site for nucleation. Step flow then occurs across the interface, followed by an additional nucleation event. There is in fact support for the argument that the three-phase interface is in fact the lowest-energy nucleation site. The work of Sear uses Monte Carlo simulations involving classical nucleation theory to explain that heterogeneous nucleation of ice from water droplets on solid particles (of a foreign material) occurs at a much higher rate at the three-phase line between the liquid water, water vapour and solid particle [37]. This model is in fact not specific to water, but is intended to be general description of crystal nucleation. The details of the treatments of preferential nucleation in particle-assisted nanowire systems vary. Cheyssac et al. emphasize this boundary as the point of minimum curvature, where mobility is lowest and thus nucleation highest [38]. This creates a diffusion gradient of material towards the boundary, either through the particle or along the surface (or both). Their approach emphasizes surface mobility of atoms on highly curved surfaces, suggesting the possibility of liquid-like surfaces on otherwise solid particles. The approach of Nebol'sin and Shchetinin considers the change in surface energies of the particle and wire that occur when nucleation occurs at the three-phase boundary [39]. They propose that there is an increase in the surface Gibbs free energy when the liquid particle is displaced by formation of a solid nucleus for a given range of particle-wire contact angles. This depends on the assumption that the surface energy of the solid is not high compared to the liquid; for material combinations for which this requirement does not hold, wire (whisker) growth is not possible. This approach explicitly considers a liquid particle,

22

but may still apply to certain solid material combinations. The work of Glas et al. follows a somewhat similar approach, emphasizing the energy gain that can be expected when a nucleus forms at the edge of the particle-wire interface [40]. However, this work emphasizes the difference between nucleation at the three-phase boundary and nucleation in the centre of the particle-wire interface. The aim here is simply to demonstrate the favourable position for nucleation, given the assumption that nucleation will occur at the particle surface. It is explicitly stated in this work that the model does not depend on a particular state for the seed particle; it should also not depend on the state of the supply. Wacaser emphasizes the point that the three-phase boundary can be treated as ideally ''rough'', making it an ideal site for nucleation [41]. Essentially, this approach treats the boundary as a kink site where incorporation of an atom is more likely than at any other position. As well, they suggest that the supersaturation should be higher at this interface than elsewhere in the system, increasing the local growth rate. Here again, the nature of the particle and the supply phase are not specified, and the model is intended to be general.

1.2.3 – Growth without seeds

Without the aid of metal catalysts, the vapor–solid (VS) growth has been mainly used to synthesize metal oxide and some semiconductor nanomaterials. It is often called selfcatalytic growth since the nanostructures grow directly from vapor phases. Plausible growth mechanisms such as the anisotropic growth, defect-induced growth (e.g., through a screw dislocation), and self-catalytic growth have been suggested based on electron microscopy studies.

The vapor solid (VS) mechanism has been used to explain many of the NWs growth in which the main constituent of the resulting nanostructure exists in the vapor phase but no liquid phase catalyst is present.

The main source of confinement to 1-D growth for this process is considered to originate from the substrate defects. However, the VS growth mechanisms is not yet deeply understood. Many theories have been developed to explain this 1-D mechanism growth without the use of a liquid catalyst, which attributed to the VS mechanism, including:

- dislocation driven growth, ascribed to the presence of screw dislocations intersecting the crystal surface of the substrate **[**42-46**]** (see **Fig. 1.6**);
- stress/strain induced growth, attributed to the accumulation of atoms due to a stress gradient [47-49];
- growth induced by reactive nanocrystalline seeds formed from the decomposition of an adsorbed precursor on a reactive oxide layer [50, 51];
- vapor phase condensation, in which nanostructures are formed in the gas phase and afterwards they condensate on the substrate [52.]
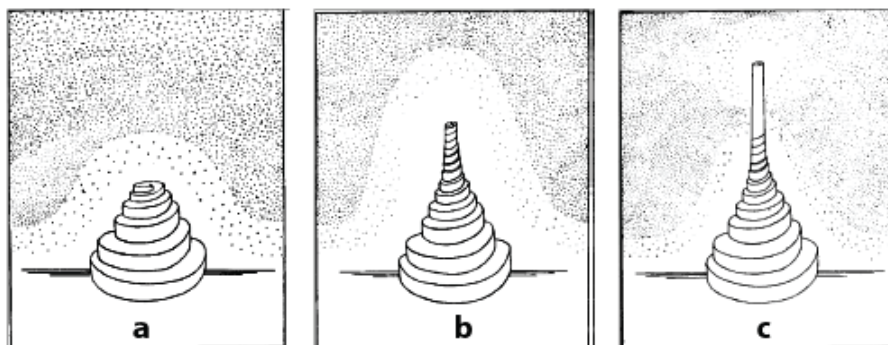

Figure 1.6 – Diagram of a screw dislocation driven growth mechanism [VS5]: the species in the gas phase deposit at the dislocation step forming a growth cone (a); as the summit of the cone rises, diffusion at the top is faster versus the base (b); next, the cone reaches the stage of having a columnar summit.

1.3 – TiO₂ Nanowires by solution growth methods

Several methods employing the bottom-up approach have been developed. They can involve a gas phase reaction of a vapor species and a substrate or can occur in solution. The desired end application often dictates which process is best suited for the production of nanostructures.
Sol – gel method is widely applied to synthetize ceramics materials. It consists of using a sol (a dispersion of solid in liquid) to obtain a gel (a dispersion of liquid in solid); a further calcination and drying steps can produce a solid final phase. The sol-gel process is characterized by hydrolysis and condensation reactions using as precursor typically inorganic metal salts or metal organic compounds. For the synthesis of TiO_2

nanostructures titanium precursors are used such as titanium (IV) alkoxide, and titanium tetraisopropoxide (TTIP). For instance a colloidal suspension containing TTIP can be deposited by electrophoresis in an anodic alumina membrane (AAM) with long pores; dissolving the AAM template with NaOH solution, TiO_2 nanowires are obtained [53] as reported in **Fig. 1.7**.
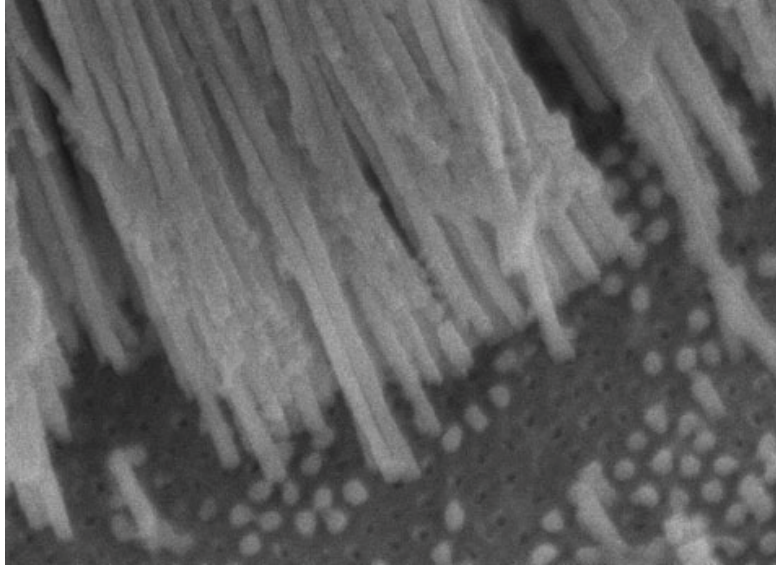

Figure 1.7 - Nanowires synthetized by sol-gel electrophoresis using a template of porous AAM [53].

A wide spread method of TiO_2 nanowires synthesis is the hydrothermal process. It based on reactions with a Ti precursor in aqueous solution in a pressure vessel (i.e. an autoclave) [54-60]. Most of the works use TiO_2 white powders in NaOH or KOH solution kept a temperature around 100-200°C for 1 to 7 days. The front view SEM image of **Fig. 1.8** illustrates an example of TiO_2 NWs grown by thermal oxidation by Zhang et al. using NaOH aqueous solution at 200°C for 24h [57]. A similar method called solvothermal process, apply a non-aqueous solution to produce the NWs [61-63]. The non-aqueous solvent can enable to control the nanostructure shapes. The TEM image in **Fig. 1.9** reports TiO_2 NWs obtained by solvothermal method [62].
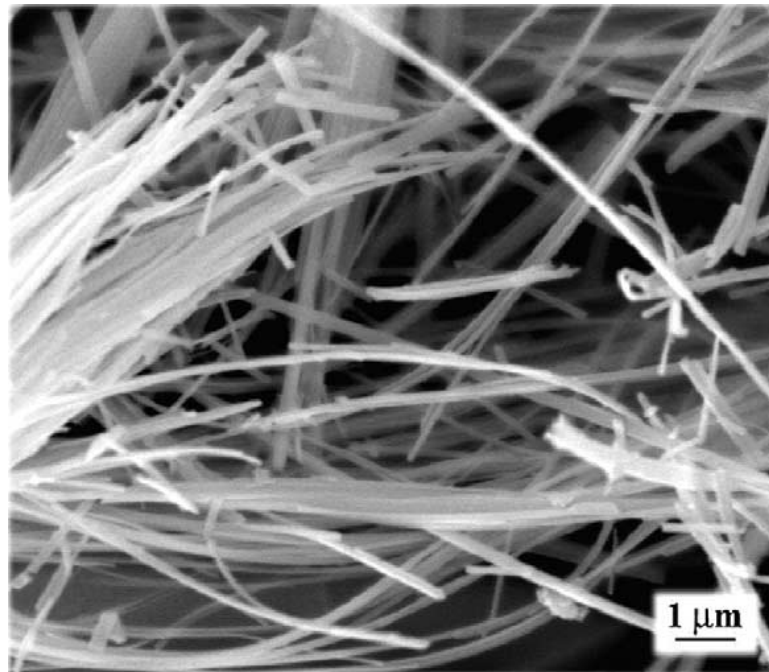
Figure 1.8 - SEM images in front-view of TiO$_2$ anatase nanowires synthetized by hydrothermal process [57].
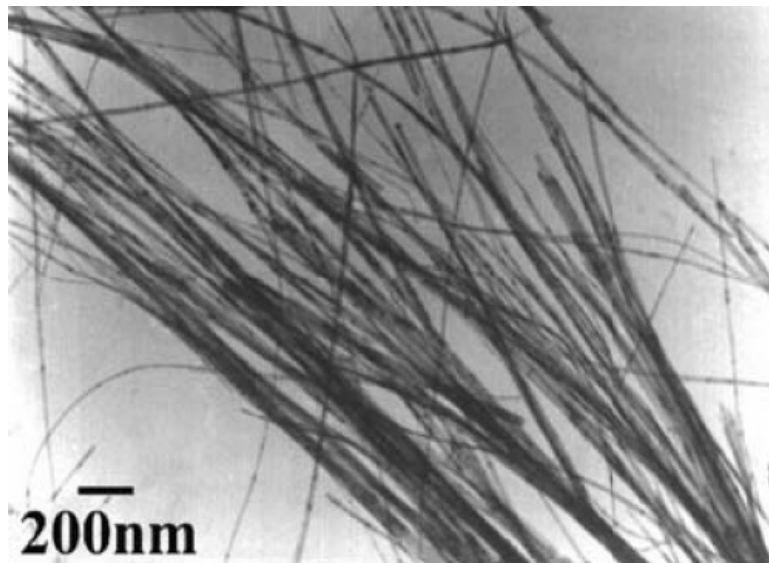

Figure 1.9 - TEM image of TiO$_2$ NWs synthetized by solvothermal method [62].

26

TiO$_2$ nanowires can be also obtained by electrodeposition with the use of the template of an AAM [64, 65]. Commonly this technique is employed to create coating, usually metallic, on a surface by the action of reduction at the cathode. The substrate to be coated is used as cathode and immersed into a solution which contains a salt of the metal to be deposited. The metallic ions are attracted to the cathode and reduced to metallic form. To synthetize TiO$_2$ NWs, the electrodeposition is carried out in 0.2 M TiCl$_3$ solution with pH   = 2 with a pulsed electrodeposition approach, and titanium and/or its compound are deposited into the pores of the AAM. By heating the above deposited template at 500 °C for 4 h and removing the template, pure anatase TiO$_2$ nanowires can be obtained, showed in a representative SEM cross section image of **Fig. 1.10**.
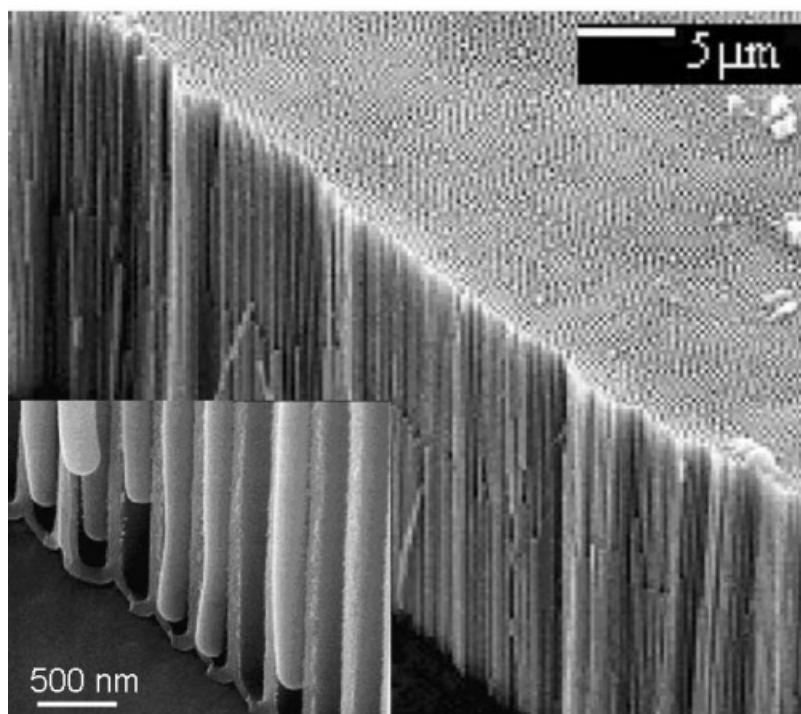

Figure 1.10 - SEM image in cross-section view of TiO2 NWs obtained by electrodeposition using a template of AAM [65].

The above described solution grown methods are capable of yielding highly uniform products however, they often require very precise control of the chemical properties of the solution (e.g. pH, viscosity, etc.) and can generate species in the final product which require removal once the reaction has completed. Indeed, many of these techniques involve the use of chemical additives which could impact device performance. Additionally, post treatments including cleaning, compaction, and sintering are often required for integration or fabrication into a device thus adding both costs (for processing equipment and the required highly trained personnel) and complexity to the processes.

1.4 – TiO$_2$ Nanowires by vapor phase assisted methods

TiO$_2$ NWs can also be obtained by vapor phase assisted growth, which is one of the most common means for producing nanostructures on a desired substrate. In general vapour deposition methods refers to processes in which materials in vapour state are condensed to form a solid-phase material. If there are chemical reactions taking place during the process it is defined as chemical vapour deposition (CVD), otherwise it is a physical vapour deposition (PVD) mechanism. Different works report about the NWs synthetized by CVD [66] and PVD [67-69]. Usually it is used a Ti pure metal powder that is placed on a quartz boat next to the substrate and inserted in a furnace at 850°C with an argon flow for 3h. A typical SEM
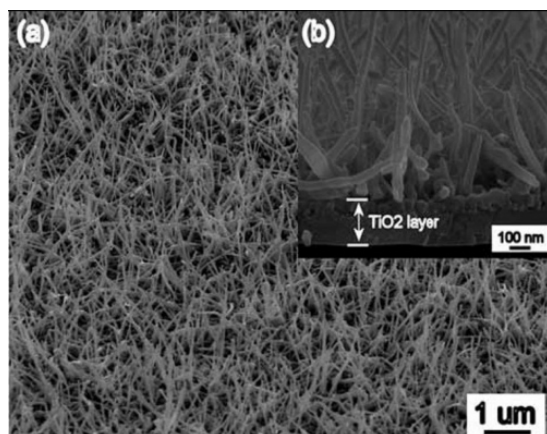

Figure 1.11 - SEM image of TiO$_2$ NWs grown by PVD process process [67].

28

image of TiO$_2$ NWs grown by PVD is illustrated in **Fig. 1.11**.

The vapor phase constituents can be a metal (as in the last example), and in this case we deal with a vapor-solid (VS) and vapor-liquid-solid (VLS) process; or it can be an oxygen-bearing gas and in this case we have a growth by oxidation.

In general, the vapor phase assisted approach has several advantages over the solution methods:

 - first and foremost, the nanostructures can often be grown directly onto a desired substrate, allowing for easy integration into an existing device or product during the fabrication process.

- additionally, a tight control over chemical reactants, compared to those required in solution treatments, is not typically necessary for these processes, thus allowing for both a wider margin of error in processing and a reduction in manufacturing costs.

TiO$_2$ NWs were grown by VLS by using Au as the liquid catalyst [70]. Wu et al. used a Ti thin film was deposited on a substrate by DC magnetron sputtering, a subsequent Au layer was added, and the sample was placed in a horizontal furnace. Ti powder was then placed upstream and heated to 1050°C while the substrate was maintained at 750°C. The Au formed liquid droplets at this temperature providing the catalytic sites necessary for 1-D growth. High purity Ar (99.999%) was flown through the furnace carrying the vaporized Ti downstream for condensation on the substrate. By this process Wu et. al. were able to produce high aspect ratio TiO$_2$ NWs with lengths up to 3 μm and diameters in the range of 60-90 nm [70].

Although Au is the most widely used metal catalyst used in the VLS growth method it is not the only catalyst used. Baik *et. al.* also successfully grew NWs using a catalyst other than Au [66]. Single crystal TiO$_2$ NWs were grown on Ti thin film, deposited via electron beam lithography, by atmospheric pressure chemical vapor deposition (APCVD) using Ni as the catalyst. TiO powder was placed in an alumina boat upstream from the thin film in a horizontal tube furnace which was heated to 950°C and high purity Ar was flown as the carrier gas. This process resulted in NWs with mean diameters of 48 nm and lengths of 10-30 μm for a 2 hour process duration [66]. A small metallic droplet was easily visible at the tip of the NWs as seen in Figure 7 (inset), a sure indicator of the VLS mechanism.
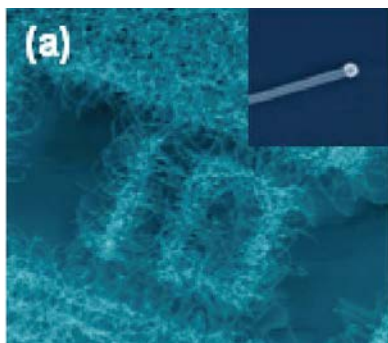
Figure 1.12 – SEM image of TiO$_2$ NWs grown by APCVD; inset: high magnification of a NWs with the metal cap on its tip [66].

VLS method presents the important advantage of being highly versatile and useful in its ability to be scaled up for mass production. Anyway, this mechanism is not without its shortcomings, the most notable of these being the residual metal alloy cap left on the NWs post growth treatment. Depending on the desired application, this may cause an added step of complexity if the application requires a cap/impurity free nanostructure. One may be able to employ chemical methods to remove the metal cap but care must be taken to ensure that neither the nanostructure morphology nor the device itself is destroyed. We define "thermal oxidation growth" when the only vaporized source material for the formation of the 1-D structures is oxygen, which reacts with the substrate during a thermal treatment.

The oxygen can be introduced from different sources which can influence the morphology of the synthetized structure. In this respect, Peng *et. al.* [71] thermally oxidized Ti metal substrates at 850 °C in three different oxygen environments: high purity oxygen, a low oxygen concentration Ar mixture, and in acetone. Both the low oxygen concentration mixture and the acetone heat treatments produced nanostructures but the high purity oxygen produced only a planar film, as reported in **Fig.1.13.**
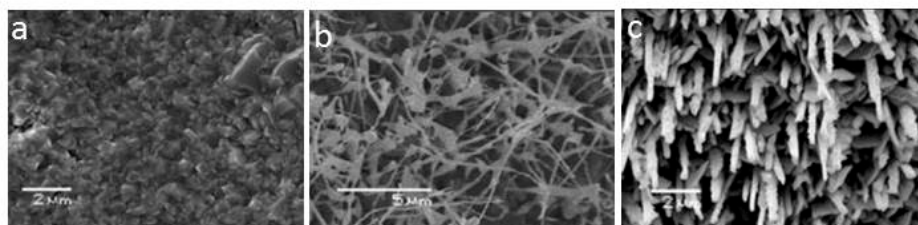

Figure 1.13 – SEM images of Ti metal substrates thermally oxidized in different atmospheres: (a) high purity oxygen, (b) low oxygen concentration Ar mixture and, (c) acetone [71].

The samples oxidized in acetone produced well-aligned nanorod arrays while the low oxygen concentration treated samples produced nanofibers several microns in length growing epitaxially from the surface of large TiO_2 grains. The difference in morphology between these three samples was attributed to the different growth rates of TiO_2 and to the difference in the dominating diffusion species, titanium and oxygen. The growth of the planar film in the high purity oxygen was explained by oxygen diffusion being predominant because of the high concentration of oxygen. It is theorized that TiO_2 is grown between the TiO_2 grains and the Ti metal surface resulting in the growth of very large TiO_2 grains. The growth of the nanofibers from the low oxygen concentration mixture was attributed to the surface diffusion of Ti cations. All nanofibers formed by this process were seen growing from ledges of TiO_2 grains instead of from grain boundaries or smooth surfaces. This was explained by Ti cations diffusing to the grain ledges and reacting with the gaseous oxygen to grow the nanostructures.

Although this explains why the growth occurs preferentially at the ledges, it does not explain how or why growth is confined to 1-D. The third process, growth in acetone, produced well aligned arrays of nanorods. Here, the difference between nanofibers (grown in low oxygen environment) and nanorods is simply the difference in average diameter: nanorods ~500 nm and nanofibers ~200 nm. The availability of oxygen for the oxidation of Ti is much less in the acetone environment compared to either of the other two environments used. Due to this, it was suggested that Ti diffusion was the predominant process in the growth of the oxide. A two-step process was presented as the means of producing the nanorods (see **Fig. 1.14**). First, a very thin layer of TiO_2 formed through which Ti diffused by a network of grain boundaries in the oxide to react with the acetone on the surface of the oxide. The confinement to 1-D is attributed to the preferential adsorption of acetone on specific TiO_2 faces resulting in preferential oxide growth on these faces. A more recent paper by the authors [6] lists <001> as the preferred growth direction for the nanorods. This paper also investigated the impact of temperature on the resulting nanostructures but added no further insight into the mechanisms involved.

Thermal methods allow producing TiO_2 NWs with low chemical contaminations in the stable phase of rutile. Additionally, the presented oxidation processes is relatively low cost and easily scalable for mass production of TiO_2 nanowires giving it a distinct advantage over other nanowire production methods.

Synthesis mechanism is still controversial and a systematic study as a function of annealing parameters is still lacking. Moreover, NWs can be grown on a solid substrate offering the possibility to perform an experimental investigation of their electrical properties with conventional and well-established spectroscopic characterizations.
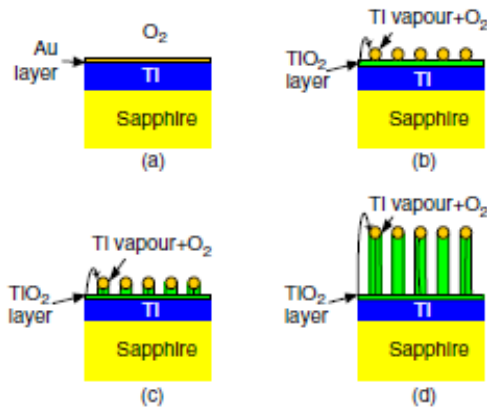
Figure 1.14 – Schematic illustration of the growth procedure of TiO2 NWs proposed by Lee *et. al.* [TiOx3]

1.5 – Au-Ti alloy phase diagram

The Au-Ti binary alloy phase diagram is reported in **Fig. 1.15**. A thorough review of the literature on the thermodynamics of the Au-Ti system has been given in [72] and a thermodynamic optimised dataset has been reported by [73]. The optimisation takes into account 5 experimental datasets for the phase diagram from the literature, a calorimetric investigation of the mixing enthalpy in Au-rich melts and reported standard enthalpies of formation for three of the intermetallic compounds, $AuTi_3$, $AuTi$, and Au_2Ti which have been obtained from direct synthesis calorimetry.

Figure 1.15 – Calculated phase diagram for the system Au-Ti [72, 73].

The low-temperature modifications of the AuTi compound have not been included in the optimisation due to a lack of data. Invariant reaction are reported in the following table.

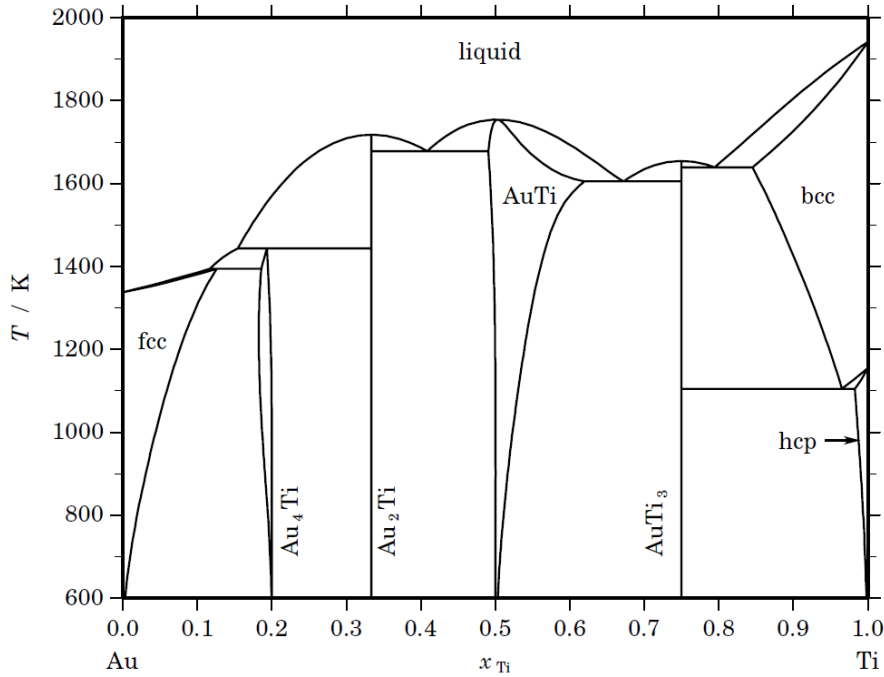**Table 1.1** – Invariant reactions of the system Au-Ti [72, 73].

Reaction	Type	T / K	Compositions / x_{Ti}			$\Delta_r H$ / (J/mol)
liquid $\rightleftharpoons$ AuTi	congruent	1754.6	0.503	0.503		−28799
liquid $\rightleftharpoons$ Au$_2$Ti	congruent	1717.9	0.333	0.333		−43289
liquid $\rightleftharpoons$ Au$_2$Ti + AuTi	eutectic	1678.0	0.409	0.333	0.490	−35388
liquid $\rightleftharpoons$ AuTi$_3$	congruent	1654.4	0.750	0.750		−23842
liquid $\rightleftharpoons$ AuTi$_3$ + bcc	eutectic	1639.3	0.794	0.750	0.845	−18241
liquid $\rightleftharpoons$ AuTi + AuTi$_3$	eutectic	1604.9	0.672	0.619	0.750	−21471
liquid + Au$_2$Ti $\rightleftharpoons$ Au$_4$Ti	peritectic	1443.7	0.154	0.333	0.193	−21679
liquid + Au$_4$Ti $\rightleftharpoons$ fcc	peritectic	1394.1	0.116	0.186	0.126	−8854
bcc $\rightleftharpoons$ AuTi$_3$ + hcp	eutectoid	1104.9	0.965	0.750	0.982	−5129

The Au-Ti phase diagram is not a simple diagram like the Au-Si one, so it is more difficult to identify the reactions occurring during the seed assisted growth of Ti nanowires. Some eutectic points are reported at very hight temperature with respect to the experimental conditions of nanowires growth with Au-Ti systems. Moreover, Ti reacts quickly with the O present in the environment leading the formation of titania nanowires instead of pure Ti nanowires with a shell of oxide such as the case of Si and Ge nanowires [74]. According to the previous general obeservations, a ternary phase diagram should be considered in order to correctly take into account the effect of Oxygen. On one side the complex thermodynamics does not help to clarify what happens during the titania nanowires growth, on the other side we should take into accounts the diffusion phenomena that can occur during the annealing of the Au-Ti systems. Transmission electron microscopy analyses [75] showed that Au/Ti thin films annealed in vacuum above 400 °C undergo diffusion of Ti atoms into Au grain boundaries and form the intermetallic phases $TiAu_4$, $TiAu_2$, TiAu, and Ti_3Au [76, 73]. A schematic representation of the phenomenology is showed in **Fig.1.16**. The authors
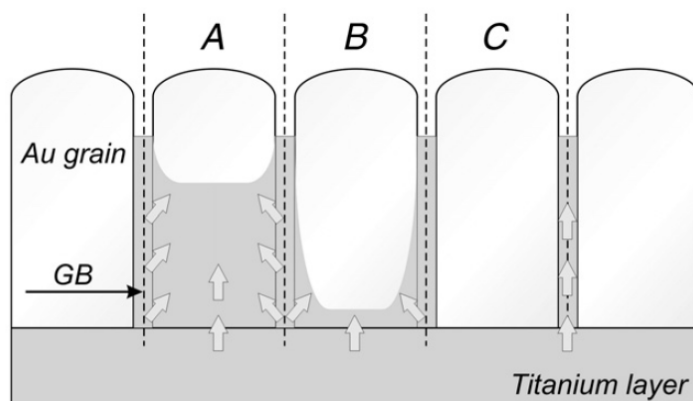
Figure 1.16 - Schematic representation of the three kinetic regimes (A, B, and C) of diffusion in polycrystalline systems for the case of Ti diffusing into Au thin films (GB=grain boundaries). The A regime refers to abundant atomic migration from the boundaries into the grains. B-kinetics describes a limited diffusion from the grain boundaries into the grains; in this case a combination of bulk and grain boundary diffusion occurs. Finally, C-kinetics refers to purely grain boundaries diffusion — the bulk contribution is negligible [81]

showed also that very small quantities of these intermetallics can precipitate at low processing temperatures (100–150 °C). Further contributions [77] confirm that co-evaporated Au–Ti thin films can react and form intermetallics when annealed in vacuum at temperatures ranging between 300 and 900 °C. However, as shown in Refs. [78.] and [79], when the heat-treatment is performed in air, titanium diffuses up to the gold free surface and form both anatase and rutile by reacting with oxygen. It was shown that, at temperatures ranging between 630 and 1030 °C, Ti diffusion in bulk Au is on the order of 10^{-13} and 10^{-9} cm^2/s, thus indicating that Ti diffusion in Au is about one order of magnitude smaller than Au self-diffusion [80].

Martinez et al. [81] reported an experimental investigation to determine the Ti diffusion in Au. The 200 nm Ti on 260 nm Au samples were annealed in air in the temperature range 200-500 °C and characterized using a secondary ion mass spectrometry (SIMS). No Ti–Au intermetallic phase could be detected by XRD at any temperature. These observations with the SIMS results prove that Ti can diffuse through the Au layer and form a rutile phase on the free surface of the samples. These observations will be useful to characterize the growth mechanism of titania nanowires of our experimental work in the next chapter.

References

[1] Martinez J., Martinez R. V. and Garcia R., Nano Letters 2008, 8, 3636.

[2] Francioso L. and Siciliano P., Nanotechnology 2006, 17, 3761.

[3] Dick K.A., Progress in Crystal Growth and Characterization of Materials, 54 (2008) 138-173

[4] Wagner R. S., Ellis W. C., Appl. Phys. Lett. 4 (1964) 89.

[5] Lee J.-C., Park K.-S., Kim T.-G.,. Choi H.-J and. Sung Y.-M, Nanotechnology 17 (2006) 4317.

[6] Peng X. S., Wang J. P., Thomas D. F. and Chen A. C., Nanotechnology 16 (2005) 2389.

[7] Wagner R.S., in: A.P. Levitt (Ed.), Whisker Technology, Wiley-Interscience, New York, 1970, p. 47.

[8] Kolasinski K.W., Curr. Opin. Solid State Mater. Sci. 10 (2006) 182–191.

[9] Tu K.-N., Mayer J. W., Feldman L.C., Electronic Thin Filmm Science - for electrical engeineers and materials scientists, Macmillan Publishing Company, New York, 1992

[10] Buffat P., Borel J.-P., Phys. Rev. A 13 (1976) 2287.

[11] Dick K., Dhanasekaran T., Zhang Z., Meisel D., J. Am. Chem. Soc. 124 (2002) 2312.

[12] Magnusson M.H., Deppert K., Malm J.-O., Bovin J.-O., Samuelson L., J. Nanoparticle Res. 1 (1999) 243.

[13] Kamins T.I., Williams R.S., Basile D.P., Hesjedal T., Harris J.S., J. Appl. Phys. 89 (2001) 1008.

[14] Bootsma G.A., Gassen H.J., J. Cryst. Growth 10 (1971) 223.

[15] Kodambaka S., Tersoff J., Reuter M. C., Ross. F. M., Science 316 (2007) 729.

[16] Adhikari H., Marshall A. F., Chidsey C. E. D. and McIntyre P. C., Nano Lett. 6 (2006) 318.

[17] Schmidt V. and Gösele U., Science 316 (2007) 698.

[18] Arbiol J., Kalache B., P. Roca i Cabarrocas, J.R. Morante, Foncuberta A. F.I. Morral, Nanotechnology 18 (2007) 305606.

[19] Yao Y., Fan S., Mater. Lett. 61 (2007) 177.

[20] Wang Y., Schmidt V., Senz S., Gosele U., Nat. Nanotech 1 (2006) 186.

[21] Baron T., Gordon M., Dhalluin F., Ternon C., Ferret P., Gentile P., Appl. Phys. Lett. 89 (2006) 233111.

[22] Kamins T.I., Li X., Williams R.S., Liu X., Nano Lett. 4 (2004) 503.

36

[23] Tuan H.Y., Lee D.C., Hanrath T., Korgel B.A., Nano Lett. 5 (2005) 681.

[24] Tuan H.Y., Lee D.C., Hanrath T., Korgel B.A., Chem. Mater 17 (2005) 2705.

[25] Wang G.T., Talin A.A., Werder D.J., Creighton J.R., Lai E., Anderson R.J., Arslan I., Nanotechnology 17 (2006) 5773.

[26] Ohno Y., Shirahama T., Takeda S., Ishizumi A., Kanemitsu Y., Solid State Commun. 14 (2007) 228.

[27] Colli A., Hofmann S., Ferrari A.C., Ducati C., Martelli F., Rubini S., Cabrini S., Franciosi A., Robertson J., Appl. Phys. Lett. 86 (2005) 153103.

[28] Kirkham M., Wang X., Wang Z.L., Snyder R.L., Nanotechnology 18 (2007) 365304.

[29] Regolin I., Khorenko V., Prost W., Tegude F.J., Sudfeld D., Kastner J., Dumpich G., Hitzbleck K., Wiggers H., J. Appl. Phys. 101 (2007) 054318.

[30] Yan H.F., Xing Y.J., Hang Q.L., Yu D.P., Wang Y.P., Xu J., Xi Z. H. and Feng S. Q., Chemical Physics Letters 323 (2000) 224–228.

[31] X. Chen, Xing Y., Xu J., Xiang J., Yu D., Chemical Physics Letters 374 (2003) 626–630.

[32] Wang H., Fischman G.S., J. Appl. Phys. 76 (1994) 1557.

[33] Trentler T.J., Hickman K.M., Goel S.C., Viano A.M., Gibbons P.C., Buhro W.E., Science 270 (1995) 1791.

[34] Yu D.P., Xing Y.J., Hang Q.L., Yan H.F., Xu J., Xi Z.H., Feng S.Q., Physica E 9 (2001) 305.

[35] T. Hanrath, Korgel B.A., Adv. Mater 15 (2003) 437.

[36] Bahloul-Hourlier D. and Perrot P., Journal of Phase Equilibria and Diffusion vol. 28 (2007) 150.

[37] Sear R.P., J. Phys: Condens. Matter 19 (2007) 466106.

[38] P. Cheyssac, M. Sacilotti, G. Patriarche, J. Appl. Phys. 100 (2006) 044315.

[39] Nebol'sin V.A., Shchetinin A.A., Inorg. Mater 39 (2003) 899.

[40] Glas F., Harmand J.-C., Patriarche G., Phys. Rev. Lett. 99 (2007) 146101.

[41] B.A. Wacaser, Doctoral Thesis, Lund University, 2007.

[42] Lau Y. K. A., Chernak D. J., Bierman M. J. and Jin S., J. Mater. Chem. 19 (2009) 934.

[43] Bierman M. J., Y. K. A. Lau, Kvit A. V., Schmitt A. L. and Jin S., Science 320 (2008) 1060.

[44] Eshelby J. D., J. Appl. Phys. 24 (1953) 3.

[45] Zhu J., PengH. L., Marshall A. F., Barnett D. M., Nix W. D. and Cui Y., Nat. Nanotechnol. 3 (2008) 477.

[46] Brenner S.S, Sears G.W, Acta Metallurgica 4 (1956) 268.

[47] Nikoobakht B., Eustis S. and Herzing A., J. Phys. Chem. C 113 (2009) 7031.

[48] Prokes S. M. and Arnold S., Appl. Phys. Lett. 86 (2005).

[49] Omi H. and Ogino T., Appl. Phys. Lett. 71 (1997) 2163.

[50] Kim B. S., Koo T. W., Lee J. H., Kim D. S., Jung Y. C., Hwang S. W., Choi B. L., Lee E. K., Kim J. M. and Whang D., Nano Letters 9 (2009) 864.

[51] Yang G. Z., Cui H., Sun Y., Gong L., Chen J., Jiang D. and Wang C. X., J. Phys. Chem. C 113 (2009) 15969.

[52] Ho S. T., Wang C. Y., Liu H. L. and Lin H. N., Chem. Phys. Lett. 463 (2008) 141.

[53] Lin, Y., Wu, G. S., Yuan, X. Y., Xie, T., Zhang, L. D., J. Phys.: Condens. Matter 15 (2003) 2917.

[54] Armstrong A. R., Armstrong G., Canales J., Garcia R., Bruce P. G., AdV. Mater. 7 (2005) 862.

[55] Armstrong A. R., Armstrong G., Canales J., Garcia R., Bruce P. G., Angew. Chem., Int. Ed. 43 (2004) 2286.

[56] Yoshida R., Suzuki Y., Yoshikawa S. J., Solid State Chem. 178 (2005) 2179.

[57] Zhang, Y. X. Li, G. H. Jin, Y. X. Zhang, Y. Zhang, J. Zhang, L.D. Chem. Phys. Lett. 365 (2002) 300.

[58] Nian J. N., Teng H. S., J. Phys. Chem. B 110 (2006) 4193.

[59] H. Yin, G. Ding, B. Gao, F. Huang, X. Xie, M. Jiang, Mater. Res. Bull. 47 (2012) 3124.

[60] A. Hu, X. Zhang, K.D. Oakes, P. Peng, Y. N. Zhou, M. R. Servos, J. Hazard. Mat. 189 (2011) 278-285.

[61] Wen, B.; Liu, C.; Liu, Y. Inorg. Chem. 44 (2005) 6503.

[62] Wen, B.; Liu, C.; Liu, Y. New J. Chem. 29 (2005) 969.

[63] Wen, B.; Liu, C.; Liu, Y. J. Phys. Chem. B, 109 (2005) 12372.

[64] Lei Y., Zhang L. D., Fan J. C., Chem. Phys. Lett. 338 (2001) 231.

[65] Liu S., Huang K., Sol. Energy Mater. Sol. Cells 85 (2004) 125.

[66] J. M. Baik, M. H. Kim, C. Larson, X. Chen, S. Guo, A. M. Wodtke and M. Moskovits, Appl. Phys. Lett. 92 (2008) 242111.

[67] Wu, J. M.; Shih, H. C.; Wu, W. T. Chem. Phys. Lett. 413 (2005) 490.

[68] Wu, J. M.; Shih, H. C.; Wu, W. T.; Tseng, Y. K.; Chen, I. C. J. Cryst. Growth 281 (2005) 384.

[69] Xiang, B.; Zhang, Y.; Wang, Z.; Luo, X. H.; Zhu, Y. W.; Zhang, H. Z.; Yu, D. P. J. Phys. D, 38 (2005) 1152.

[70] J. M. Wu, W.-T. Wu and H.C. Shih, J. Electrochem. Soc. 152 (2005) G613.

[71] X. S. Peng and A. C. Chen, J. Mater. Chem. 14 (2004) 2542.

[72] Murray J.L. in: Phase Diagrams of Binary Titanium Alloys, Murray J.L., Ed., ASM Intl., Metals Park, OH, 1987, pp. 27–32.

[73] Luo W., Jin Z., Liu H., Wang T.: Calphad 25 (2001) 19–26.

[74] Romano L., Rudawski N. G., Holzworth M. R., Jones K. S., Choi S. G. and Picraux S. T., J. Appl. Phys., Vol. 106 (2009) 114316.

[75] Tisone T.C., Drobek J., J. Vac. Sci. Technol. 9 (1971) 271.

[76] Murray J.L., Bull. Alloy Phase Diag. 4 (1983) 278.

[77] Katz A., Murarka S.P., Nissim Y.I., Harper J.M.E., Adva. Meta. and Proc. for Semi. Devi. and Circ. — II, Sumposium, 1992 Pittsburgh, U.S.A.

[78] Poate M., Turner P.A., Debonte W.J., Yahalom J., J. Appl. Phys. 46 (1975) 4275.

[79] Sylwestrowicz W.D., Elkholy H.A., Kammlott G.W., J. Mater. Sci. 14 (1979) 873.

[80] Henry B.M., StatonBevan A.E., Sharma V.K.M., Crouch M.A., Appl. Surf. Sci. 108 (1997) 485.

[81] Martinez W.E., Gregori G., Mates T., Thin Solid Films 518 (2010) 2585–2591.

Chapter 2

TiO$_2$ Nanowires synthesis

This chapter is dedicated to the main topic of this dissertation: the study of the thermal synthesis of titania nanowires on Ti substrates, through a seed assisted growth mechanism. We will analyze and discuss the experimental procedure, the morphological and structural characterizations, and the dynamic of the growth mechanism on Ti foil. The second section shows some experiments of NWs growth on non-flat Ti substrates.

2.1 - Synthesis on Ti foil

In this section we will go in depth on the synthesis of TiO$_2$ NWs on Ti foil performed by means of a thermal seed assisted process. We will illustrate the technical details related to the material preparation and the instruments used for the samples characterization. Next, we will treat in details the growth process varying different parameters such as temperature, annealing time and gas flow; we will discuss the related results together with the morphological and structural characterization data. Finally, the growth dynamic of the TiO$_2$ NWs will be studied by means of an *in-situ* annealing process.

2.1.1 – Experimental

The samples used as substrate for the growth of TiO$_2$ NWs were Ti foils, with thickness 0.13 mm and 0.25 mm and purity ≥99.99% (Sigma Aldrich). Each sample was cut by diamond saw in pieces of about 1x1 cm^2 and cleaned via ultra-sonication in acetone for 30 min and successively in isopropyl alcohol for 15 min. Afterwards, a thin layer of gold with thickness in the range 3-5 nm, was deposited on the sample surface by means of an RF

(60 Hz) Emitech K550X sputter. The deposition occurred in Ar flow at a plasma current of 10 mA for 1 to 3 min, with a chamber pressure of 0.02 mbar and using an Au target of 99.999% purity. Rutherford Backscattering Spectrometry (RBS) by HVEE Singletron was used to measure the Au film thickness, with standard configuration of 2 MeV $^4He^+$ beam and 165° scattering angle.

The thermal oxidation process of TiO₂ NWs synthesis was carried out by annealing the as deposited Au/Ti sample in a carbolite horizontal furnace at temperatures between 700°C and 1000°C, for 1 to 4 hours in a mixed gas flow of argon (1.5 – 10 lpm) and oxygen (5 – 1 lpm).

In situ SEM annealing has been performed by means of the equipment FEI Quanta 200 FEG Environmental-SEM. For this purpose, an Au film was deposited on the Ti foil surface, following the same procedure already reported for the other samples. Then, the sample was inserted in the SEM furnace placed inside the SEM chamber and annealed at 800°C and 1000°C for annealing time ranging from few minutes up to 2 hours and half, in water vapour atmosphere at 500 Pa

The morphology of the grown NWs was analysed by Scanning Electron Microscopy (SEM) using a Gemini field emission SUPRA 25 of Carl Zeiss, in plan-view and cross-section. The structure was investigated with X-Ray Diffraction (XRD) by means of a Bruker D-9000 diffractometer with Cu Kα. The Au thickness was determined by Rutherford Backscattering Spectrometry (RBS) with 2 MeV $^4He^+$ beam and 165° scattering angle. Transmission Electron Microscopy (TEM) was performed by using a microscope Jeol 2010F with a camera Gatan Orius 2k/2k at an acceleration voltage of 200 keV.

2.1.2 - Morphological and structural characterization

TiO₂ NWs on Ti foil were synthetized using different annealing times (1 to 4 hours), temperatures (700°C to 1000°C) and flow rates (various O₂/Ar mix). The effect of the annealing temperature was investigated by thermally processing Ti foils samples at different temperatures, namely 700°C, 800°C, 900°C and 1000°C. The minimum studied temperature was set to 700°C since lower annealing temperature had showed experimentally

rare and short NWs. **Fig. 2.1** reports the SEM plan-view images of samples annealed at 700°C (**Fig.2.1.**a and e), at 800°C (**Fig.2.1**.b and f), at 900°C (**Fig.2.1**c and g) and at 1000°C (**Fig.2.1**d and h). The images of **Fig.2.1**a) to d) refer to samples annealed for 1 hour, while annealing time of 4 hours was applied to the foils reported in **Fig.2.1**e) to h).

The results indicate that increasing the temperature above 700°C, the growth kinetics is strongly improved. Indeed, at 700°C very few NWs were grown, and they are characterised by a maximum length of 200- 300 nm (**Fig.2.1**a). Already at 800°C (**Fig.2.1**b) the NWs density increased and the maximum length went up to 2-3µm. Au nanoparticles are present on top of the nanowires, and they typically refer to the vapour-liquid-solid process, widely treated in literature in particularly for the synthesis of silicon nanowires [1] as we already discussed in Chapter 1. Gold caps suggest that the nanowires formed because of the unidimensional growth catalysed by the Au nanoparticles laying on the surface. First, Au nanoparticles are formed during annealing on the substrate surface because of de-wetting [2]. Second, we suppose that Ti atoms diffused from the substrate in the Au drops or through the Au film and precipitated forming nanowires, as reported in section 1.5. Since several NWs show a larger bottom section with respect to the top, the mechanism could be ascribed to a surface diffusion mediated growth, already discussed in Paragraph 1.2.2. Being oxygen, TiO$_2$ formed and the TiO$_2$ nanowire elongated along a main growth direction. Furthermore, several nanowires present a change of direction within their structures, even with very sharp edges. This effect is probably due to the presence of an extended defect in the crystallographic structure of the nanowire. Indeed, as for a polycrystalline growth [3], the nucleation of a crystallographic defect can act as an instability and lead to an abrupt change of crystal structure that – in the nanowire – is observed like a sharp change of the main growth direction.

Increasing the annealing temperature to 900°C (**Fig.2.1**c), the synthetized structures resulted very similar to the ones processed at 800°C. Indeed, an increase of the average length of the NWs up to 4-5µm is obtained.
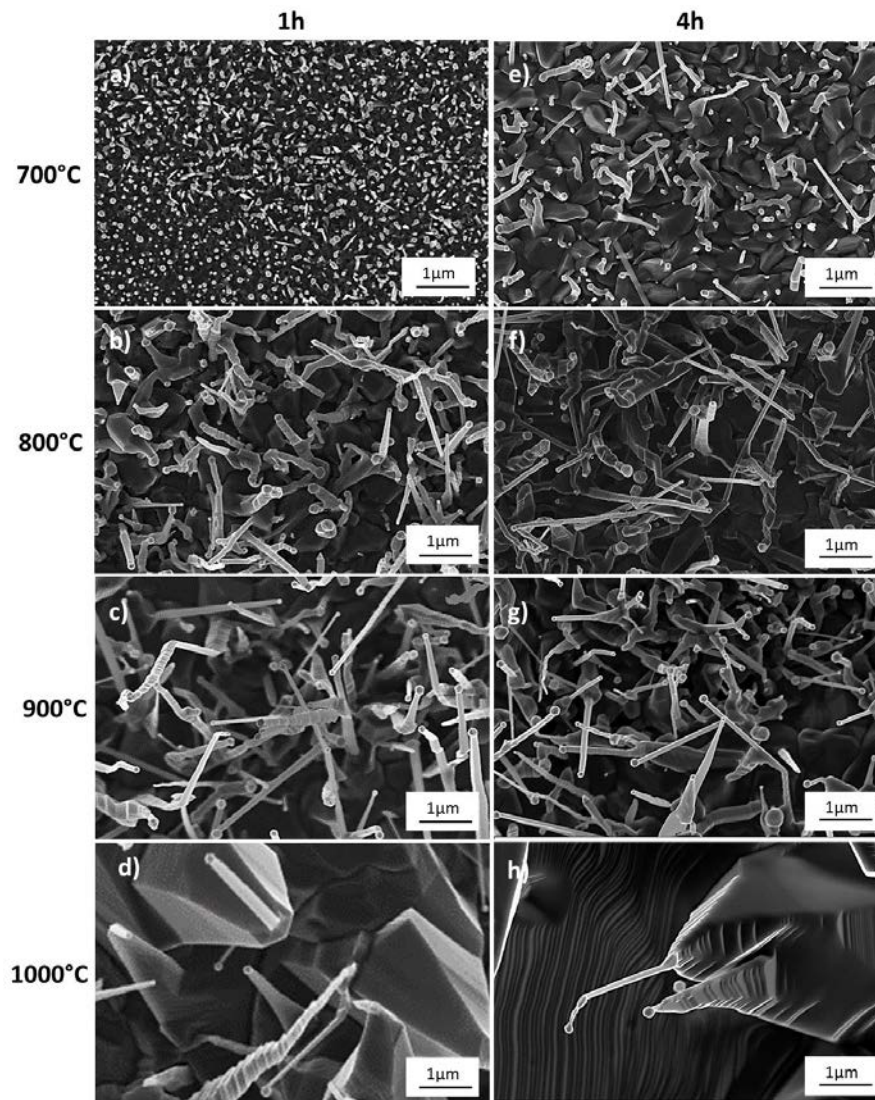
Figure 2.1 - SEM plan view of TiO2 NWs growth at different temperatures: a) and e) at 700°C, b) and f) at 800°C, c) and g) at 900°C, d) and h) at 1000°C.

A different effect was obtained by annealing at 1000°C, where the NWs growth mechanism occurred in competition with microcrystal grain formation, as showed in the SEM image of **Fig.2.1**d.

It is important to mention that the samples processed at annealing temperatures higher than 800°C, resulted to be fragile and friable at the macroscopic level, hence not optimal for future applications. **Fig.2.1**e) to h) show the samples obtained with increasing the annealing time to 4 hours. In particular, a comparison of **Fig.2.1**a) and e) show that at 700°C the nucleation is improved (higher density of NWs) together with the length and the diameter of the nanostructures. At 800° and 900°C we observe an increase in the average NWs length. This is due to the fact that the nucleation is fully activated at temperature higher than 700°C, therefore longer annealing time only favour the growth of NWs in length.

Fig.2.1h (sample processed at 1000°C, 4h) shows that the competitive mechanism of micrograins nucleation prevails over the NWs growth, since the grains increased in size while the NWs are shorter and set on the top of the grains. Considering the results reported so far, the annealing conditions of 800°C for 4 hours offered the optimal performances of NWs density and length.

The growth direction of nanowires has no specific orientation with respect to the substrate. Epitaxial growth was observed for Si VLS nanowires on a single crystal substrate [1]. This is not the case for oxides, moreover the substrate foil has a polycrystalline structure.

Several nanostructures are formed during the annealing process. The SEM plan view images of **Fig.2.2** show that it is possible to find structures such as ribbons, facet nanowires, spikes, rods, either with or without the Au cap on the top. However, the predominant structure is the facet nanowire with gold on its tip, as it was also illustrated by the images of **Fig.2.1**. In **Fig.2.2c** it is also possible to better appreciate the morphology of the NWs Au caps, which do not show a spherical shape, but a more facet one. The facet shapes on the Au nanoparticle is usually associated with a solid phase particle. However, according with observations about the growth mecanisms of Chapter 1, we cannot definitely determine the phase status of the Au caps without an in situ structural analysis (section 1.2.2).

Once again, the growing mechanism could be referred to a seed assisted growth where the source of Ti is the substrate itself, Ti diffuses through the thin Au layer or along the Au particles that are formed during the annealing, then the Au particles catalyze the preferential 1D growth. Furthermore, a pure VLS mechanism with Au as catalyzer is difficult to predict for TiO$_2$ NWs since the Au-Ti phase diagram doesn't show up a single eutectic point (see paragraph 1.5) such as the Au-Si one [1].

In order to investigate the nucleation mechanism as a function of the synthesis parameters, such as gas carrier flow and oxygen content, we prepared a set of samples processed with different gas flow in the furnace
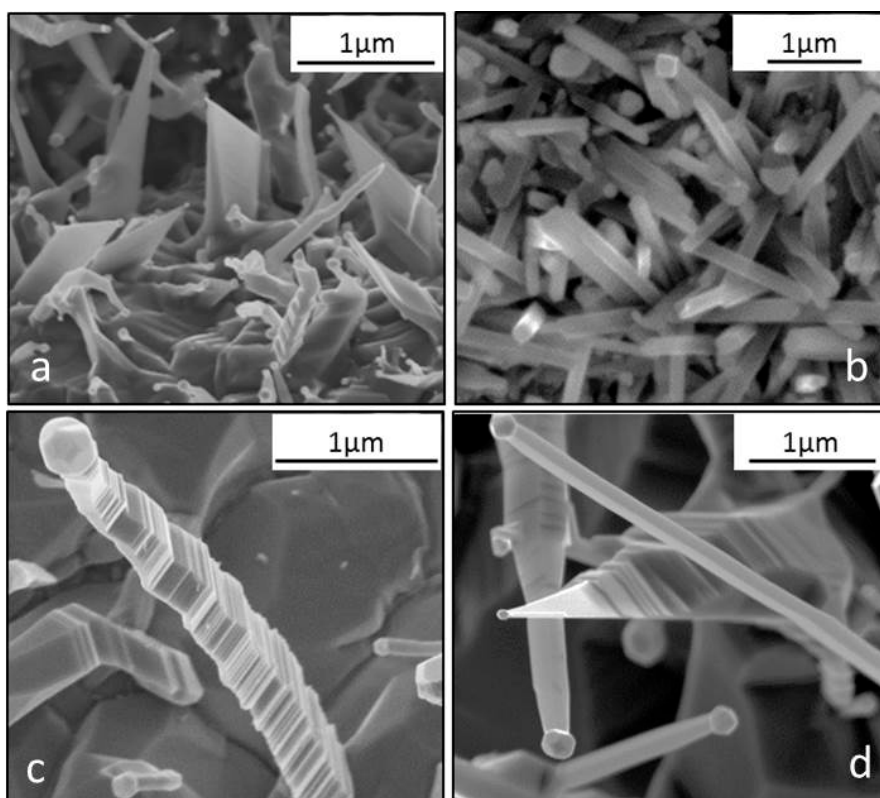

Figure 2.2 – SEM plan view of different TiO$_2$ nanostructures grown during the thermal oxidation process of a Ti foil. Synthesis conditions: 700°C 4h a) and b); 800°C 4h c); 900 °C 4h d).

chamber at annealing temperature of 700°C, which is the threshold temperature for the nucleation process. **Fig.2.3**.**a** shows the high resolution SEM plan-view images of the annealed sample for 4 h at low Ar flow (1 lpm). The Ar gas used for this experiment was pure at 99.999%, so the oxygen contamination is negligible within the range of the experimental set up. TiO$_2$ grains are well distinguished on the sample surface and some of them have an elongated shape on their top that indicates the formation of a NW with a large base (inset of **Fig.2.3**.**a**). Au nanoparticles are well separated from each other, indicating the de-wetting process occurred. Some Au nanoparticles appear to evolve in a dendritic shape as shown in the SEM image of the inset of **Fig.2.3**.a. This effect was reported for Au de-wetting on oxide substrate and it is related to the fast temperature quenching of the annealing process [4]. NWs appear only in few spots with very small area ($\sim\mu m^2$). In particular, these few NWs nucleated in rod-shape and Au nanoparticles are not visible on the top. This kind of growth mechanism was reported in literature for other metal oxides NWs, and it is promoted by the presence of surface roughness or defects in the substrate [5]. Since the substrate is a Ti foil, this growth mechanism is randomly induced on the surface. The uniformity of NWs over the full sample area was indeed very poor in this condition, since NWs can only be detected in small bunches as the one reported in **Fig.2.3**a. In **Fig.2.3**b, it can be observed that the increase of Ar flow (to 15 lpm) favours the NWs growth in some larger spots of the sample with respect to the low gas flow condition (**Fig.2.3**.a).

However, the distribution over the full area of sample is still poor, as it can be observed in the insert of **Fig. 2.3.b**, where the bright zones contain NWs. Therefore, we investigated how to improve the uniformity of NWs distribution. We observed that an increase of oxygen content was effective to promote a uniform growth. **Figures 1.4** a), b) and c) report the SEM of samples annealed at 700°C for 1 h with different mix of argon and oxygen flow.

The NWs distribution is uniform over the full size of the sample, however, the effect of Ar/O$_2$ ratio in this range of flow does not provide a remarkable effect in terms of increase of NWs density. The optimal gas condition was set to 7.5 lpm of oxygen and 10 lpm of argon, based on the

best experimental results of NWs growth as reported in the low and high magnification SEM images of **Fig.2.5**.
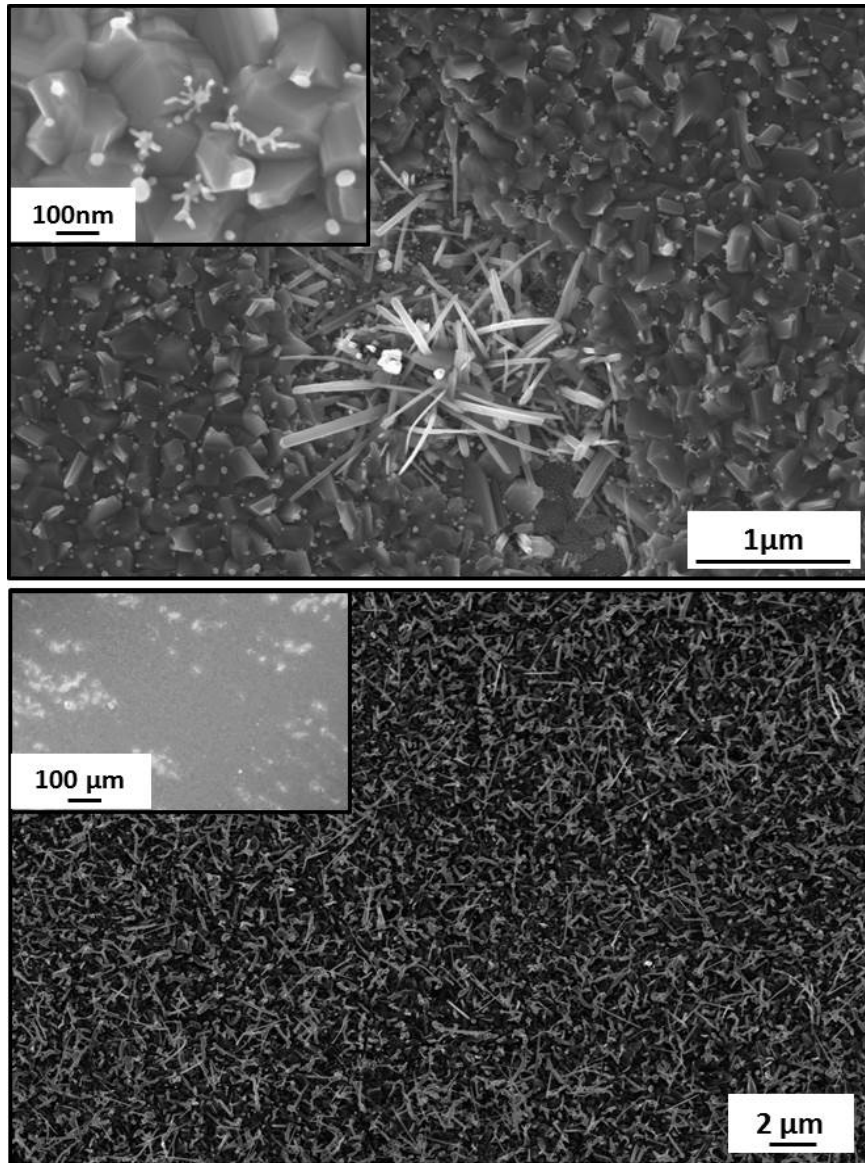

Figure 2.3 – SEM plan view of TiO$_2$ foil with a 3nm of gold layer deposited on the surface, annealed at 700°C for 4h with a) a low Ar flow of 1 lpm and b) an high Ar flow of 15 lpm. Bright zones in the insert of b) contain NWs.

48

Temperature and annealing time were set at the optimal condition of 800°C for 4h as founded earlier.
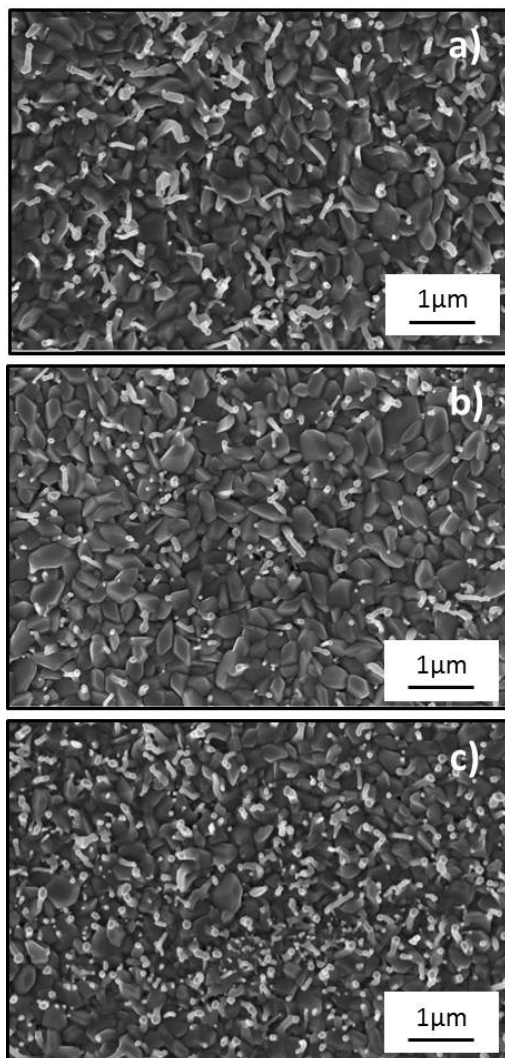

Figure 2.4 - SEM plan views of TiO$_2$ samples annealed at 700°C for 1 h with different argon and oxygen flows: a) O$_2$ 1.5 lpm, Ar 10 lpm; b) O$_2$ 5 lpm, Ar 10 lpm; c) O$_2$ 10 lpm, Ar 5 lpm; d) O$_2$ 7.5 lpm, Ar 10 lpm (optimal flow).
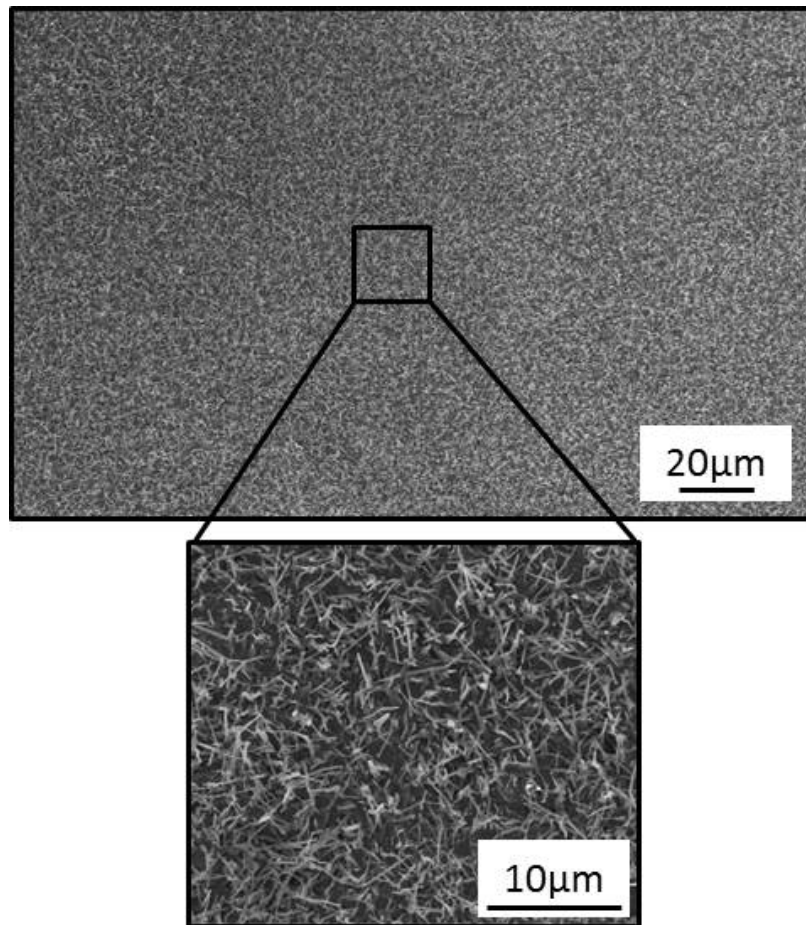
Figure 2. 5 - SEM plan views of TiO$_2$ samples annealed at 700°C for 1 h with flows of O$_2$ 7.5 lpm and Ar 10 lpm (optimal flow) view at low magnification.

The structure of the TiO$_2$ NWs has been analysed by XRD as showed in **Fig. 2.6.**. The TiO$_2$ signals resulted always to be rutile phase which is reported to be the most stable structure upon annealing at temperatures higher than 600°C [6]. The most intense peak is represented by the (110) orientation that is reported to be the most thermodynamically stable in the rutile TiO$_2$ structure [7]. The signals associated to gold are also present, and they are due to the Au nanoparticles formed on top of the NWs.
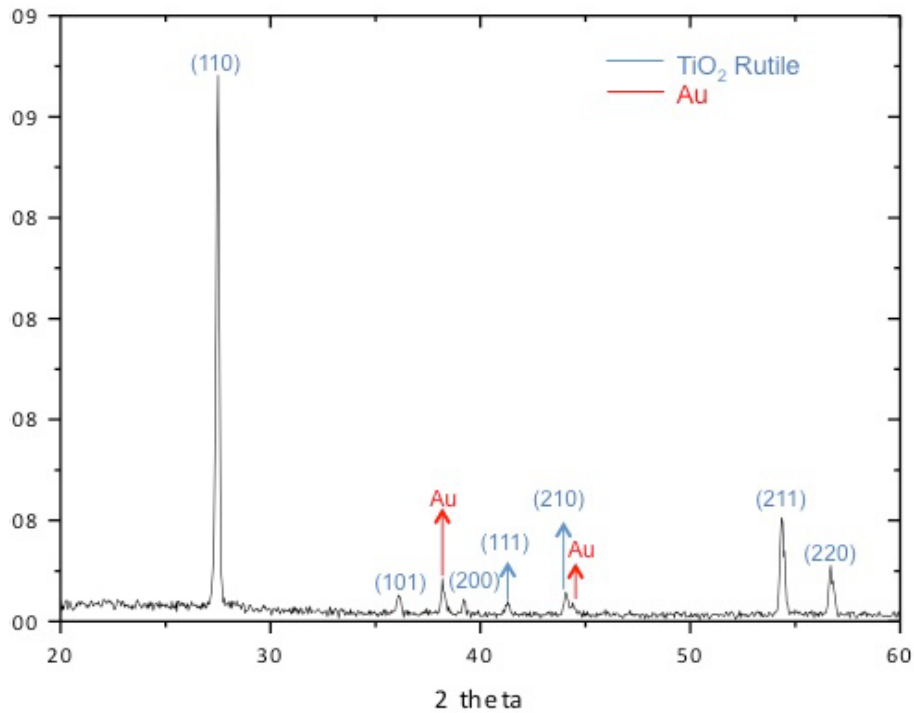
Figure 2.6 - XRD analysis of TiO₂ NWs synthetized by thermal oxidation.

Fig. 2.7 shows the TEM analysis performed on TiO₂ NWs isolated from the substrate. The diffraction pattern indicates that the NWs are pure TiO₂ monocrystalline. In diffraction conditions we were able to identify the crystal orientations of TiO₂ rutile associated with (110) and (200) planes. The NW has a quite uniform diameter of about 200 nm, which shrinks in the highest third part of the NW down to about 120 nm just at the bottom of the Au cap. In the inset of **Fig. 2.7** the crystal planes are clearly distinguishable.

Figure 2.7 – TEM image of a TiO$_2$ NW and its diffraction pattern.

2.1.3 - *In situ* SEM

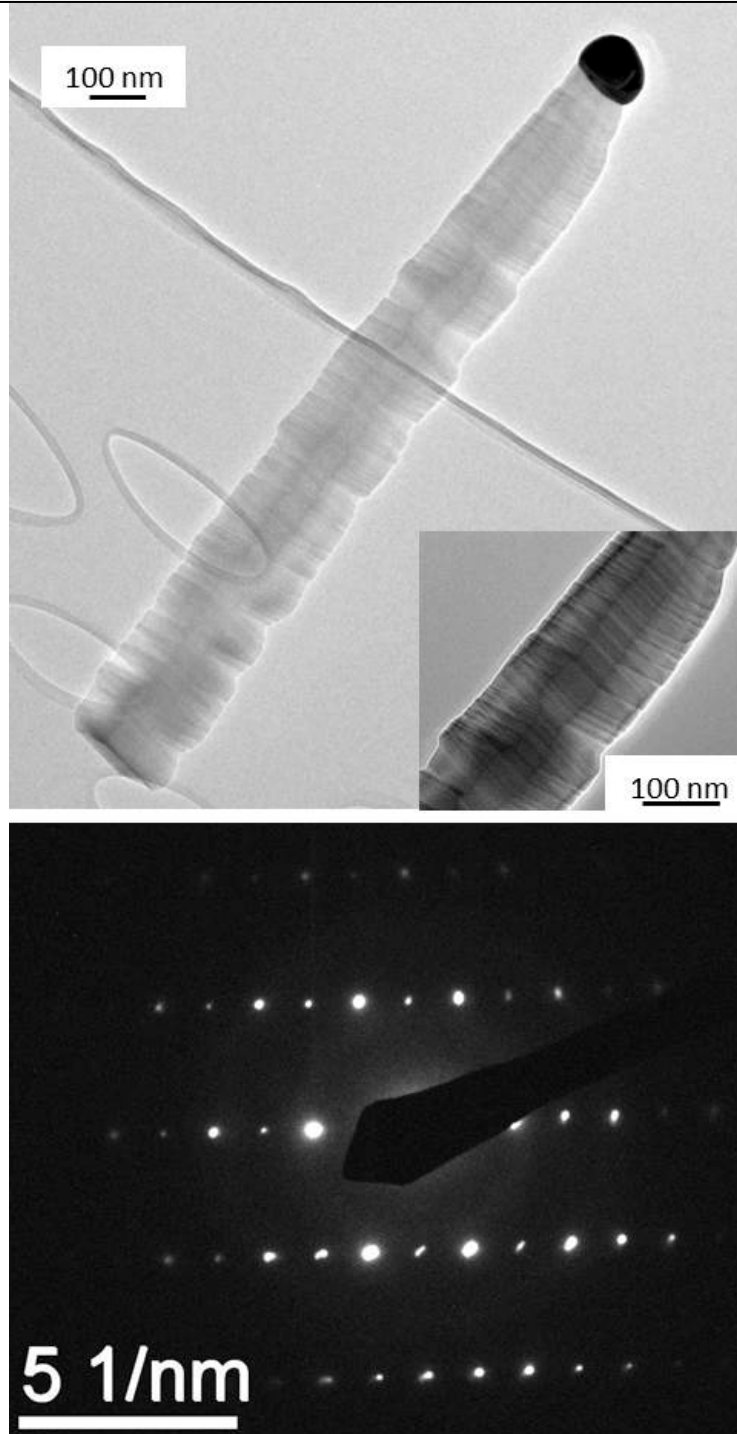In order to investigate more in detail the growth mechanism of the NWs, an in situ thermal growth was performed by means of an environmental SEM on a Ti foil substrate coated with Au thin film, as described in section 2.1.1. The sample was inserted in the SEM furnace placed inside the SEM chamber and annealed at 1000°C in water vapour atmosphere at 500 Pa.

The SEM detector showed that as soon as we started the annealing, an explosive growth of NWs occurred (length of about $\sim$ 30 μm) at sample surface. The main growth occurred in the first moments of the process so it was not easy to monitor the process. **Fig.2.8** reports a representative SEM plan view of the sample after about 30 min annealing.

Figure 2.8 – SEM plan view images of TiO$_2$ NWs synthetysed by in situ thermal growth at 1000°C in water vapuor atmosphere at 500 Pa, at an annealing time of about 30 min.
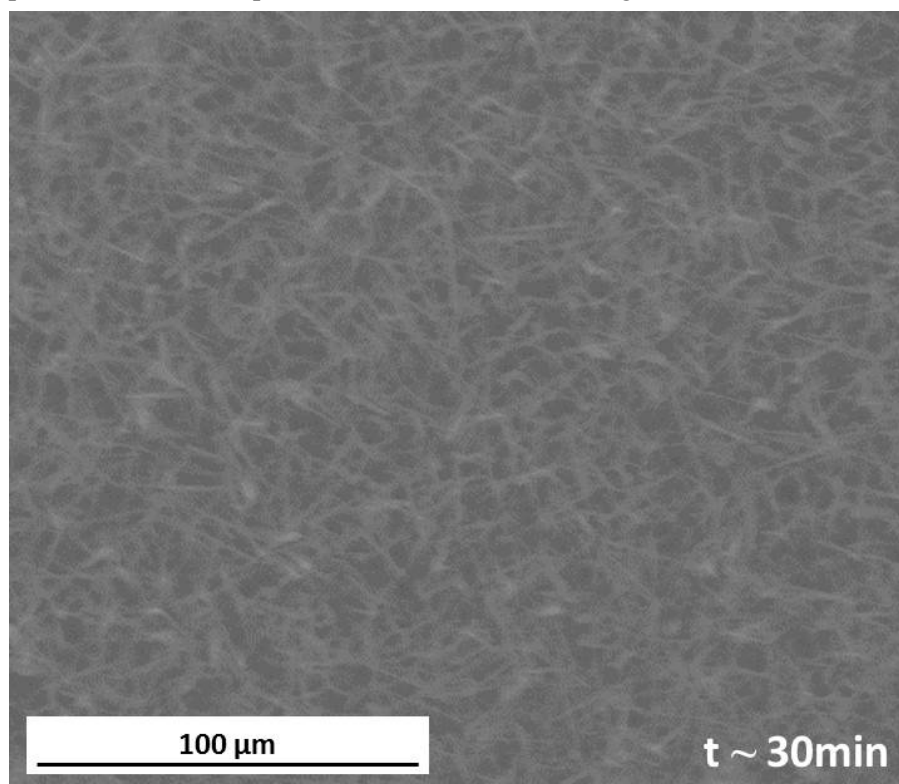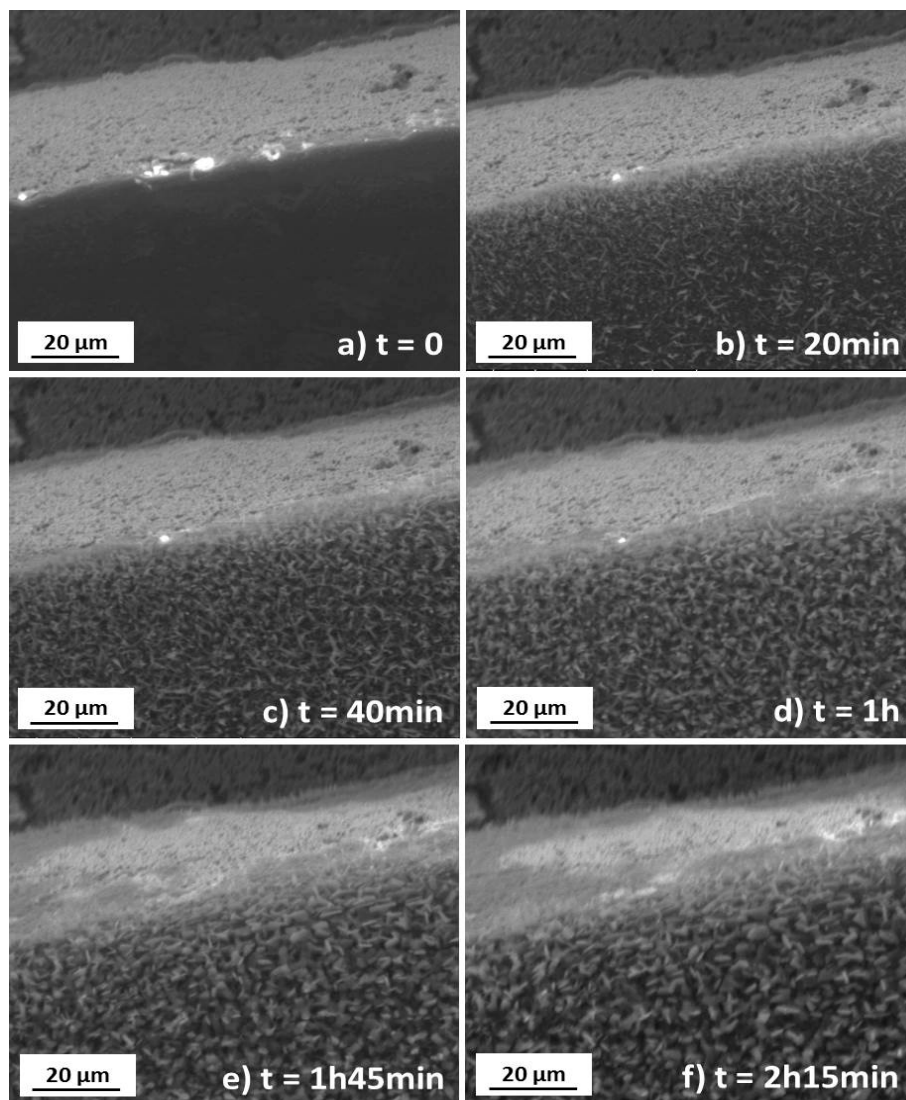
Figure 2.9 – SEM plan view images of TiO₂ NWs synthetysed by in situ thermal growth at 800°C in water vapuor atmosphere at 500Pa, at the beginning of the annealing (a) and after an annealing time of 20 min (b), 40 min (c), 1 h (d), 1h 45 min (e) and 2h 15 min (f).

Applying a lower annealing temperature of 800°C with the same conditions of atmosphere and pressure, the growth process is slower and the NWs growth dynamic can be monitored as a function of time. It was possible to obtain SEM images on average every 2 minutes for a total annealing time of 2 hours and 15 minutes.

Fig. 2.9 reports six representative images of a sample area near the edge, obtained when the annealing was just started (**Fig. 2.9**), and after different annealing times, i.e. 20 min (**Fig. 2.9** b), 40 min (**Fig. 2.9** c), 1 h (**Fig. 2.9** d), 1h 45 min (**Fig. 2.9** e) and 2h 15 min (**Fig. 2.9** f).

During the first 20-40 minutes (**Fig. 2.9** b and c), there is an higher rate of growth of NWs in length and density, with dimension up to 10-20 μm in length and up to ~10^2 nm in diameter. Afterward, during the following hour (**Fig. 2.9** d and e), the NWs tent to shorten and became wider in their base, creating a more wide rods/grains shapes, with width and length both of few microns. This is in agreement with the study of Perez [8] that reports an increased oxidation rate of Ti in annealing under water vapour in the short time; while, as the time of annealing increases, the oxidation rate decreases and it is observed the formation of dense oxide scales. Motte et al. [9] also reported an higher oxidation rate of Ti for short time of annealing under water vapour.

2.2 - Synthesis on different substrates

The synthesis of TiO$_2$ NWs was also performed on other Ti substrates different than Ti bulk foil. This allowed us to investigate the reproducibility of the growth method presented above in paragraph 2.1 while varying the substrate. We employed thin film of Ti deposited on bulk SiO$_2$, Ti thick wire (diameter of 0.2 mm) and a pre-nanostructured Ti bulk substrate. TiO$_2$ NWs grown on various substrates can be useful to favour different final applications.

2.2.1 - Thin Ti film

Ti thin films were deposited using RF magnetron sputter under UHV conditions on SiO$_2$ substrates. The base pressure was 10^{-9} mbar and the deposition was performed in Ar atmosphere at $5 \cdot 10^{-3}$ mbar, applying 400 W to a Ti target (at room temperature) for 2.5 h. The thickness of the deposited

Ti film was evaluated by RBS carried out with 2 MeV ^{4}He$^+$ beam and 165° scattering angle. Afterwards, a thin Au layer of 5 nm was deposited on the Ti film surface by means of an RF (60 Hz) Emitech K550X sputter. The deposition occurred in Ar flow at a plasma current of 10 mA for 3 minutes and with a chamber pressure of 0.02 mbar. RBS analysis was again performed to verify the thickness of the deposited Au.

The as deposited sample was then annealed in a carbolite horizontal furnace at temperatures of 700°C, for 4 hours with a mixed gas flow of argon at 1,5 lpm and oxygen at 0.1 liter per minute (lpm).

Fig. 2.10 shows the SEM images of the sputtered Ti film on SiO₂ substrate in cross-section (**Fig. 2.10a**) and plan-view (**Fig. 2.10b**), respectively. The film is porous with columnar nanostructured shape, typical of such sputtered layer [10].
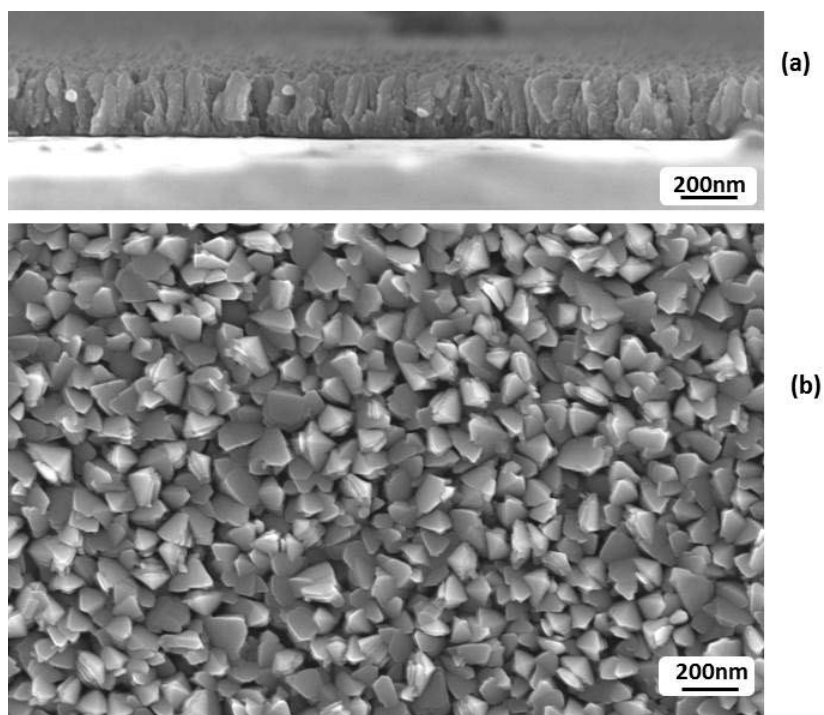
Figure 2.10 – SEM images in cross (a) and front views (b) of the Ti thin film deposited on SiO2 by UHV RF magnetron sputter

The RBS spectrum of the as deposited film is reported in **Fig. 2.11**, the experimental data (dots) have been simulated with SIMNRA [11]. We estimated a Ti film thickness of 325 ± 5 nm assuming the Ti bulk density of $5.68 \cdot 10^{22}$ at/cm^{-3}. The content of oxygen in the film is about 10% due to the native oxidize layer that is readily formed on Ti surface when exposed to air. Simulated spectrum indicated an average roughness of the Ti layer with a full width half max (FWHM) of the thickness distribution of 70 nm [11]. This roughness is due to the columnar structure of the sputtered film.

Figure 2.11 – RBS spectrum of Ti film (red dots). The blue line represents the SIMNRA simulation.

After having sputtered a thin layer of gold (5nm) on top of the Ti film, the sample was annealed at 700°C for 4 h in Ar (1.5 lpm) and O$_2$ (0.1 lpm) flow to induce the thermal oxidation of Ti. The resulting surface structure was examined by SEM analysis in cross-section (**Fig. 2.12a**) and plan-vie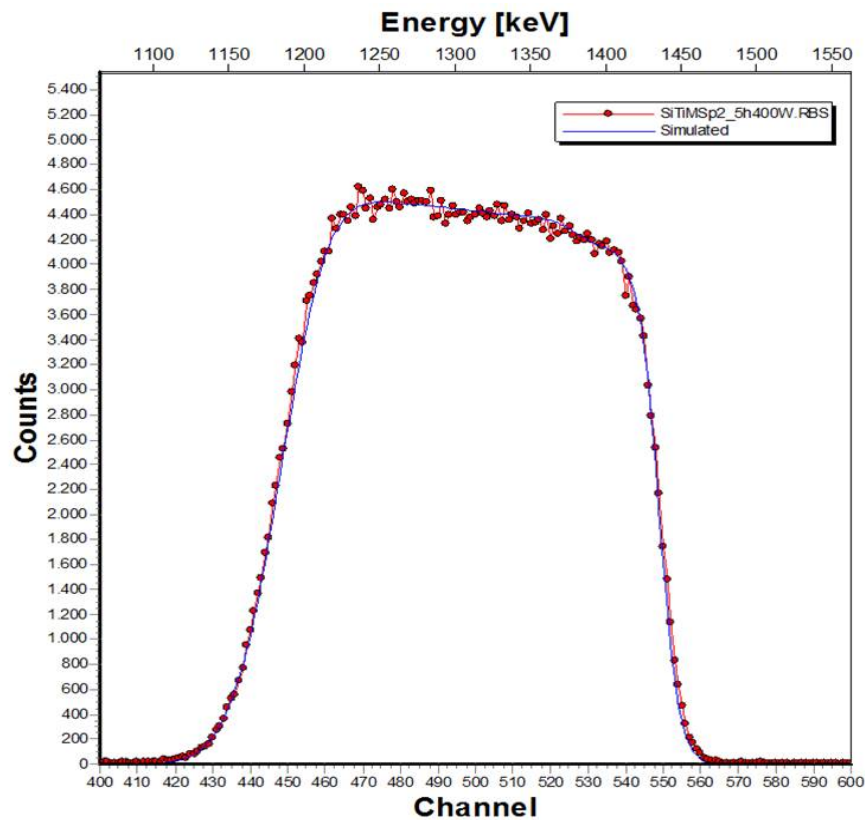w (**Fig. 2.12b**), respectively. The oxidized titanium film is reorganized along its depth in grains of size in the range of 100-500 nm clearly visible in the cross-view, but also in the background of the front-view. NWs grew on the sample surface, presenting a large distribution in size: up to 500 nm in length and up to 100 nm in diameter. They exhibited low areal density but they are uniformly distributed over the sample surface. The cross-section image indicates that the NWs are almost vertical with respect of the substrate. We identified the seed assisted growth mechanism catalyzed by the Au nanoparticles created on the surface during the annealing. Indeed, the synthesized NWs are characterized by a well distinguished metal cap on the tip of each wire. However, some Au nanoparticles did not catalyse the NWs growth and they were detected laying on the substrate surface. X-ray diffraction analysis indicated that NWs have the crystalline structure of rutile TiO$_2$, as expected since this phase is stable upon annealing at temperatures higher than 600°C [6].
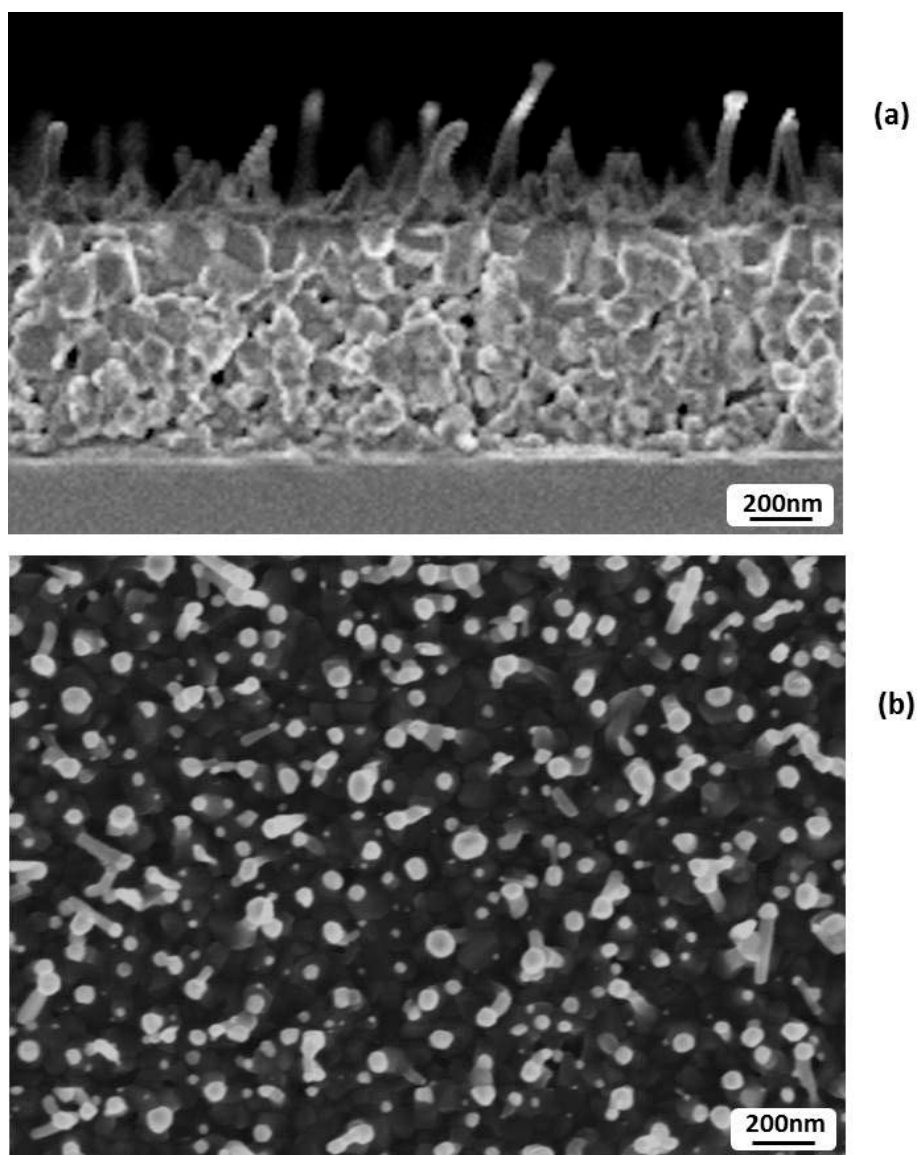
Figure 2.12 – SEM images in cross (a) and front views (b) of the TiO2 NWs grown by thermal oxidation (700°C for 4 h in Ar and O$_2$ flow) on Ti thin film substrate.

2.2.2 - Ti wire

TiO$_2$ NWs were also grown on Ti wire substrates with diameter of 0.2 mm and purity of 99.6% (Sigma Aldrich). The synthesis process was the same as the one described above for the Ti foil substrate. Regarding the Au deposition, since the diffuse transport, characteristic of sputtering, makes a full shadow impossible, the process was performed two time, on the two sides of the wire, which was flipped over by using a flat ribbon tape applied on one end of the wire. **Fig. 2.13** reports the SEM plan view of a Ti wire sample processed at 700°C for 4 h. The distribution of NWs resulted to be very dense and uniform. This effect could be due to the mechanical strain of the substrate because of the wire curvature or to the impurity of Ti wire (99.6% againt 99.9% of the Ti foil). Dinan et al. [12] reported the presence of impurities in the Ti substrate could enhance the NWs nucleation.

The length of the NWs is in the order of few μm. The inset is a low magnification image of **Fig. 2.13** showing the whole size of the annealed wire.
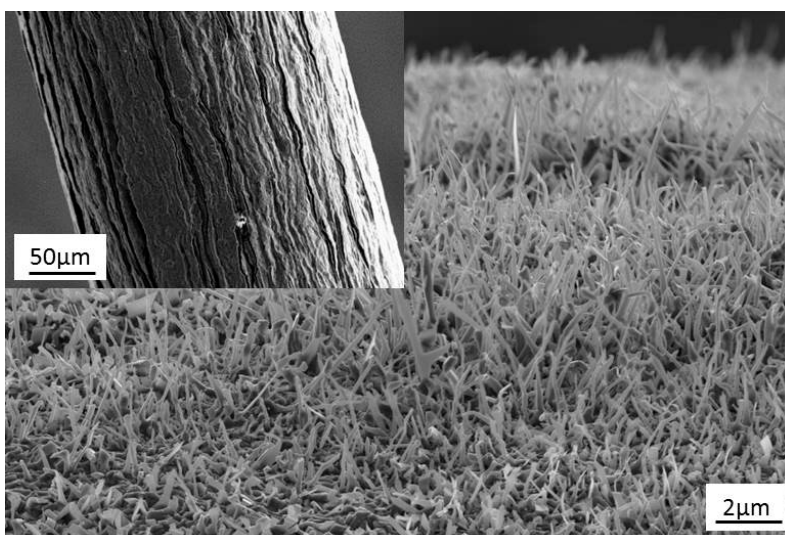

Figure 2.13 – SEM images of the TiO$_2$ NWs grown by thermal oxidation on a Ti wire substrate.

2.2.3 Ti nanospikes

In order to further enhance the surface area in contact with water and therefore to improve the degradation reactions, NWs were synthesized on a substrate with an already nanostructured surface. The substrate sample was obtained from the same Ti foil used for the NWs synthesis described in paragraph 2.1. The foil was first processed with a conventional electrochemical anodization [13] at 50 V for 30 minutes with an electrolyte containing ethylene glycol, NH$_4$F 0.1 M, and H$_2$O 1 M. After an annealing at 400°C of 2h in vacuum for crystallization, the sample was analyzed by SEM microscopy as reported in **Fig. 2.14**. The images show the layer of packed

100 nm

100 nm
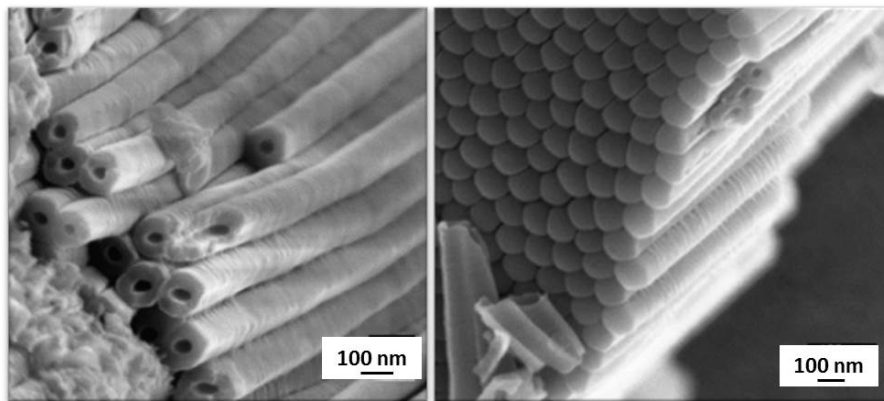
Figure 1.14 – SEM images of TiO$_2$ nanotubes grown on a Ti foil substrate by electrochemical anodization.

TiO$_2$ nanotubes formed on the foil surface. Afterward, the layer of nanotubes was removed from the foil surface by etching the sample in HF at 50% for 5 minutes. The resulting nanostructures surface is showed in the SEM images of **Fig. 2.15**. The etched nanotubes layer acted like a mold for the surface, leaving a uniformly distribution of nanospikes, which can reach high up to 400nm. On this nanostruictured substrate we synthetized TiO$_2$ nanowire by following the same thermal method employed in paragraph 2.1, i.e. with seed assisted growth.

The resulting system of TiO$_2$ nanowires on top pf the nanospikes substrate is reported in the SEM images of **Fig. 2.16**.
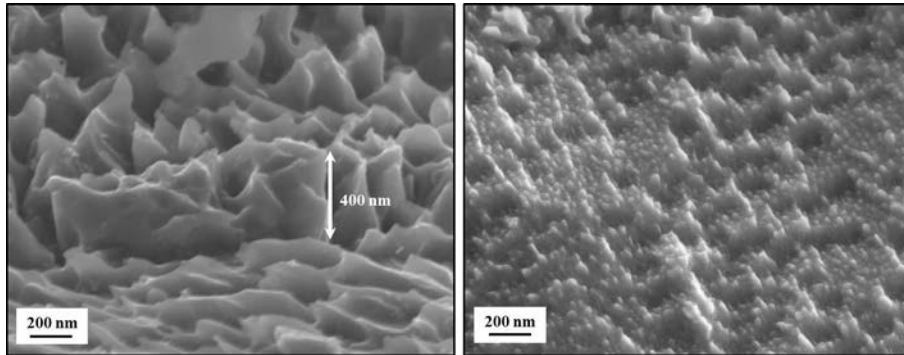
Figure 2.15 – SEM images of Nanospikes of TiO₂ obtained by electrochemical anodization of a Ti foil.
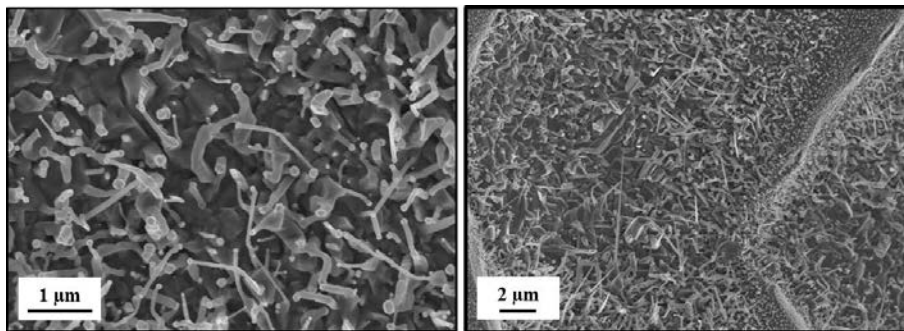
Figure 2.16 – SEM images of TiO₂ Nanowires grown on a substrates of nanospikes.

This kind of substrate could be very interesting for example for biomedical application. Ti based implants are reported as the best bio-compatible material for human surgery and artificial bio-components, the antibacterial properties of TiO₂ could be exploited in this context to avoid biofouling and maintain sterilization for example in dental or orthopedic applications, where texured material are preferred for preferential natural tissue adhesion.

2.3 – Conclusions

Thermal oxidation synthesis of TiO$_2$ NWs by seed assisted growth was performed on substrates of Ti foils coated with a thin layer of Au (3-5 nm). Annealing at temperature below 700°C revealed very rare and short NW$_S$. With increasing temperature, NWs grew in length and in density. At 1000°C a mechanism of micrograins growth appeared in competition with the NWs evolution. Increasing the annealing time to 4h amplified the effect obtained for 1h. Besides, samples annealed at temperature higher than 800°C resulted macroscopically friable. Hence, the optimal growth parameters were set at 800°C and 4h. Concerning the annealing atmosphere, an increase in gas flow rates improved the nanowires coverage, while varying the mixture of Ar and O$_2$ did not give relevant changes. The optimal gas condition resulted 7.5 lpm of oxygen and 10 lpm of argon. XRD measurements of the NWs revealed a TiO$_2$ rutile crystalline phase with a main peak of the (110) orientation. TEM analysis indicated that the NWs are pure TiO$_2$ monocrystalline. The in situ thermal growth in water vapor atmosphere at 800°C for about 2h, showed that the rate of NWs growth in length and density is higher in the first 20-40 minutes (length up to 10-20 µm); subsequently the oxidation rate decrease and the NWs tent to shorten and became wider in their base, creating a more wide rods/grains shapes (length of few µm).

At high temperature (1000°C) the surface mobility favours the 2D grain growth so we observed a decrease of NWs density. At low temperature (700°C), the nucleation process is activated but the growing rate is low so we observed very short NWs. At medium temperature (800°C) we got the best compromise.

Since NWs are not nucleated without gas carrier (in vacuum) we can conclude that the nucleation mecanism cannot be only supported by the surface migration of Ti from the substrate but a certain amount of Ti has to be transported in the gas phase. Moreover, the uniformity of NWs coverage pf the substrate improves when the gas carrier contains oxygen. This means that the formation of pure Ti NWs is not energetically or kinetically favoured in the full range of explored temperatures (600-1000 °C). According to this observation the Au-Ti phase diagram cannot be taken unto

account to depict the VLS mecanism with the help of eutectic alloys. Moreover, without catalyst the NWs growth is very difficult to be induced and controlled, only few NWs are observed in small isolated areas of the sample with no reproducibility. In conclusion, the seed assisted growth of TiO2 NWs is a very complex synthesis mecanism, as it is assisted by Ti-Au interdiffusion, Ti migration, gas carrier transport and oxygen gas reaction.

The same TiO_2 NWs growth method was also reported in other Ti substrates such as: thin film of Ti deposited on bulk SiO_2 by UHV RF magnetron sputter; Ti wire of diameter of 0.2 mm; and a Ti bulk substrate pre-nanostructured obtained first growing TiO_2 nanotubes on its surface by electrochemical anodization and then etching them with HF etching. TiO_2 NWs grown on various substrates can be useful to favour different final applications.

In the last chapter of this dissertation we are going to test if the synthetized nanostructure provided improved photocatalytic properties.

References

[1] Wagner R. S., Ellis W. C., Appl. Phys. Lett. 4 (1964) 89.

[2] C.V. Thompson, Annu. Rev. Mater. Res. 42 (2012) 399.

[3] L. Romano, V. Privitera, C. Jagadish, *Defects in Semiconductors, 1st Edition*. Multi-volume: Semiconductors and Semimetal. Elsevier, 2015.ISO 10678:2010.

[4] F. Ruffino, L. Romano, G. Pitruzzello, M. G. Grimaldi, Appl. Phys. Lett. 100 (2012) 053102.

[5] M. Chen, Y. Yue, and Y. Ju, J. Appl. Phys. 111 (2012) 104305.

[6] D. A. H. Hanaor, C. C. Sorrell, J. Mat. Sci. 46 (2011) 855

[7] Fujishima A, Zhang X, Tryk D A, Surf. Sci. Rep. 63 (2008) 515-82.

[8] P. Perez, Corrosion Sci. 49 (2007) 1172.

[9] F. Motte, C. Coddet, P. Sarrazin, M. Azzopardi and J. Besson, Oxidation of Metals 10 (1976) 113.

[10] V. Chawlaa, R. Jayaganthana, A.K. Chawlab, R. Chandrab, J. Mat. Pro. Tec. 209 (2009), 3444.

[11] M. Mayer, *SIMNRA User's Guide*, Max-Planck-Institut für Plasmaphysik, Germany, 1997-2011.

[12] Dinan B. J., Akbar S. A., Func. Mat. Lett., 2 (2009) 87-94.

[13] P. Roy, S. Berger, and P. Schmuki, Angew. Chem. Int. Ed. (2011), 50, 2904 – 2939.

Chapter 3

Doping of TiO$_2$ nanowires

One of the factors that limit the application of TiO$_2$ as an efficient photocatalyst is its wide band-gap resulting in poor absorption of light in the visible (VIS) region. The development of photocatalysts that can operate under visible light will allow the use of the main part of the solar spectrum and even the poor illumination of interior-lighting. One possible approach for solution has been to dope TiO$_2$. Asahi et al. reported that TiO$_2$ doping with nitrogen, by sputtering, shifts the optical absorption of the material to the visible range and improves its reactivity for organic molecules under VIS light illumination [1]. One year later, Khan et al. chemically synthesized, by flame pyrolysis of a Ti sheet, TiO$_{2-x}$C$_x$ with a lower band-gap than titania (2.32 versus 3.00 eV) [2]. Doping with transition metals has also been studied [3-7].

Metal ion implantation has been reported as an effective method to improve the visible light response of TiO$_2$ [3, 8, 9, 10].

In this Chapter we will illustrate the ion implantation of TiO$_2$ thin film and TiO$_2$ NWs and their morphological and structural characterization.

TiO$_2$ NWs were also thermally processed in forming gas (5%H$_2$ in N$_2$), since it has been reported in literature [11, 12] that H$_2$ treatment can induce the formation of defects (oxygen vacancies) that increase the donor density, promoting the conductivity and favoring the photoefficiency. We will present and discuss the effects produced by the iron implantation and forming gas treatments on TiO$_2$ samples.

The electrical and photocatalytic properties of these samples will be analysed in the following Chapetr 4 and Chapter 5, respectively.

3.1 - Fe ion implantation

In the ion implantation process [13], commonly used in the microelectronic industry, the titania is bombarded with metal ions. Although metal ion-implanted TiO$_2$ (commonly called "second-generation photocatalyst") is currently believed to be one of the most effective photocatalyst for solar energy utilization, the operative mechanism together with the photocatalytic performance of the material is not yet clear (see Ref. 3, p. 24). For example, Yamashita *et al.* studied Fe-doped bulk TiO$_2$ realized by ion-implantation or the sol-gel method [8]. They observed in the case of the chemical doping by sol-gel only a small shift of the absorption band to the visible light regions, in contrast with the larger shift observed for doping with the ion-implantation method. X-ray absorption fine structure analysis suggested that the substitution of Ti atoms in the TiO$_2$ lattice with implanted metal ions is important in modifying the TiO$_2$ for the absorption of VIS light [8]. Anpo *et al.* investigated Cr ion-implanted TiO$_2$ and observed a shift of the absorption band towards the visible light region [9]. They attributed the VIS shift to a modification of the electronic properties of bulk TiO$_2$ by the implanted metal ions [9]. The authors also excluded a mechanism in which the ion-implanted metals act as electron-hole recombination centers [9]. In this section, we investigate the effect of Fe$^+$ implantation into TiO$_2$ samples.

3.1.1 – Fe ion implantation in TiO$_2$ thin film

Titanium layers, $\sim$ 100 nm thick, were deposited on quartz substrates by sputtering at room temperature. Then, the Ti layers were annealed at 600 °C for 30 min in a conventional furnace under a controlled O$_2$ flux, in order to induce the complete oxidation of the titanium layer in TiO$_2$ [14].

The samples were implanted with Fe$^+$ ions at 80 keV. The energy was chosen, [15] such that the iron implanted profile was fully contained within the TiO$_2$ layers (Fe projected range of $\sim$ 40 nm). The implanted fluence were 2 x 10^{16} cm^{-2} or 5 x 10^{15} cm^{-2}, so as to produce an iron doping of 5% and 1% by atomic weight. The fluence were fixed as the existing

literature suggests that a high concentration of metals is necessary in order to realize a second-generation photocatalyst [3,8–10]. During implantation, the average current density was ~ 0.1 $\mu A/cm^2$, and the substrates were held at room temperature. Afterwards, some samples were annealed at 450 or 550 °C for 2 h in an Ar atmosphere, so as to reduce the damage induced by the ion-implantation process.

The crystallographic morphology was investigated by transmission electron microscopy (TEM) in a cross sectioned sample, by using a JEOL JEM-2010 F microscope operated at 200 keV. The structure of the films was studied by X-Ray Diffraction (XRD) analyses with a Bruker D-500 diffractometer at several angles of incidence, from 0.8° to 1.0°, and Θ-2Θ from 20° to 60°. The XRD spectra were analyzed by a Bruker software suite, including the ICSD structure database. The UV-VIS optical characterization was obtained by extracting both the normal transmittance (T) and the 20° reflectance (R) spectra in the 200–800 nm wavelength range, by using a Varian Cary 500 double beam scanning UV/VIS/NIR spectrophotometer.

The as implanted samples showed a polycrystalline structure with an average grain size of ~ 30 nm, as revealed by the TEM analysis reported in **Fig. 3.1**, reporting cross-section images in bright and dark field, where the bright area represent the different crystalline domains.

The XRD patterns of the starting TiO₂ film, as-implanted and after the thermal treatments are reported in **Fig. 3.2(a)** for the iron fluence of 2 x 10^{16} cm^{-2}, and in **Fig. 3.2(b)** for the iron fluence of 5 x 10^{15} cm^{-2}. The XRD analyses only detected the presence of the anatase and rutile crystalline phases. No peaks related to the Fe_2O_3 or Fe_xTiO_y phases were found in the XRD patterns. Un-implanted films were found to crystallize at 600 °C into anatase and rutile phases. The ion-implantation induced a reduction of the XRD peak intensities, which increases with the fluence. The observed
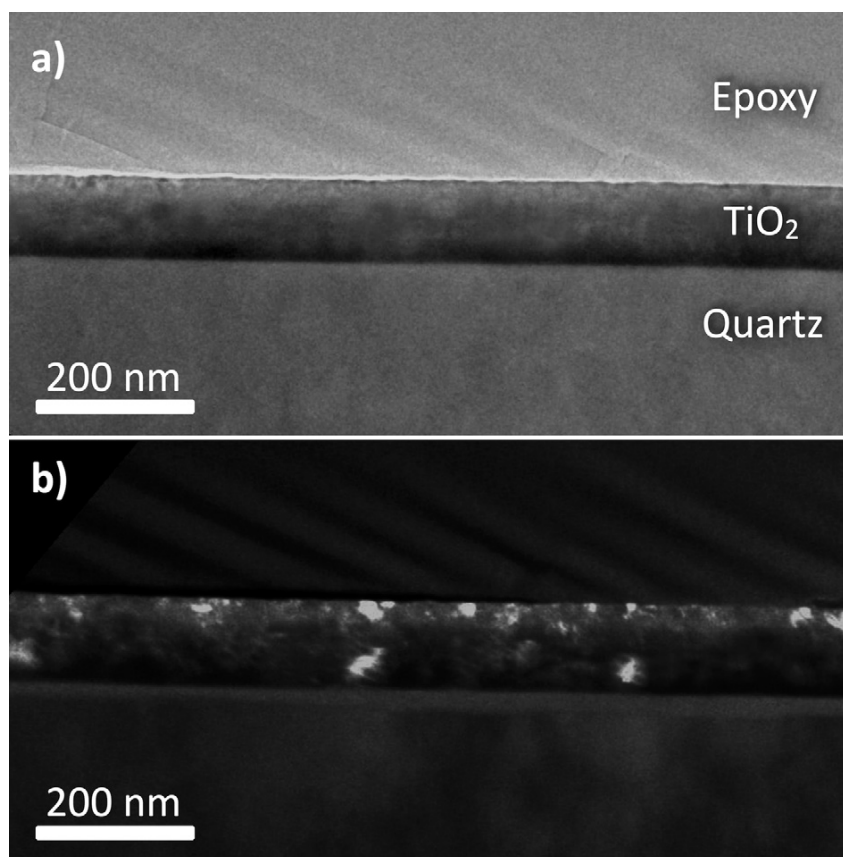
Figure 3.1 - Cross-sectional TEM images of the TiO$_2$ film implanted with Fe (2 x 10^{16} cm^{-2} at 80 keV). (a) Bright field image showing a continuous polycrystalline TiO$_2$ film. (b) Dark field image of the same portion of figure (a); here, the bright contrast regions indicate the presence of different crystal domains due to the polycrystalline nature of the TiO$_2$ layer [16].

decrease in the intensity can be correlated to a damaging process, typical of ion-implantation [13]. The thermal treatments induced, as expected, a damage recovery that was complete for the lower fluence but only partially for the higher fluence. In addition, the annealing at 550 °C promoted the recovery of the rutile phase [17].

Fig. 3.3 reports the absorbance for the pure TiO$_2$ film, an as-implanted sample and a sample after the thermal treatments, for the iron fluence of 2 x 10^{16} cm^{-2} (a) or 5 x 10^{15} cm^{-2} (b). The absorbance (A) was

obtained from the transmittance (T) and reflectance (R) spectra: A% = 100 – T% – R%. The reference sample (i.e., the pure TiO$_2$ film) shows the typical optical absorption in the UV part of the spectrum, for wavelengths shorter than 387 nm (line plus closed circles in **Fig. 3.3**). In addition, the iron-implanted films show a remarkable absorption in the VIS part of the spectrum, in the form of a shoulder peak. In detail, the as-implanted samples exhibit an absorbance of ~ 28% and ~ 12% for the high and low fluence,
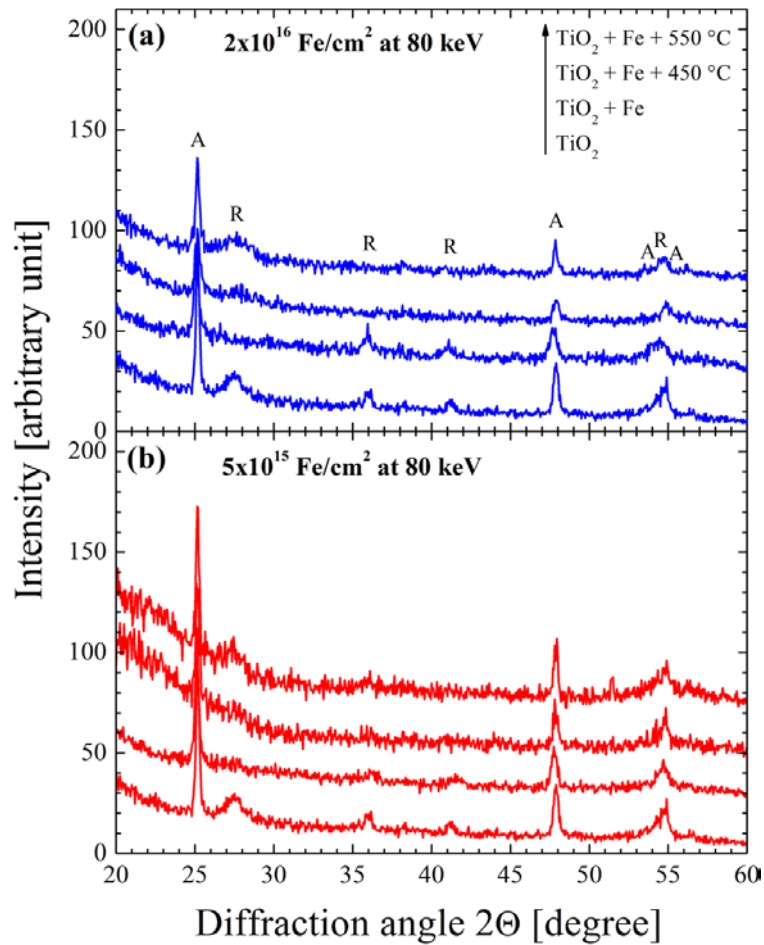
Figure 3.2 - XRD patterns of the pure TiO$_2$ film, as-implanted and after the thermal treatments for the Fe$^+$ fluence of 2 x 10^{16} cm^{-2} (a) or 5 x 10^{15} cm^{-2} (b) at 80 keV [16].

respectively, indicating a correlation between the ion fluence and the absorbance of the materials in the VIS. With annealing, the observed trend, for both the fluences, is a decrease of the absorption band in the VIS (see continuous and dashed lines in **Fig. 3.3**).

Although doped-TiO$_2$ has attracted remarkable interest in the recent years, there is not yet a clear explanation for the mechanism responsible for
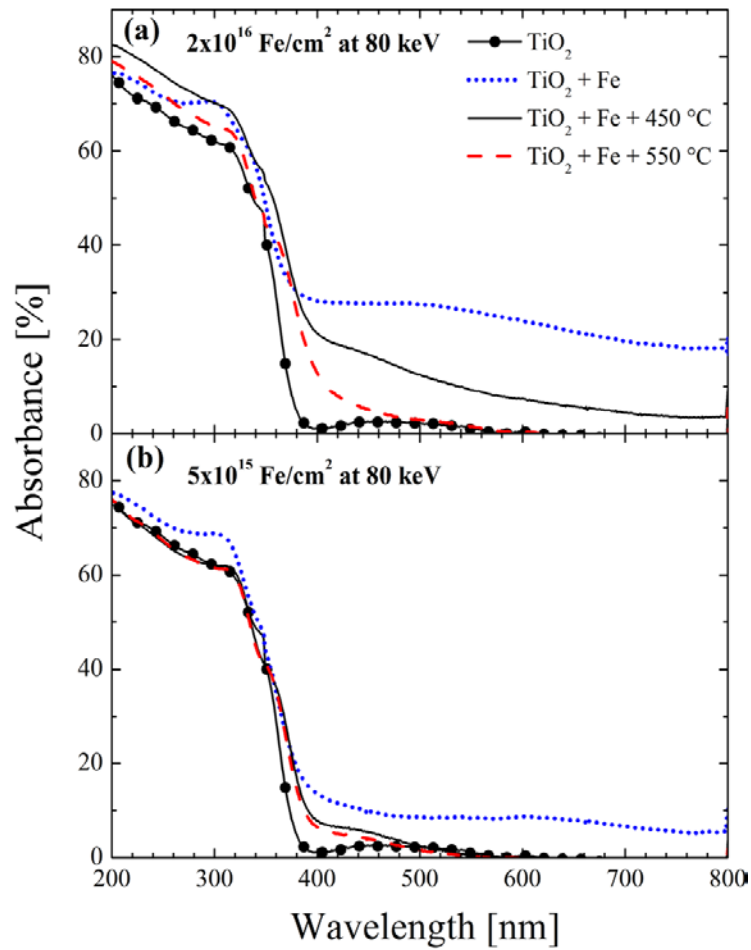

Figure 3.3 – Absorbance spectra of the pure TiO$_2$ film, as-implanted and after the thermal treatments for an Fe$^+$ fluence of 2 x 10^{16} cm^{-2} (a) or 5 x 10^{15} cm^{-2} (b) at 80 keV [16].

the VIS response, as mentioned above. The obtained results suggest that ion implantation causes a beneficial damage effect in the TiO$_2$ film (see the XRD measurements reported in **Fig. 3.2**), in good agreement with the literature data (see, for example, Refs. 27G and 29G). We suggest that this damage can induce energy levels in the TiO$_2$ energy band structure, which are responsible for the observed ability of the implanted films to absorb VIS light (see optical measurements reported in **Fig. 3.3**). In particular, for higher damage we observe higher VIS absorbance (compare results in **Fig. 3.2** and **Fig. 3.3**). We wish to underline that, differently from the results of Yamashita et al. [8], our study on damage indicates that implanted metal ions do not substitute Ti in the TiO$_2$ matrix, but occupy interstitial positions in the lattice. In addition, our optical measurements indicate the formation of a new absorption band in the VIS part of the spectrum, which is also different from the shift of the absorption band of the doped titania towards the visible light region observed by Yamashita et al. and Anpo et al.[8, 9]. By using our optical measurements, we also estimated [16] a lowering of the band gap energy of the Fe$^+$ implanted samples to around 1.6 - 1.9 eV, which are among the lowest values ever reported in the literature.

3.1.2 – Fe ion implantation in TiO$_2$ NWs

A similar iron implantation process as the one performed on the Ti thin film sample was also carried out in TiO$_2$ NWs. The NW growth was described in Chapter 2 in detail. The TiO$_2$ NWs used for iron implantation were grown on Ti foil by the thermal oxidation seed assisted method at 700°C for 4h in an Ar and O$_2$ mixed flow. We choose an Fe$^+$ ions energy of 20 keV corresponding to a Fe projected range of ~ 13 nm [15], in order to obtain an iron implantation profile fully contained within the TiO$_2$ NWs thickness, considering a NWs average diameter of 30-50 nm (see SEM images in Chapter 2). The Fe$^+$ implantation was carried out at two different fluence, namely 1.3 x 10^{15} cm^{-2} and 6.5 x 10^{14} cm^{-2} corresponding to an iron doping of 0.5% and 1% by atomic weight, respectively. The two implantation conditions as stated above, were simulated using SRIM [15] in normal incidence on the foil surface and are shown in **Fig. 3.4**. The average implantation current density was ~ 0.06 µA/cm^2, and the substrates were

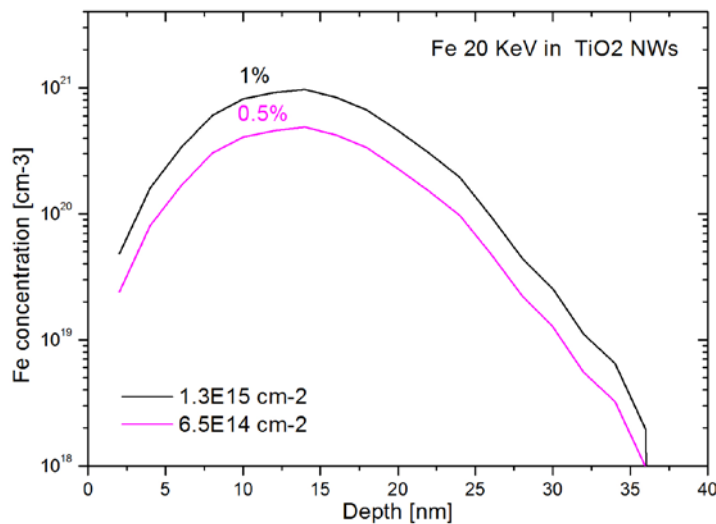**Figure 3.4** – SRIM simulation [15] of 20 keV Fe$^+$ ion implantation in TiO$_2$ two fluences: 1.3 x 10^{15} cm^{-2} (black line) and 6.5 x 10^{14} cm^{-2} (pink line) corresponding to an iron doping of 0.5% and 1% by atomic weight, respectively.

held at room temperature. Nanowires have no preferential direction with respect to the substrate and also the substrate being a metal foil is atomically flat, so the angle dependence of the ion implantated profile has not been taken into account in the simulation.

After the ion implantation, the morphology of the NWs sample was analysed by SEM microscopy, in order to check if the implantation process induced any modification. We observed a strong effect in the bending of many NWs after the implantation. **Fig. 3. 5** reports two high-resolution SEM images of an as-implanted sample at a fluence of 1.3 x 10^{15} cm^{-2}, showing two representative NWs bent**.** A similar effect has been observed in the TiO$_2$ NWs implanted at the lower fluence of 6.5 x 10^{14} cm^{-2}. **Fig. 3. 6** shows two SEM images of an as-implanted sample at a fluence of 6.5 x 10^{14} cm^{-2}. In the top image we can observe the bending effect even in long NWs (3-4 μm in length), which show a smaller bending curvature, compared to the shorter NWs of **Fig. 3. 5** Moreover, the facets of the NWs after the implantation appear less sharp and more smooth probably because of the sputter effect induced by the ion beam. This effect is visible in the bottom image of **Fig. 3.6.**

Other works have already studied NWs bending due to ion implantation [18, 19], showing, for instance, that Si and Ge NWs implanted with Ge and Ga ions amorphize and bend toward the impinging ions, modifying their structure in such a way as to minimize the exposed surface to the beam [18]. Romano *et al.* [19] demonstrated a simple method to reversibly control the shape and the orientation of Ge nanowires using Ga^{+} ion beams: viscous flow and plastic deformation occurred causing the nanowires to bend toward the beam direction. The bending was reversed multiple times by ion implanting the opposite side of the nanowires, resulting in straightening and subsequent bending into that opposite direction, demonstrating that a detailed manipulation of nanoscale structures is possible through the use of ion irradiation.

In the case of TiO$_2$ NWs, further analyses are required to determine the effectiveness of doping or defects engineering by ion implantation in comparison to thin film implantation and damage recovery in order to activate the photocatalytic effect.
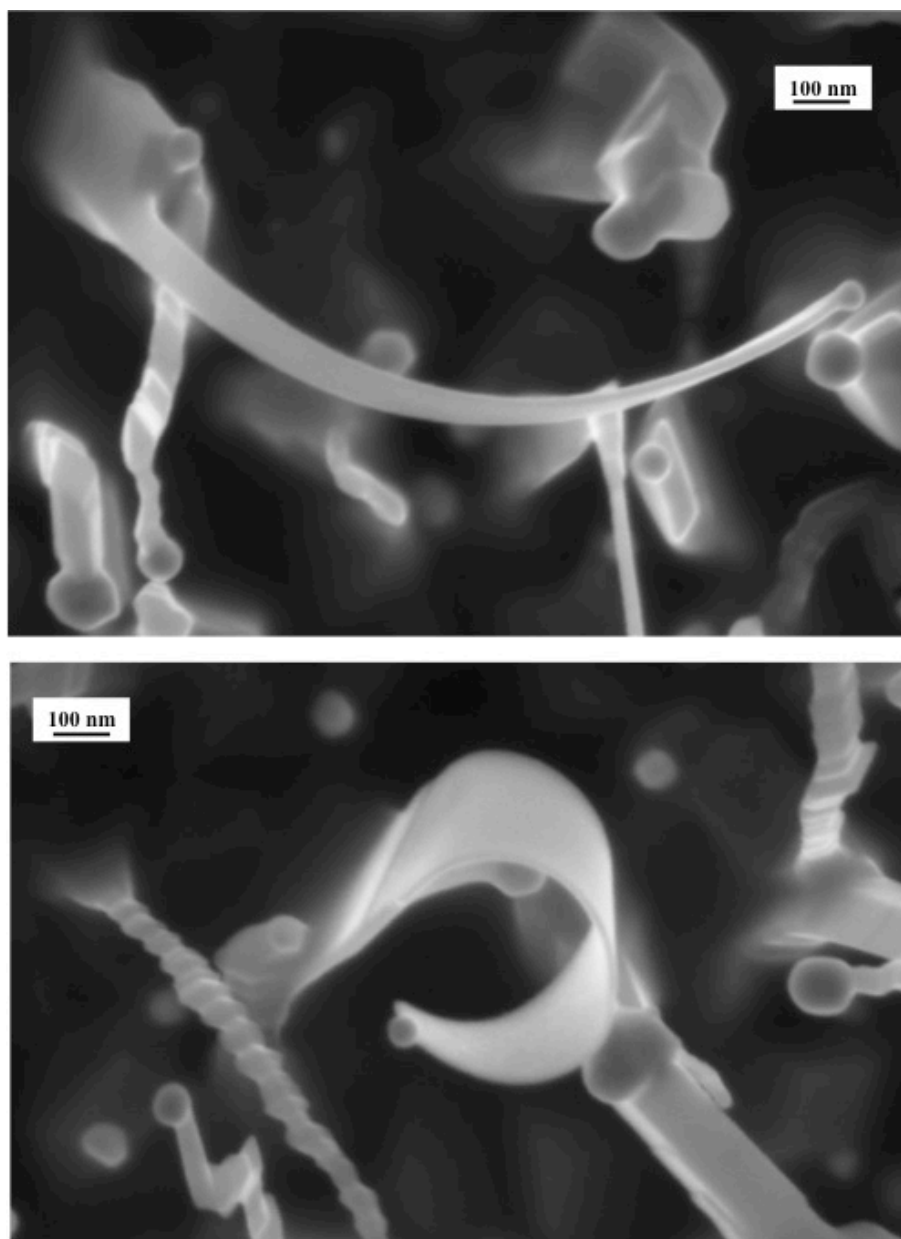
Figure 3.5 – High magnification SEM images of TiO$_2$ NWs grown on Ti foil and bent after a Fe$^+$ implantation at a fluence of 1.3 x 10^{15} cm^{-2}.
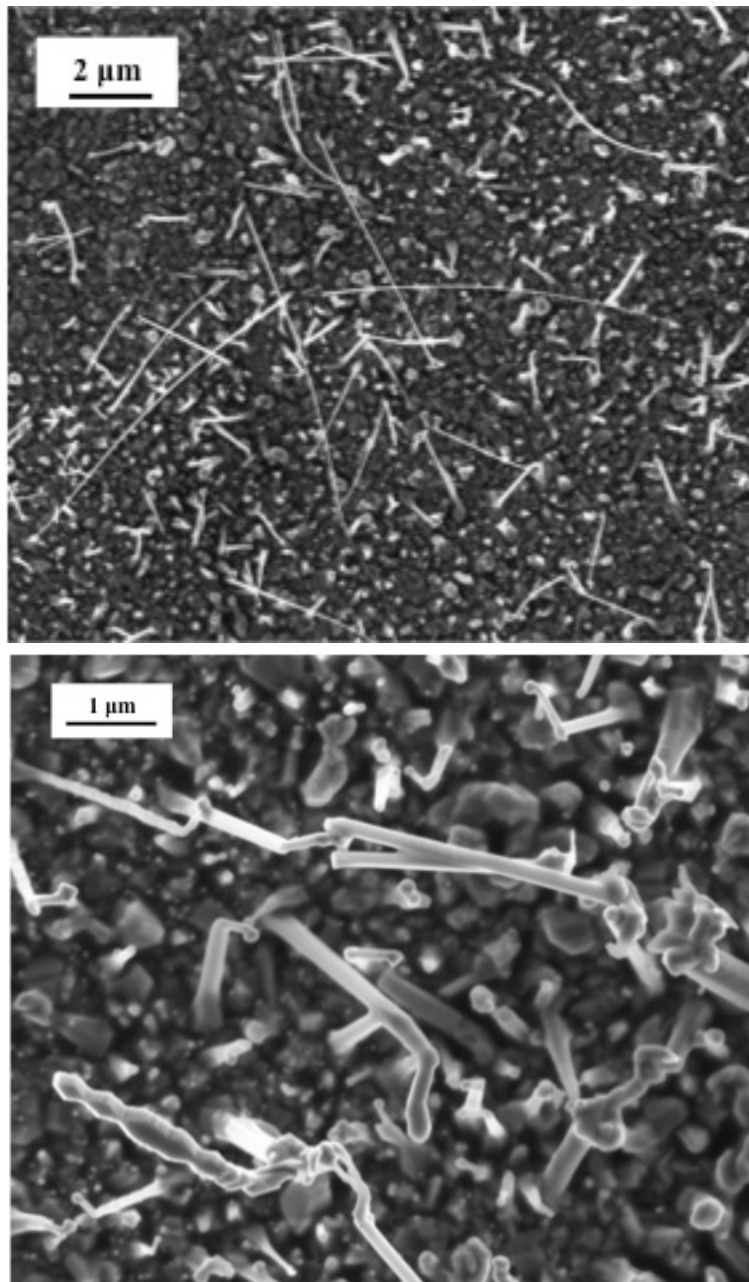
Figure 3.6 – SEM images of TiO$_2$ NWs grown on Ti foil and bent after a Fe$^+$ implantation at a fluence of 6.5 x 10^{14} cm^{-2}.

3.2 – Forming gas treatment of TiO$_2$ NWs

It has been reported in literature that annealing in an atmosphere of mixed H$_2$ in N$_2$ (i.e. forming gas) can increase the photoefficiency of TiO$_2$ by the formation of oxygen vacancies, which increase the shallow donor density, promoting the conductivity and improving the charge collection [11, 12]. Therefore, we wanted to investigate the effect produced by the forming gas annealing on the TiO$_2$ NWs especially in the electrical and photocatalytic properties.

For this purpose, we prepared a sample of TiO$_2$ NWs grown on Ti bulk by thermal seed assisted method (illustrated in detail in Chapetr 2) at the previously defined optimal conditions of 800°C annealing for 4h in a mixed flow of Ar 10 lpm and O$_2$ 7.5 lpm. Then, we carried out an additionally annealed in forming gas (5% H$_2$ in N$_2$) at 500°C for 2h of the NWs sample in order to promote the formation of oxygen vacancies and the hydrogen passivation of dangling bonds and the consequential increase of the carrier density.

Afterward, we analyzed the sample by SEM in order to observe if any morphology change after the annealing process occurred. The SEM images did not report any visible modification in the NWs structure comparing them before and after the forming gas annealing, indicating that this thermal process did not affect the surface morphology of the samples. This was also confirmed by the reflectance measurement reported in **Fig. 3.7.** The measurements were carried out by means of the spectrophotometer Lambda 40 Perking-Elmer equipped with an integrating sphere. The plot show the reflectance of the TiO$_2$ NWs and of the same sample after the forming gas annealing. The measurement of a bulk TiO$_2$ without NWs is also reported as reference. As expected, all curves display an important decrease in reflectance (i.e. increase in absorbance) at a wavelength 410 nm, compared to higher wavelengths, corresponding to the energy bandgap of the rutile TiO$_2$ (Eg = 3.03 eV). The two samples of NWs, with and without forming gas treatment, exhibit the same values of reflectance for wavelengths < 410 nm and a very small difference of 2-3% of reflectance for values above 410 nm. Therefore, structural differences of the surface of the

two samples, which would have brought different (anti-) reflective effect, are excluded especially in the UV range of energy higher than the bandgap energy where the samples are expected to be active in the photocatalytic processes.
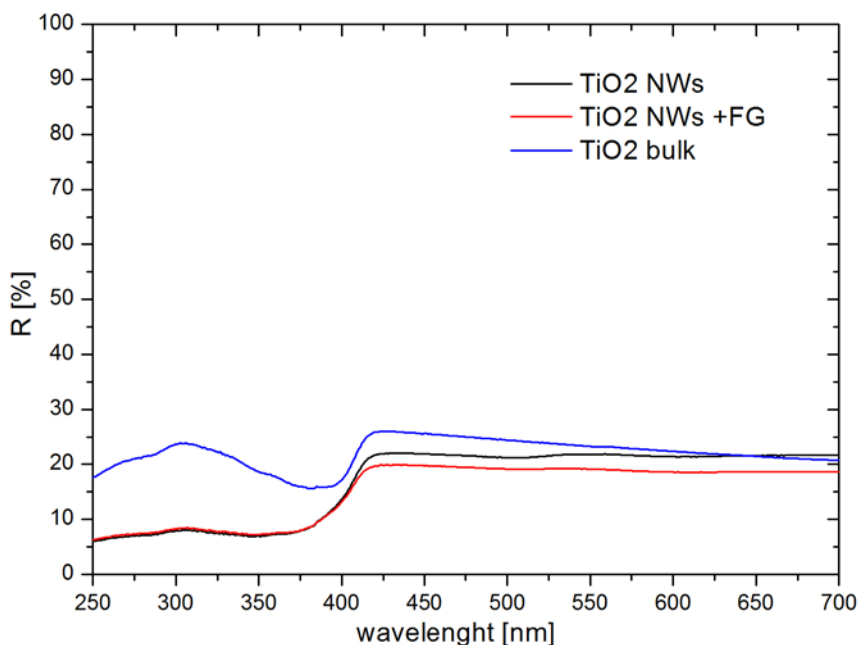
Figure 3.7 – Reflectance measurement of the TiO$_2$ NWs before (black line) and after (red line) an additional annealing in forming gas (5% H$_2$ in N$_2$) at 500°C for 2h. The reflectance of a bulk TiO$_2$ without NWs is also reported as reference.

The defect evolution due to the forming gas annealing was studied by electrical characterization using deep level transient spectroscopy, and it will be illustrated in detail in Chapetr 4. Wheras, the photocatalytic results on the NWs treated in forming gas will be presented in Chapter 5.

3.3 - Conclusions

Our experimental results clearly demonstrate that a small effective band-gap (1.6–1.9 eV) can be achieved by Fe$^+$ irradiation of TiO$_2$ films, and an increase in photocatalytic efficiency can be obtained under VIS light

irradiation. Particular attention should be paid to the process, which relies on implantation-induced defects to form energy levels inside the band-gap of the material, but it is crucial to keep their amount below a certain limit, as they act as recombination centres for electrons and holes. We demonstrated that the implantation of a 100 nm thick TiO$_2$ film with Fe$^+$ at 5 x 10^{15} cm^{-2}, 80 keV induces an absorbance of ~ 12% for VIS light (see **Fig. 3.Abs(b)**), with an effective band-gap lowering from 3.2 eV to 1.6–1.9 eV, without the help of any additional thermal treatments. The same work could extended to TiO$_2$ nanowires by tuning the ion implantation energy in order the ion implanted profile is mostly within the average NWs section. NWs showed bending like in the case of ion implanted Si and Ge nanowires.

TiO$_2$ NWs were also treated with an annealing in forming gas (5%H$_2$ in N$_2$) at 500°C for 2h in order to promote the formation of oxygen vacancies and the hydrogen passivation of dangling bonds and the consequential increase of the carrier density, as it was already suggested in literature [11, 12]. The NWs were analysed by SEM and they did not show any morphological modification due to the forming gas annealing. In addition, reflectance measurements showed that they report the same (anti-)reflective behavior especially in the wavelength region of the UV where they are expected to be active for the photocatalysis. In Chapetr 5 we will present the results of the photocatalytic analysis of the iron implanted TiO$_2$ NWs and the forming gas treated TiO$_2$ NWs samples.

References

[1] R. Asahi, T. Morikawa, T. Ohwaki, K. Aoki, and Y. Taga, Science 293, 269 (2001).

[2] S. U. M. Khan, M. Al-Shahry, and W. B. Ingler, Jr., Science 297, 2243 (2002).

[3] S. Malato, P. Fernandez-Ibanez, M. I. Maldonado, J. Blanco, and W. Gernjak, Catal. Today 147, 1 (2009).

[4] X. Chen and S. S. Mao, Chem. Rev. 107, 2891 (2007).

[5] M. I. Litter, Appl. Catal. B 23, 89 (1999).

[6] S. Zhang, Y. Chen, Y. Yu, H. Wu, S. Wang, B. Zhu, W. Huang, and S. Wu, J. Nanopart. Res. 10, 871 (2008).

[7] J. Yu, Q. Xiang, and M. Zhou, Appl. Catal. B 90, 595 (2009).

[8] H. Yamashita, M. Harada, J. Misaka, M. Takeuchi, B. Neppolian, and M. Anpo, Catal. Today 84, 191 (2003).

[9] M. Anpo and M. Takeuchi, J. Catal. 216, 505 (2003).

[10] L. Z. Qin, H. Liang, B. Liao, A. D. Liu, X. Y. Wu, and J. Sun, Nucl. Instrum. Methods Phys. Res., Sect. B 307, 385 (2013).

[11] C. Fàbrega, T. Andreu, F. Guell, J.D. Prades, S. Estradé, J.M. Rebled, F. Peirò and J.R. Morante, Nanotechnology, 22 (2011) 235403.

[12] G. Wang, H. Wang, Y. Ling, Y. Tang, X. Yang, R. C. Fitzmorris, C. Wang, J. Z. Zhang and Y. Li, Nano Lett., 11 (2011) 3026-3033.

[13] E. Rimini, Ion Implantation: Basics to Device Fabrication (Kluwer Academic Publishers, Boston, 1995).

[14] D. Velten, V. Biehl, F. Aubertin, B. Valeske, W. Possart, and J. Breme, J. Biomed. Mater. Res. 59 (2002) 18.

[15] J. F. Ziegler, J. P. Biersack, and U. Littmark, The Stopping and Range of Ions in Solids (Pergamon, New York, 1984), Vol. 1; see http://www.srim.org for The Stopping and Range of Ions in Solids.

[16] G. Impellizzeri, V. Scuderi, L. Romano, P.M. Sberna, E. Arcadipane, R.Sanz, M.Scuderi, G. Nicotra, M. Bayle, R. Carles, F. Simone and V. Privitera, J. Appl. Phys., Vol. 116 (2014) pp.173507,

[17] D. A. H. Hanaor and C. C. Sorrell, J. Mater. Sci. 46 (2011) 855.

[18] Pecora E. F., Irrera A., Boninelli S., Romano L., Spinella C., Priolo F., Appl. Phys. A, Vol. 116, Issue 1, pp 13-19, 2010

80

[19] L. Romano, N.G. Rudawski, M.R. Holzworth, K.S. Jones, S.G. Choi, S.T. Picraux, J. Appl. Phys. 106, 114316 (2009).

Chapter 4

Electrical properties

Defects are crucial for the electrical properties of semiconductor materials. Indeed, a perfect single crystal semiconductor without any defects will have limited free carriers and thus a low intrinsic conductivity. Defects are necessary to supply charge carriers in the semiconductor making the material conducting and, in the domain of photocatalytic application, this can strongly improve the material performance. Moreover, unintentional introduction of defects can occurs especially during the growth and processing of the materials, and may drastically affect their electrical characteristics. Therefore, control of the defects is a key issue and allows to tune the properties of semiconductors.

4.1 - Defects in TiO_2

The defects present in a crystal, distort the periodic potential and may introduce additional electronic states. Depending on the energy position of the electronic states, the defects can be either electrically active or inactive. An electrical active defect will introduce additional discreet levels in the electronic band gap of the semiconductor and, will have different characteristics depending on the location of these levels in relation to the conduction and valence band. States located close to the conduction band, i.e. shallow levels, are usually applied for doping the semiconductor. Whereas, levels that reside further away from the band edges, i.e. deep levels, may act as generation/recombination centers.

The defect energy levels introduced in the band gap can trap the charge carriers. Considering a defect having a level in the electronic band

gap with a trap concentration N_t and an energy position E_t below the conduction band edge, E_c. According to the Shockley-Read-Hall statistic [1,2], the electron and hole from the conduction and valence band, respectively, can be captured or emitted by a defect level in the band gap, as illustrated in **Fig. 4.1**. These processes are controlled by the capture $(c_{n,p})$ and emission $(e_{n,p})$ rates. Depending on the position of the defect in the band gap and the values of the emission and capture coefficients, different process will dominate. For example, generation of electrons occurs when e_n and e_p are dominant, recombination when c_n and c_p are dominant and, trapping of
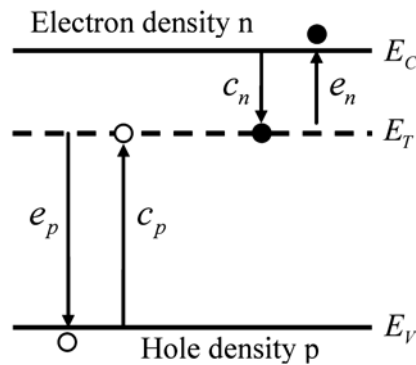
Figure 4.1 – Illustration of the capture $(c_{n,p})$ and emission rate $(e_{n,p})$ processes of electrons and holes from the conduction band and valence band respectivelym for a defect.

carrier when e_n and c_n are dominant.

Regarding the defects in TiO_2, oxygen vacancy is considered one of the most important and is supposed to be the prevalent defect in many metal oxides [3]. Oxygen vacancies in metal oxides have been extensively investigated both by theoretical calculations and experimental characterizations [4-7]. It has been revealed that oxygen vacancies can behave as important adsorption and active sites for heterogeneous catalysis, which are able to strongly influence the reactivity of metal oxides [5].

In TiO_2 when an oxygen vacancy is created, the electrons associated with the lattice O atom removed from the structure are transferred to the empty *3d* levels at the bottom of the conduction band belonging to the adjacent Ti atoms [8]. Since the *3d* states are rather localized, this corresponds to a change of the formal oxidation state, from Ti^{4+} to Ti^{3+}.

In general, defects levels in the band gap can be characterized both by electrical or optical techniques. The latter ones, include for instance photoluminescence (PL) and cathodoluminescence and can give information about various charge carrier transitions, such as band-to-band, localized-state-to-band and between interval states of a defect. Among the electrical methods there are the deep level transient spectroscopy (DLTS), and the thermal admittance spectroscopy (TAS), which are based on a junction spectroscopy technique.

In this dissertation, the electrical properties of the TiO_2 samples are investigated employing the DLTS technique [9], which is a well known capacitance method used in the characterization of defects in the band gap of semiconductors.

The main issue of electrical and optical characterizations of nanostructures is related to the technical difficulties of isolating the nanostructures and at the same time collecting enough signal to obtain significant measurement. When measurements are realized on bulk samples where NWs are grown on top of Ti substrates, a TiO_2 layer is always formed surrounding or supporting the nanowires. Therefore, it was really difficult to isolate the NWs.

DLTS were realized on NWs still on the growing original substrate so it is not possible to discriminate between the signal coming from NWs and the one coming from the supporting TiO_2 layer, even if a comparison TiO2 sample without NWs has been analyzed as well. Some DLTS data show an improvement of the signal intensity when NWs are present, indicating that a certain gain is possible due to an increase of the involved surface.

4.2 - DLTS on TiO_2

The deep level transient spectroscopy (DLTS) [9] is an experimental technique utilizing the depletion region capacitance modification in temperature and time domains as a function of applied voltage, providing information about electronic trap levels. First, we will briefly describe a rectifying junction, needed to create in the semiconductor a depletion region,

that is required in order to perform the DLTS measurement. Then, we will go in to the details of the DLTS technique and its application on TiO_2 samples.

4.2.1 – Rectifying junction for DLTS measurement

A rectifying junction is crucial for most semiconductor devices as well as a tool for electrical characterization of physical properties of semiconductor. In this thesis we will use Schottky contacts on TiO_2 for the electrical characterization by DLTS capacitance technique.

The interruption of the periodic potential of the crystal at the surface
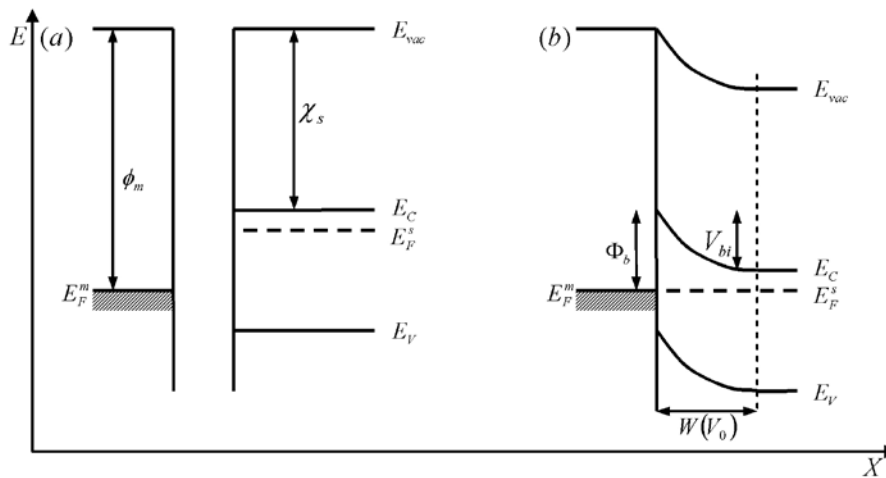
Figure 4.2 – Shottky contact energy band diagram: a metal and a semiconductor before (a) and after (b) a perfect contact.

of the semiconductor modifies the energy potential of the surface. If we consider an ideal junction formation between an n-type semiconductor with an electron affinity (χ_s) and a metal with a work function (ϕ_m), where $\phi_m > \chi_s$ it can be represented as in **Fig. 4.2**.

With a metal contact onto the surface of the semiconductor, electrons from the semiconductor can lower their energy by moving towards the metal. At the equilibrium, the Fermi level of the metal (E_F^m) and of the semiconductor (E_F^s) will coincide. According to the Schottky-Mott model

[10], a band bending of the band edges of the semiconductor occurs, which results in the formation of a region depleted of free carriers, with a width W and a barrier Φ_b. The height of the barrier relative to the Fermi level is given by:

$$\Phi_b = \Phi_b - \chi_s \qquad (4.1)$$

By applying bias to the metal-semiconductor junction, the difference between E_F^m and E_F^s can be manipulated. Under forward bias, E_F^s is raised, thus, the potential across the semiconductor decreases and allows electrons to flow through the junction, which leads to a positive current through the junction at a voltage comparable to the built-in potential V_{bi}. Under reverse bias, E_F^s is lowered, the potential across the semiconductor increases, yielding larger depletion region and larger electric field at the interface which limits the flow of electrons.

The junction and its depletion region can be considered as a parallel plate capacitor, and this concept is of uttermost importance both in semiconductor devices and in our case in probing defects in the band gap by deep level transient spectroscopy. The resulting capacitance, C, becomes:

$$C = \frac{\varepsilon A}{W} \qquad (4.2)$$

where A is the contact area. Fabrication of ideal contacts remains difficult and several factors can strongly modify the properties of the junction, such as the presence of trap states and/or an insulating layer at the interface. These different factors may influence the barrier height and Eq. 4.1 may no longer be appropriate, as it was developed for instance in the model of Bardeen [10] where a thin oxide layer is considered at the interface the metal and the semiconductor. In our samples of TiO_2 NWs grown on Ti foil substrate, the Schottky junction was realized by contacting the top TiO_2 layer with gold.

4.2.2 – DLTS technique

The deep level transient spectroscopy (DLTS) [9] is a powerful technique allowing detecting electrically active defects in the band gap of

semiconductors. DLTS gives quantitative information on: the position in the band gap, the apparent capture cross section and, the concentration of the defect levels. The method is based on the measurement of a capacitance transient of the junction due to the emission process of carrier trapped by defects in the depletion region:

$$C(t) \propto \exp(-e_n t) \tag{4.3}$$

where C is the capacitance and e_n is the electron emission rate of trap defect.

A DLTS cycle is based on a sequence of bias voltage alternatively fixed between a large and a small voltage during a temperature scan. Considering a Schottky contact on an n-type semiconductor with carrier concentration N_D and containing a deep acceptor electron trap of concentration Nt, with Nt << N_D, a DLTS cycle can be described in the three steps (see **Fig. 4.3**):

1. At the start of the DLTS cycle, a large reverse bias is applied, so that the depletion region has a width $W(V_{rb})$ and all the traps in the depletion region above the Fermi level are empty. The width of the region where the defect level is below the Fermi level and therefore filled, is given by $\lambda = \sqrt{\frac{2\varepsilon\,(E_c - E_t)}{q\,N_d}}$, where ε is the permittivity of TiO_2, E_c is the bottom of the conduction band, E_t is the trap energy level, q is the elementary charge and N_d is the carrier concentration. Thus, DLTS measurement probes a region that extends up to $W(V_{rb})$ - λ.

2. A filling pulse is applied to reduce the voltage across the diode. This bias pulse reduces the depletion width to $W(V_0)$ and fills the traps below the Fermi level in this region.

3. After the shutdown of the filling pulse the reverse bias returns to its original value as in step 1. At t_0, the filled traps get again above the Fermi level and the depletion region increase to $W'(V_{rb})$, slightly larger than $W(V_{rb})$ because the charge density in the depletion region is lower than the one in step 1. At $t_0 + t$, the filled traps start to emit the trapped carriers to the conduction band which result in an increase of the charge density in the depletion region and the depletion region width returns to $W(V_{rb})$.
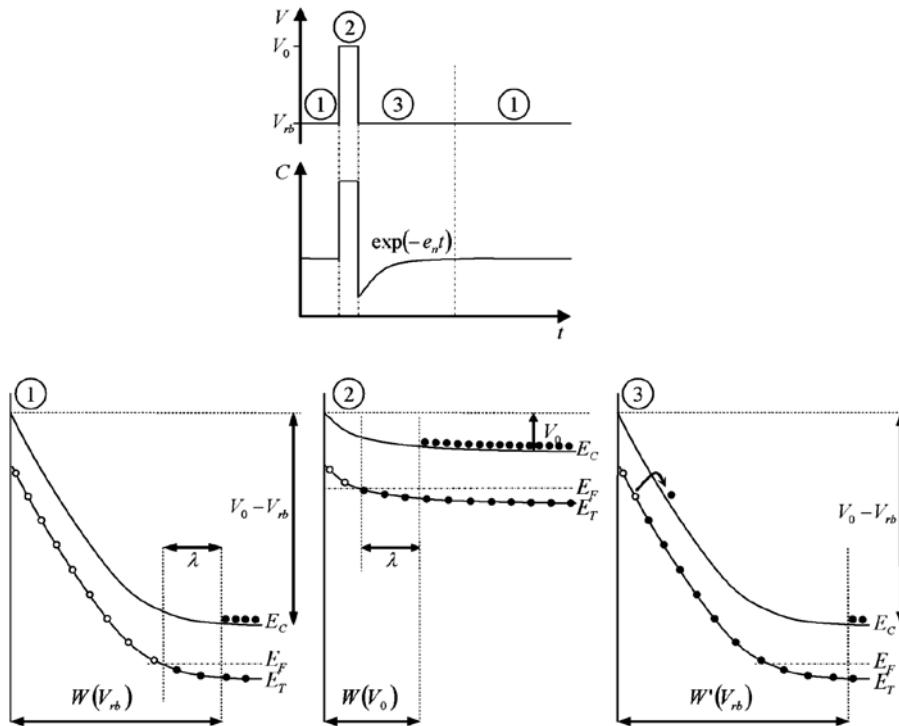
Figure 4.3 - Illustration of the DLTS procedure of a Schottky contact on n-type semiconductor having one defect level with energy position E_t below the conduction band Ec. The DLTS measurement comprises three steps: (1) reverse bias; (2) filling pulse and (3) charge carrier emission.

The emission of carriers is measured by the junction capacitance transient. This transient can be described by an exponential decay, proportional of the emission rate of trapped carriers. The procedure is then repeated (step 1-3) in a temperature scan and a DLTS spectrum is built by measuring the capacitance transient at each temperature.

Fig. 4.4 illustrates the DLTS construction by measuring the capacitance transient at two separate times (t_1 and t_2) for different temperatures. A defect in the depletion region will result in a peak in the DLTS spectrum where the peak maximum position corresponds to the emission rate from the defect level.

Figure 4.4 – DLTS spectrum obtained from the transient capacitance curves at different temperatures (top right inset), considering the capacitance difference measured at two fixed time t_1 and t_2.

If we vary the time difference used in measuring the capacitance transient, called time windows, the peak is shifted in temperature. This will give a set of DLTS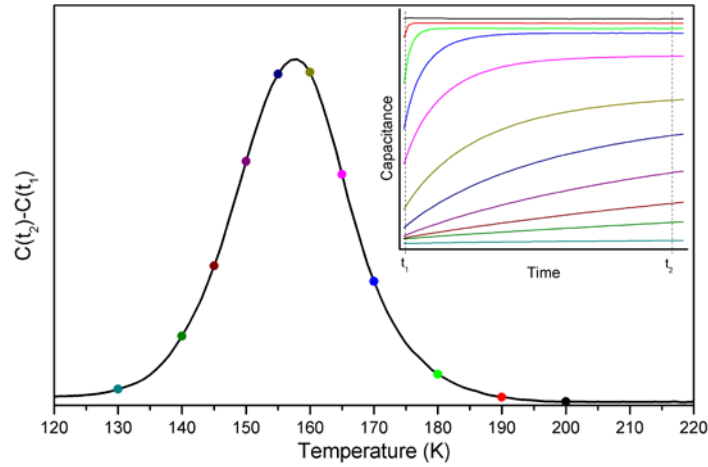 spectra associated with different time windows. The variation of the time window is useful and allows investigation of a wide range of defect levels, e.g. detection of levels close to midgap, while scanning over a limited temperature range. In the present case, a lock-in weighting function is applied to the capacitance transient and each time window corresponds to specific emission rate. Thus, one DLTS spectrum is built for each time window during the same temperature scan when recording the full transient.

A defect level will generate a set of DLTS peaks versus temperature with their corresponding emission rates $(T, e_n(T))$. An Arrhenius plot can be constructed by considering the following expression of the emission rate defined by the Fermi-Dirac distribution:

$$e_n = \sigma_{na}\, \beta\, T^2 e^{-\frac{E_c - E_t}{kT}} \qquad (4.4)$$

where σ_{na} is the electron apparent capture cross section, k is the Boltzmann constant, T is the temperature and $\beta = \sqrt{\frac{3k}{m_n^*}}\, 2 \left(\frac{2\,\pi\, k\, m_n^*}{h^2}\right)^{3/2}$ is a factor

independent of the temperature with m_n^* being the electron effective mass in TiO_2 and h the Plank constant. We can rewrite this equation (4.4) as:

$$\ln\left(\frac{e_n}{T^2}\right) = \ln(\beta\sigma_{na}) - \frac{\Delta H}{kT} \qquad (4.5)$$

The Arrhenius plot obtained from equation (4.5), can give the activation energy enthalpy ΔH and the apparent capture cross section σ_{na} of a defect level form the slope of the line and the intercept at $1/T = 0$, respectively.

Fig. 4.5 shows an example of DLTS spectra for 6 different time windows with one main defect in the 170-230K temperature range. The graph on the right shows the corresponding Arrhenius plot of the observed defect level, giving a position energy of 0.45 eV and an apparent capture cross section of ~10^{-14} cm^2.
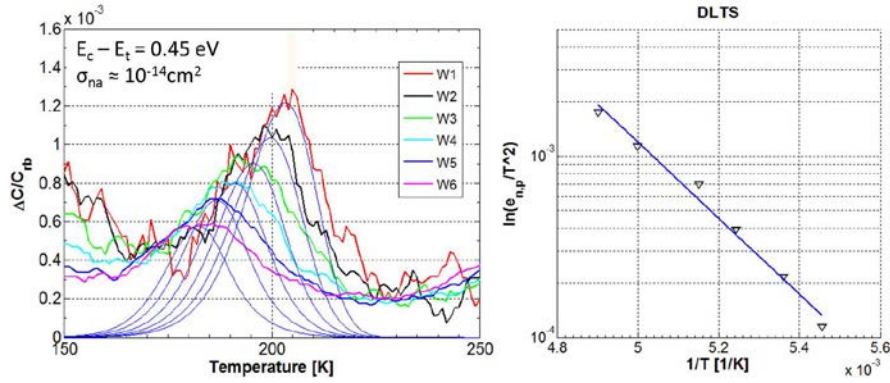
Figure 4.5 – DLTS spectra for six different rate windows (on the left) and the corresponding Arrhenius plot (on the right).

The maximum amplitude of a DLTS peak is proportional of the trap concentration. If we assume a small trap concentration, i.e. $C(V_o) \gg C(V_{rb})$, the change in the depletion region width will be insignificant during the charge carriers emission, so that the emission can be described by a simple exponential decay. Further, if the trap density is uniformly distributed in the material, the relation between the trap concentration and the capacitance transient will be given by:

$$\frac{N_t}{N_d} = 2 \frac{\Delta C}{C_{rb}} \qquad (4.6)$$

Thus, DLTS is a very sensitive technique which allows to detect defects with concentration less than 0.01% of the free carrier concentration. However, due to the assumptions used in DLTS measurement, an appropriate quantification requires that the defect does not exceed ~10% of the doping concentration.

4.2.3 – Experimental

Contacts of 100 nm thick of Au were deposited on the TiO_2 NWs samples and on a single crystal (rutile) bulk TiO_2 sample for comparison. The same contacts were created on a TiO_2 NWs samples, synthetized with the same process, with an additional post-growth treatment in forming gas (FG) at 500°C for 2h (see Chapter 3). The depositions were made by thermal evaporation through a shadow mask. The contacts displayed a Schottky behavior with about one order of magnitude (or more) in current rectification between +1 V in forward and -1 V in reverse bias. The DLTS measurements were carried out in the temperature range of 50 to 325 K using a refined version of the setup described in Ref.Oslo1 [11]. The quiescent reverse bias used was -1 V together with 1 V filling pulse of 50 ms duration.

4.3. – Results and discussion

Fig. 4.6 shows DLTS spectra of two TiO_2 NWs samples, one as-grown and one subjected to post-growth treatment in forming gas (FG) at 500°C for 2h, as already described in Chapter 3. Further, the spectrum of an as-grown TiO_2 sample without NWs is also included for comparison.

Four peaks are clearly resolved occurring at ~55 K, ~110 K, ~188 K and >320 K, respectively, and they are labelled as E_1, E_2, E_3 and E_4. The E_4 peak was not possible to cover fully because of the high conductance of the Schottky contacts at temperatures above 320 K. The corresponding energy positions extracted from six DLTS spectra, recorded simultaneously during

91
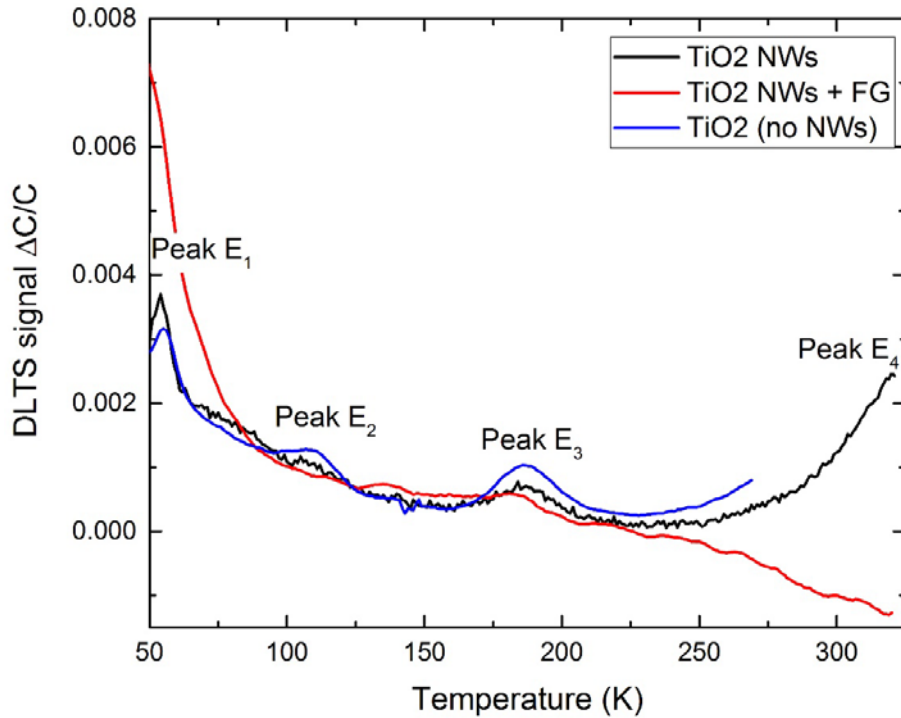
Figure 4.6 - DLTS spectra between 50 and 325 K for three different samples: TiO_2 NWs (as grown), TiO_2 NWs + FG (NWs additionally annealed in forming gas at 500°C), and a TiO_2 sample without NWs. Reverse bias = -1V, filling pulse = +1V, and rate window = $(640 \text{ ms})^{-1}$.

Table 4.1 – Energy level positions and apparent electron capture cross sections of the E_1, E_2, E_3 and E_4 levels.

Level	$E_C - E_T$ [eV]	σ [cm^2]
E_1	0.11	~10^{-14}
E_2	0.30	~10^{-13}
E_3	0.45	~10^{-14}
E_4	>0.6	-

one temperature scan and with rate windows between $(20 \text{ ms})^{-1}$ and $(640 \text{ ms})^{-1}$, are given in **Table 4.1**. The apparent electron capture cross sections of the levels, obtained by extrapolation of the Arrhenius plots of their emission rates, are also included in **Table 4.1**. The spectra of the TiO_2 sample without NWs and the as-grown TiO_2 NWs sample are similar both in shape and amplitude of the four peaks. However, the sample of TiO_2 NWs with the additional annealing in forming gas (TiO_2 NWs + FG), exhibits a considerably higher amplitude of the shallow E_1 peak than the other samples, while the E_2, E_3 and E_4 peaks are substantially weaker. This holds especially for the deep E_4 peak, which has vanished and the spectrum displays negative values above ~275 K presumably caused by hole injection.

The loss of the E_4 level after the FG treatment can be correlated with the 'NW + FG' sample increased photocatalytic activity that will be discussed in Chapter 5. As mentioned above, the position of the E_4 level cannot be determined from the present data but it is estimated to be located at least 0.6 eV below E_C assuming a capture cross section with a typical value of ~10^{-15} cm^2. Hence, E_4 can be anticipated to act as a competing charge carrier recombination center suppressing the catalytic effect of the photon-induced electron-hole pairs.

The identity of the E_1, E_2, E_3 and E_4 levels is not known and previous DLTS data in the literature on deep levels in TiO_2 NWs are scarce (if any). In fact, this holds also for mono-crystalline TiO_2 bulk material where the recent amount of DLTS reports is very limited. An early study by Duckworth et al. [12] showed the presence of a level at ~ E_C - 0.4 eV in N_b - doped rutile samples. This level is possibly identical to the E_3 level in our samples, and Duckworth et al. discussed a tentative assignment to the oxygen vacancy. Regarding the E_4 level, it is tempting to make an association with a defect of dangling bond character being passivated by hydrogen during the FG annealing. However, further work needs to be pursued in order to confirm this speculation.

4.4 – Conclusion

The electrical properties of TiO_2 NWs have been investigated by using deep level transient spectroscopy, which is a powerful technique

allowing to detect electrically active defects in the band gap of semiconductors. Since DLTS is based on the measurement of a capacitance transient of the junction due to the emission process of carrier trapped by defects in the depletion region, a Schottky have been created on the TiO_2 sample surface by depositing a layer of gold on its surface. The contacts displayed a Schottky behavior with about one order of magnitude (or more) in current rectification between +1 V in forward and -1 V in reverse bias. DLTS was carried out in the temperature interval of 50 to 325 K on the following samples: two TiO_2 NWs samples, one as-grown and one subjected to post-growth treatment in forming gas (FG) at 500°C for 2h, and, as reference, on an as-grown TiO_2 sample without NWs. Four peaks were clearly resolved, with energy level below the conduction band at $E_C - E_T$ respectively of: 0.11 eV, 0.30 eV, 0.45eV and >0.6 eV. The latter E_4 peak disappears in the spectrum of the samples tof NWs treated with forming gas. Which aslo exhibits a considerably higher amplitude of the shallow E_1 peak than the other samples, while the E_2, E_3 peaks are substantially weaker.

The loss of the E_4 level after the FG treatment can be correlated with the 'NW + FG' sample increased photocatalytic activity that will be discussed in Chapter 5. Hence, E_4 can be anticipated to act as a competing charge carrier recombination center suppressing the catalytic effect of the photon-induced electron-hole pairs. Moreover, it is tempting to make an association with a defect of dangling bond character being passivated by hydrogen during the FG annealing. The identity of the E_1, E_2, E_3 and E_4 levels is not known and previous DLTS data in the literature on deep levels in TiO_2 NWs are scarce (if any).

References

[1] A. Yamada, B. Sang, and M. Konagai, Appl. Surf. Sci. 112, 216 (1997).

[2] S. Pearton, D. Norton, K. Ip, Y. Heo, and T. Steiner, Prog. Mater. Sci. 50, 293 (2005).

[3] G. Pacchioni, ChemPhysChem, 2003, 4, 1041.

[4] I. Nakamura, N. Negishi, S. Kutsuna, T. Ihara, S. Sugihara and K. Takeuchi, J. Mol. Catal. A: Chem., 2000, 161, 205.

[5] S. Polarz, J. Strunk, V. Ischenko, M. W. E. van den Berg, O. Hinrichsen, M. Muhler and M. Driess, Angew. Chem., Int. Ed., 2006, 45, 2965.

[6] T. Thompson and J. Yates, Jr, Top. Catal., 2005, 35, 197.

[7] Z. Zhang, O. Bondarchuk, J. M. White, B. D. Kay and Z. Dohn´alek, J. Am. Chem. Soc., 2006, 128, 4198.

[8] T. Bredow, G. Pacchioni, Chem. Phys. Lett. 2002, 355, 417.

[9] D.V. Lang J. Appl. Phys., vol. 45, p. 3014, 1974.

[10] S. Lim, S. Kwon, and H. Kim, Thin solid films 516, 1523 (2008).

[11] B.G. Svensson, K.H. Rydén, and B.M.S. Lewerentz, J. Appl. Phys. 66, 1699 (1989).

[12] C.N. Duckworth, A.W. Brinkman and J. Woods, Phys. Stat. Sol, (a) 75, K99 (1983).

Chapter 5

Photocatalytic properties

The last four decades have shown a remarkable increase in scientific interest in photocatalysis as a tool for tackling the world's energy and waste problems. Titanium oxide, as already mentioned in the introduction section of this manuscript, is a powerful semiconductor photocatalyst with relevant advantageous features such as being extremely robust both chemically and photochemically, and inexpensive. A number of different commercial products have arisen from the study on TiO_2, including: self-cleaning glass, concrete, tent/awning materials and tiles, odour-removing paint for indoor applications, NO_x removing paint, concrete and tiles for exterior applications, photo-induced sterile surfaces (ceramics and metals), water and air purification units and defogging mirrors [1]. Such new materials and diverse commercial products require standards by which their effectiveness can be gauged, compared and contrasted.

5.1 – Dye photodegradation testing method

The international standards organisation (ISO) has begun to address the need for the quantification of performance ability of such materials through the publication of a series of standards [2 - 9]. The ISO is the world's leading developer and publisher of international standards, comprising a network of the national standards institutes of 162 countries, with a central co-ordinating secretariat based in Geneva, Switzerland. It is a non-governmental organisation that bridges the public and private sectors and so is able to generate, via a consensus among experts in the field, standards that meet the requirements of both business and society. ISO standards are developed by technical committees, comprising national experts from those sectors that have asked for the standards. Countries

96

sometimes choose to refer to the ISO standards even in regulative legislations.

Regarding the evaluation of the photocatalytic activity of the materials, the ISO standard recommend the use of the Methylene blue (MB) dye as described in the document "ISO 10678: 2010 - Determination of photocatalytic activity of surfaces in an aqueous medium by degradation of methylene blue"[5].

MB is a highly popular test pollutant in semiconductor photocatalysis used in the assessment of such key features as: new photocatalytic materials, photoreactors and light sources. The molecular structure of MB is represented in **fig.5.1.**
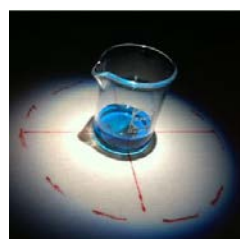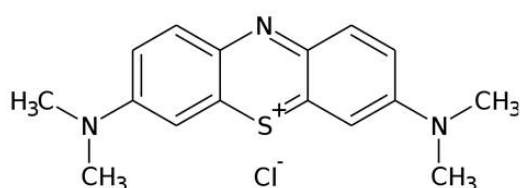
Figure 5.1 - Molecular structure of the Methylene Blue (MB) dye and a MB aqueous solution in a beaker containing a TiO_2 sample.

Its popularity lies in its simplicity, since all that is required for an assessment is the measurement of the rate of photocatalytic bleaching of MB in aqueous solution via UV/vis spectrophotometery. The high molar absorptivity of MB ensures a striking and easily measured colour change, from blue to colourless, when the dye is photo-bleached by the semiconductor photocatalyst under study. MB is still used, although no longer on a large scale, as a textile, leather and paper dye and so is a reasonable choice as a test pollutant dye for the photocatalytic remediation of water.

It has been demonstrated [10] that titania is able to mediate the complete photo-mineralisation of MB ($C_{16}H_{18}N_3SCl$) as it follows:

$$C_{16}H_{18}N_3SCl + 25.5O_2 \xrightarrow[h\nu>3eV]{TiO_2} HCl + H_2SO_4 + 3HNO_3 + 16CO_2 + 6H_2O$$
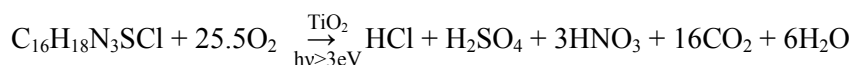
The schematic of the overall reaction, for the photocatalytic mineralization of a generic organic pollutant on the surface of titania is illustrated in more details in **fig. 5.2**:

Figure 5.2 – Schematic of the overall reaction, for the photocatalytic mineralisation of an organic pollutant on the surface of a titania photocatalyst sample. (1) Ultra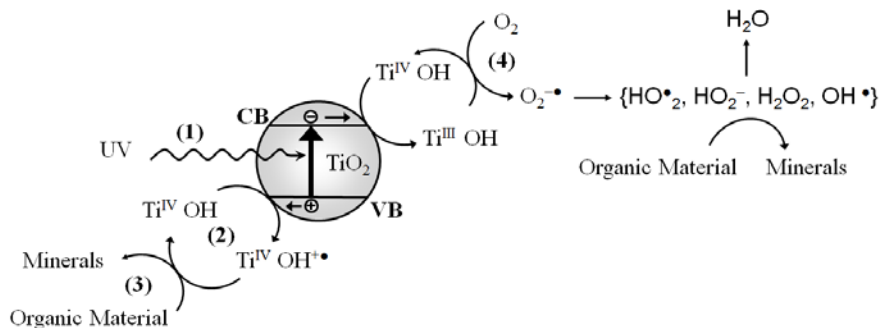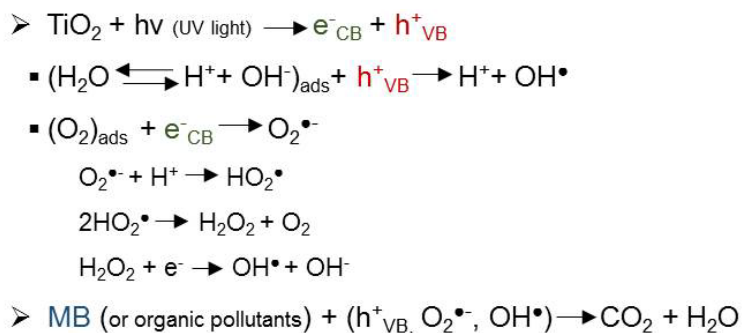-band gap light generates electron-hole pairs. (2) Photogenerated holes migrate to the surface which then react with surface hydroxyl groups to generate hydroxyl radicals. (3) Organic pollutants are oxidised to their mineral form via the hydroxyl radicals. (4) Photogenerated electrons can react with adsorbed oxygen to generate superoxide and subsequently other reactive species which can also oxidise organic pollutants.

(1) the electron-hole pair photogenerated by the ultra-band gap light respectively in the conduction band (CB) and valence band (VB), can migrate to the surface of titania; (2) holes (h^+_{VB}) react with the surface adsorbed hydroxyl groups (OH⁻) generating reactive hydroxyl radicals (OH•) that (3) can oxidize the organic pollutants to their mineral form; (4) electrons (e^-_{CB}) can react with the adsorbed oxygen (O_2) to generate superoxide radicals (O_2•⁻), that can also oxydize organic material. Moreover, O_2•⁻ can also induce various reactions producing other reactive species such as HO_2•, H_2O_2, OH•, able as well to oxidize organic pollutants:

> $TiO_2 + h\nu$ (UV light) $\longrightarrow e^-_{CB} + h^+_{VB}$

    ▪ $(H_2O \rightleftharpoons H^+ + OH^-)_{ads} + h^+_{VB} \longrightarrow H^+ + OH$•

    ▪ $(O_2)_{ads} + e^-_{CB} \longrightarrow O_2$•⁻

        O_2•⁻ $+ H^+ \longrightarrow HO_2$•

        $2HO_2$• $\longrightarrow H_2O_2 + O_2$

        $H_2O_2 + e^- \longrightarrow OH$• $+ OH^-$

> MB (or organic pollutants) $+ (h^+_{VB,} O_2$•⁻, OH•$) \longrightarrow CO_2 + H_2O$

The main and very strong advantages of this ISO standard are its simplicity and ease of use. On the other hand, the standard is not completely reliable for materials with photonic efficiencies > 0.1% [11] and it also results not entirely appropriate for assessing activity in the visible light (i.e. using visible light source instead of the recommended UV light source), since dye-sensitised photobleaching, could make a significant (non-photocatalytic) contribution to the observed photobleaching of the dye. In fact, MB absorbtion in the visible range is not negligible and it can give rise to dye photosensitised processes where the electronically excited state of the dye injects an electron into the conduction band of the photocatalytic material producing an oxidised dye radical which is unstable and able to decompose subsequently to bleached products. However, the standard is appropriate for assessing the photocatalytic activity of photocatalyst using UVA light [11], like we did in this thesis.

5.2 - Experimental

The study of the photo-catalytic properties of the synthetized TiO_2 samples was carried out following the international standards ISO 10678:2010 [5]. We monitored the degradation of the methilene blue (MB) dye, in a water solution under UV light.

For each measurement the sample was first preconditioned: it was exposed to UV light using a lamp in the wavelength range of 350-400 nm (TL 8W BLB 1FM Philips lamp), with a stable irradiance of 1.1 mW/cm^2 at the sample surface. This was done in order to clean the sample surface from any organic contaminant, which could affect the measurements. Then, the sample was placed in a cuvette filled with the MB water solution (2 ml at $\sim 10^{-5}$ M) and kept in dark. In this way the dye degradation was monitored in dark for about 12 h until saturation (variation of the MB concentration < 1% hour $^{-1}$); after this step, the decrease of MB concentration due to the physical absorption of the dye by the sample surface can be considered negligible. Afterwards, the cuvette with the MB and the sample was covered with a quartz glass (having a minimal absorbance within the spectral emission region of the UV light source), to prevent the solution evaporation, and irradiated with the same UV light employed for the preconditioning step.

The experiment was carried out at room temperature condition and in air. The experiment set up is illustrated in the schematic diagram of **fig. 5.3**.
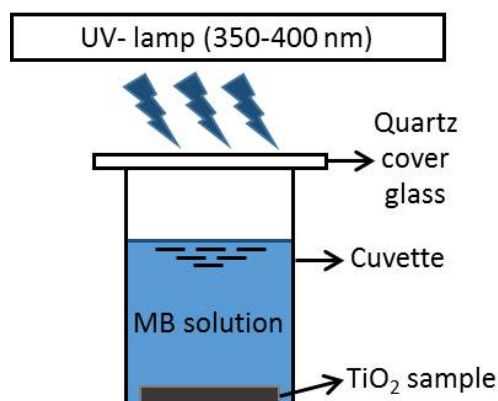

Figure 5.3 – Schematic diagram of the experimental set up for the measurement of the photocatalytic activity of a TiO_2 sample in MB aqueous solution, following the standard ISO 10678: 2010 [5]

Meanwhile, we monitored the MB degradation by measuring the absorbance of the solution, which is proportional to the MB concentration according to the Lambert-Beer law [12]:

$$A = \varepsilon \; x \; l \; x \; C \quad \text{(Lambert-Beer law)}$$

where A is the absorbance of the solution, ε is the extinction molar coefficient, l is the height of the solution, and C is the concentration of the MB. During 3 hours we measured every 20 min the absorbance at 664 nm, where the main absorbance peak of MB occurs, by means of a spectrophotometer (Lambda45, Perking-Elmer) in the wavelength range of 500-750 nm. **Fig. 5.4** reports on the left, the absorbance spectrum of the MB molecule (blue line), together with the one of the employed UV lamp (red line). The spectra on the right, represents a typical absorbance spectra behaviour of the MB solution in contact with a TiO_2 sample, varying the time of irradiation under UV light. For clarity, it does not show all the curves measured every 20 min. With this procedure, we also ensure a homogenous concentration of the solution by mixing it every 20 minutes (as suggested by the ISO protocol) while transferring it in another cuvette for the absorbance measurements in the spectrophotometer. The collected values, normalized to

100

the macroscopic area of the sample, were used to calculate the pseudo-first order photocatalytic rate constant (or degradation rate constant) of our sample, following the degradation kinetics law:

$$C = C_0 e^{-kt} \quad \text{(first order kinetic law of MB degradation)}$$

where C is the concentration of the MB solution at the time t, C_o is its initial concentration at t = 0, and k is the degradation rate constant. The kinetic law is of the first order as the reaction rate results proportional to the MB concentration (dC/dt = - kC). In addition, when in a reaction the concentration of one of reactant remains constant (because it is a catalyst or it is in great excess with respect to the other reactants), it can be included in the rate constant, and we call it pseudo–first-order rate equation.
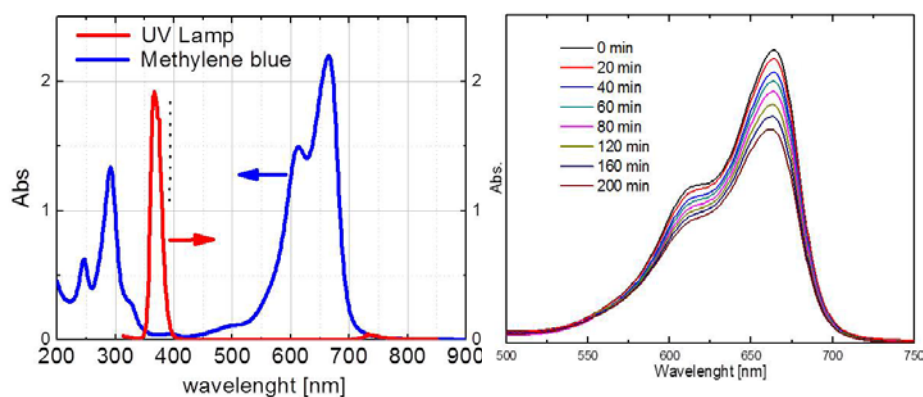
Figure 5.4 - On the left: absorbance spectra of the Methylene Blue molecule (blue line) and the UV lamp employed for the photocatalytic measurement (red line); on the right: typical absorbance spectra of the MB solution in contact with a TiO_2 sample, for different irradiation time under UV light.

The sizes of the analyzed samples were usually about 1 cm^2, referred as macroscopic area. We also performed all the mentioned processes in parallel with a cuvette containing only the MB solution, in order to have a control reference measurement.

In addition, measurements of the samples reflectivity were carried out by means of the spectrophotometer Lambda 40 Perking-Elmer equipped with an integrating sphere, in order to evaluate the share of photons that are not reflected and that are actually involved in the photocatalytic process.

5.3 – Results and discussion

The analysis of the experimental results and the related comments will be illustrated considering first the study on the TiO_2 NWs grown on Ti bulk foil, then the sample of TiO_2 NWs grown on Ti thin film substrate and on the iron doped film. The samples were already treated in Chapter 2 and Chapter from the point of view of the synthesis and morphological and structural characterization. Antibacterial activity of nanospike and nanowires TiO_2 substrates will be studied in the last paragraph.

5.3.1 - Photocatalytic activity of TiO_2 NWs on Ti foil

NWs TiO_2 synthetized on bulk Ti foil have been already studied in paragraph 2.1 morpohlogically and structurally. **Fig. 5.5** reports the analysis of photo-catalytic activity of these type of samples. The plot shows the values of the logarithm of the absorbance at a wavelength of 664 nm (proportional to C) normalized to the initial value at t = 0 s (proportional to C_0); the values are also normalized to the macroscopic area of each sample. The lines represents the fits with linear regression.

The reported data refers to the following samples: MB reference solution without any TiO_2 sample (blue downward triangles); TiO_2 reference foil without NWs (green upward triangles); TiO_2 foil with NWs grown at 800°C for 4h with a mixed flow of Ar at 10 lpm and O_2 at 7,5 lpm, namely the optimal growth conditions discussed in Chapter 2 (black squares); TiO_2 foil with the same NWs as the latter mentioned sample, with an additional annealing in forming gas at 500°C for 2h (red circles), as discussed in Chapter 3. The TiO_2 reference sample without NWs was processed with the same annealing treatment of the NWs sample but without gold previously sputtered on its surface. The negative slope of the lines (not considering the MB reference solution), confirm a decrease with time of the absorbance and therefore of the MB concentration; this indicates that the TiO_2 photocatalysis reaction, i.e. the degradation of the dye, tooks place. This slope represents the pseudo-first order photocatalytic rate constant (or degradation rate constant) of the photo-catalysis reaction per unit of area.
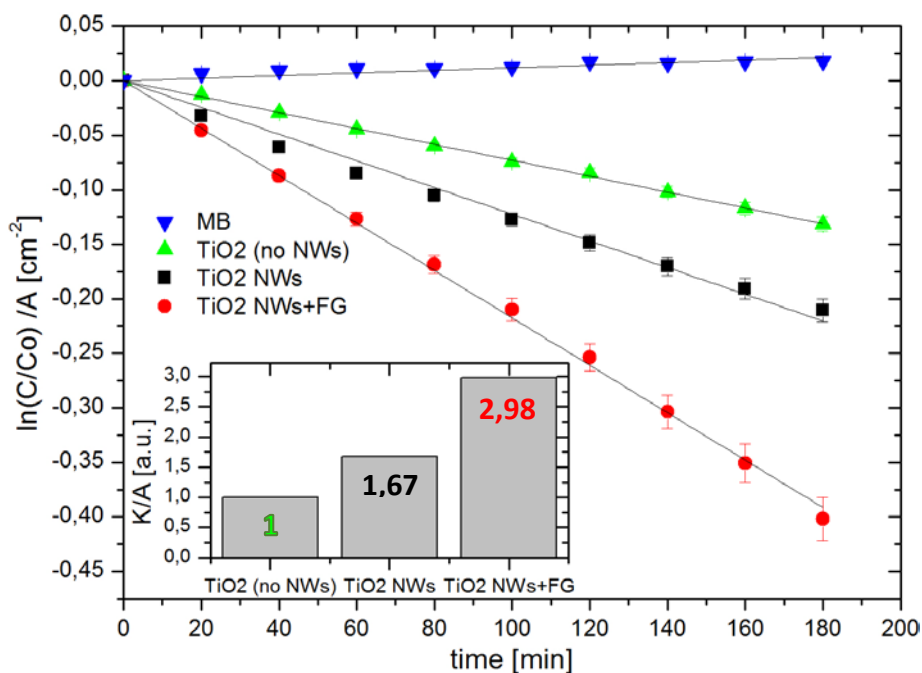
Figure 5.5 - Photocatalytic activity of various samples: MB reference solution without any TiO_2 sample (blue downward triangles); TiO_2 reference foil without NWs (green upward triangles); TiO_2 foil with NWs (black squares); TiO_2 foil with NWs and additional annealing in forming gas (FG, red circles). Inset: degradation rate per unit area (K/A) of the samples normalised to the K/A obtained from the TiO_2 reference foil without NWs.

The inset of **fig.5.5** shows more clearly the degradation rate constant (k) of the samples per unit area (A) normalised to the degradation rate constant of the TiO_2 reference sample without NWs. The histogram indicates that the sample with TiO_2 NWs shows an improvement in the degradation rate constant of almost 70% compared to the one of the reference TiO_2 foil without NWs. Moreover, an additional thermal treatment in forming gas results in a further improvement of the degradation rate, which is almost 3 times higher compared to the one of the reference TiO_2 foil and almost doubled versus the one of the TiO_2 NWs sample.

The photonic efficiency of the MB degradation (ζ_{MB}) of the active sample, was calculated as indicated in the international standards ISO 10678:2010 [5], that is:

$$\zeta_{MB} = \frac{P_{MB}}{E_P} \times 100 \quad \text{(photonic efficiency of the MB degradation)}$$

where P_{MB} is the photoactivity, corresponding to the average degradation rate calculated during the UV irradiation, expressed in (mol of MB molecules)/(m^{2}h); E_P is the photon UV-radiation intensity irradiated by the lamp used during the MB experiment, indicated in (mol of photons)/(m^{2}h). ζ_{MB} refers to the efficiency of the photons in the process of MB degradation, considering the total light incident on the sample. The resulting efficiencies for the three samples are reported in **Table 5.1**. The NWs sample showed an increased photon efficiency of 25% compared to the TiO$_2$ sample without NWs. Moreover, the NWs annealed in forming gas, revealed even higher photon efficiency, doubled with respect to the ζ_{MB} of the reference TiO$_2$ foil.

Table 5.1 – Photocatalytic rate constant and efficiency parameters of the studied samples.

	TiO$_2$ (no NWs)	TiO$_2$ NWs	TiO$_2$ NWs+FG
K/A [a.u.]	1	1.67	2.98
ζ_{MB} [%]	0.0095 ± 0.0009	0.012 ± 0.001	0.019 ± 0.001
Φ_{MB} [%]	0.011 ± 0.001	0.013 ± 0.001	0.021 ± 0.001

Another significant parameter to take into account is represented by the quantum efficiency of the MB degradation (Φ_{MB}), which considers only the effect of the "absorbed" photons (not reflected) [15]. For this purpose, the reflectance of the three studied samples was measured and it is reported in **fig.5.6** together with the spectra of the UV lamp employed for the MB photocatalytic degradation measurements. NWs samples exhibited the same reflectance (black and red lines) at the same light wavelengths range of the employed UV source (green line), thus the increased photocatalytic efficiency of the NWs sample annealed in forming gas (FG) should be related to intrinsic factors, such as extended carrier life-times, and not due to antireflective effects due to their morphology.

The quantum efficiencies were then calculated by using these values of reflectance in the spectra of the UV lamp used in our MB experiment
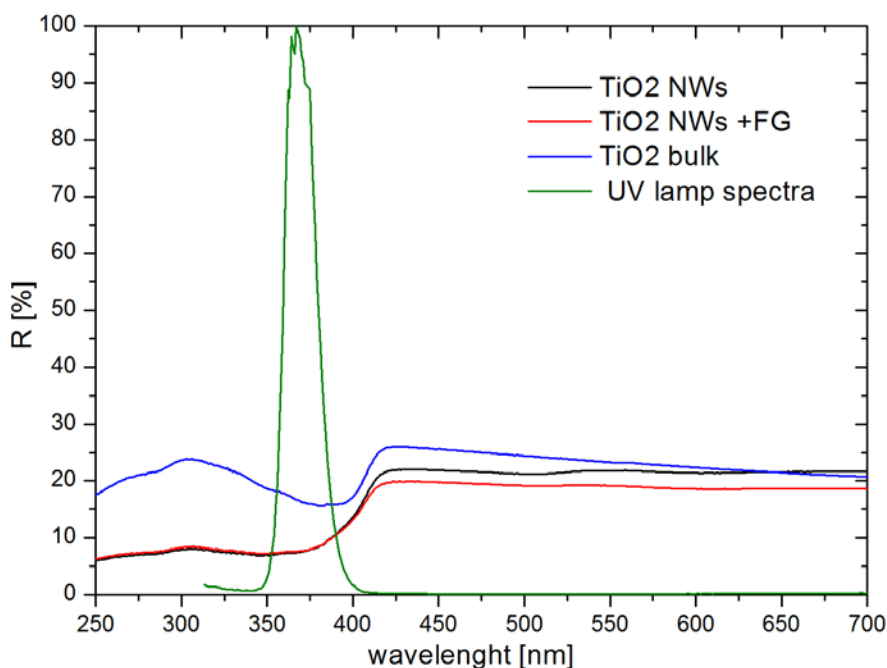
Figure 5.6 - Reflectance of the three studied samples: TiO_2 NWs (black line); TiO_2 NWs additionally treated with a forming gas (FG) annealing (red line); TiO_2 reference bulk substrate without NWs (blue line). The spectra of the UV lamp employed for the photocatalytic measurement, is also reported (green line).

(**table 5.1**). The obtained Φ_{MB} values showed again an improvement with the presence of the NWs of almost 20% compared to the reference TiO_2 foil; this increase went up to 90% in the case of NWs treated with the forming gas.

These increases in efficiencies further indicate the positive effect of the presence of the nanowires structures and of the additional forming gas treatment, in the photocatalytic properties of the TiO_2 material. It has already been reported in literature [13, 14] that annealing treatments of TiO_2 with hydrogen (present in the forming gas), can increase the carrier density and so the photocatalytic activities.

Moreover, this increase in the photocatalytic activity after the forming gas annealing correlates also with the results obtained by deep level transient spectroscopy discussed in Chapter 4, that showed a disappearance of a deep level recombination centre that could have suppressed the catalytic effect of the photon-induced electron-hole pairs. It may be a defect of

105

dangling bond character being passivated by hydrogen during the forming gas annealing.

5.3.2 - Photocatalytic activity of TiO_2 NWs on Ti Thin film

The analysis of photo-catalytic activity of the synthetized NWs grown on the Ti thin film substrate (morphology reported in section 2.2.1) is illustrated in **Fig. 5.7**. The dots in the plots represent the different absorbance measurements carried out every 20 min for a total time of 3 h, during the UV irradiation of the sample immersed in the MB solution. The negative slope of the curves confirm a decrease with time of the absorbance and therefore of the MB concentration; this indicates that the TiO_2 photo-catalysis reaction,
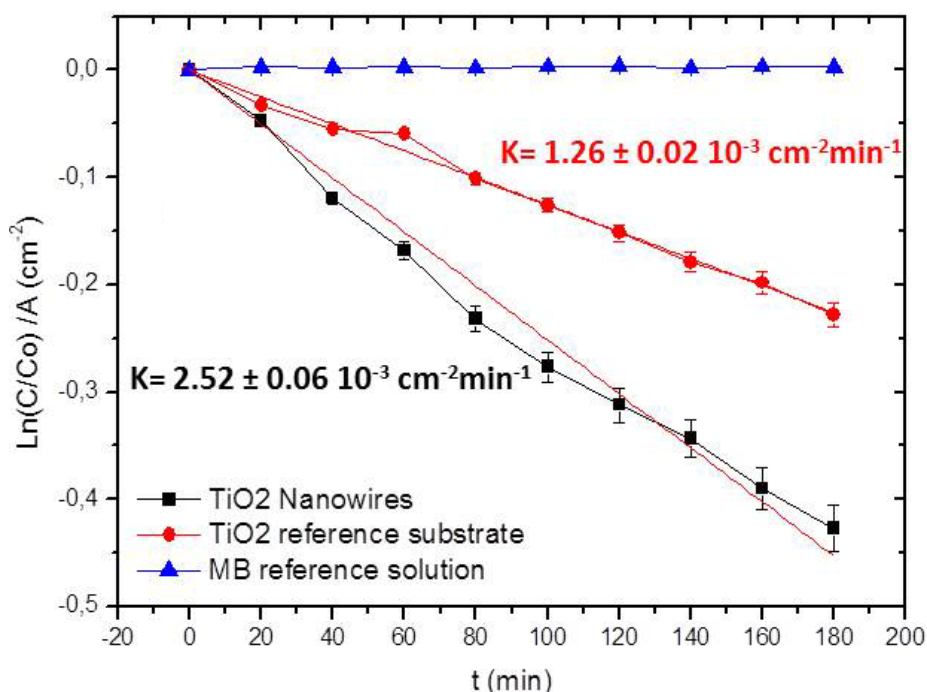

Figure 5.7 – Logarithm of the MB concentration C normalized to the initial concentration Co and to the sample macroscopic area for the TiO_2 NWs grown on the Ti film substrate (squares), the reference TiO_2 film annealed substrate (circles) and the reference MB solution (triangles). The fits give the photo-catalytic rate constant k per unit area.
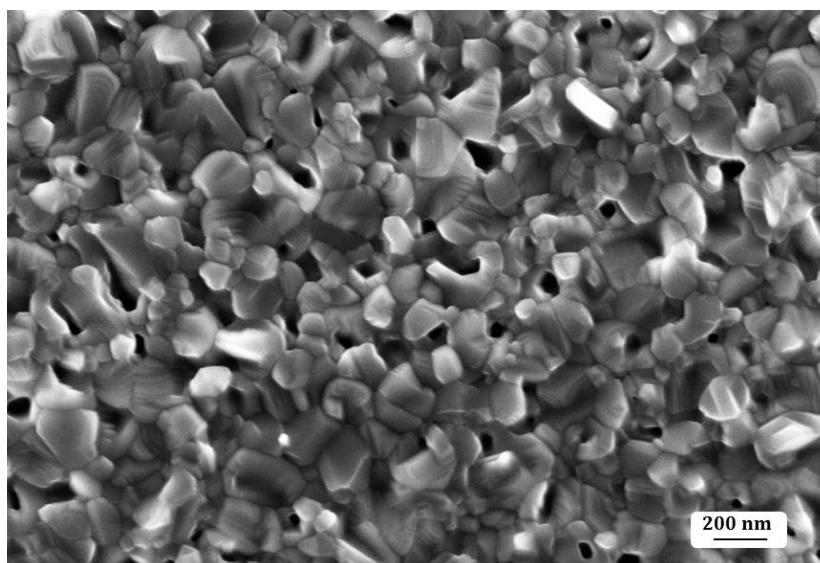
Figure 5.8 - SEM plan-view image of the reference TiO_2 substrate, consisting of the Ti sputtered film annealed at the same conditions (700°C, 4h, gas flow of Ar 1.5 lpm and O_2 0.1 lpm) used for the NWs growth.

i.e. the degradation of the dye, tooks place. The plot shows the calculation of the degradation rate, which was done reporting the logarithm of the absorbance at a wavelength of 664 nm normalized to the initial value at t=0 s and then divided by the macroscopic area of each sample. The slope represents the photocatalytic rate constant of the reaction, per unit of area. For the NWs sample it resulted to be $(2.52 \pm 0.06) \cdot 10^{-3}$ cm^{-2} min^{-1} (black squares in **Fig. 5.7**). In order to evaluate the contribution of the NWs in the process, the calculation of the photocatalytic rate constant was carried out in parallel on a reference substrate created using the Ti thin film treated with the same annealing process (red circles in **Fig. 5.7**). SEM imaging in **Fig. 5.8** indicated that this reference substrate, treated with the same annealing conditions of NWs growth (700°C, 4h, gas flow of Ar 1.5 lpm and O2 0.1 lpm) has the TiO_2 granular structure of the same size of the sample with nanowires; the whole film thickness was also the same, about 325 nm. The degradation rate constant for this sample without NWs resulted to be $(1.26 \pm 0.02) \cdot 10^{-3}$ cm^{-2} min^{-1}, corresponding to half of the value obtained with the presence of NWs.

107

The photonic efficiency (in %) of the MB degradation for the two samples was estimated following the ISO 10678:2010 standard [5], obtaining $(1.3 \pm 0.5) \cdot 10^{-2}$ for the reference substrate without NWs and, $(2.1 \pm 0.6) \cdot 10^{-2}$ for the sample with NWs, corresponding to an increase of about 60%. These results confirm an improvement of the photocatalytic properties due to the presence of the TiO_2 NWs on the sample.

5.3.3 - Photocatalytic activity of TiO_2 NWs on nanospikes

As discussed in Chapter 2 (Paragraph 2.2.3), TiO_2 NWs were also synthetized by thermal seed assisted growth on a substrate of nanospikes with height up to 400 nm. The photocatalytic activity of this sample was studied together with a reference sample represented only by the nanospikes substrate, treated with the same annealing process but without the gold catalyser layer, so without NWs grown on top of the nanospikes.

Fig. 5.9 report the results of the analysis of the photocatalytic activity of these two samples together with the reference value measured from a cuvette containing only the MB solution. The experiment was carried out for 3h and the data, collected every 20 min for each sample, are represented by the points in the plot. In particular, the plot shows for each sample the logarithm of the MB concentration divided by the initial concentration, and afterwards normalized by the area of each sample, versus the time of exposure to the UV radiation. The negative slope confirms the effectiveness of the dye degradation with time.

The photocatalytic rate constant, per unit area, for the TiO_2 NWs grown on the nanospikes substrate, resulted to be $(3.09 \pm 0.07) \cdot 10^{-3}$ cm^{-2} min^{-1} ; while for the reference nanospikes substrate (whithout NWs) it was calculated as $(2.28 \pm 0.03) \cdot 10^{-3}$ cm^{-2} min^{-1}. Therefore, the contribution of the nanowires in the surface of the nanospike substrate, had as effect an improvement of the photocatalytic activity of about 36% compared to the same substrate without NWs.

The calculation of the photonic efficiency of the MB degradation (ζ_{MB}), following the international standards ISO 10678:2010 [5], provided the following values (in %): $(2.7 \pm 0.6) \cdot 10^{-2}$ for the sample of NWs on top of the nanospikes substrate; and $(1.9 \pm 0.3) \cdot 10^{-2}$ for the bare nanospikes
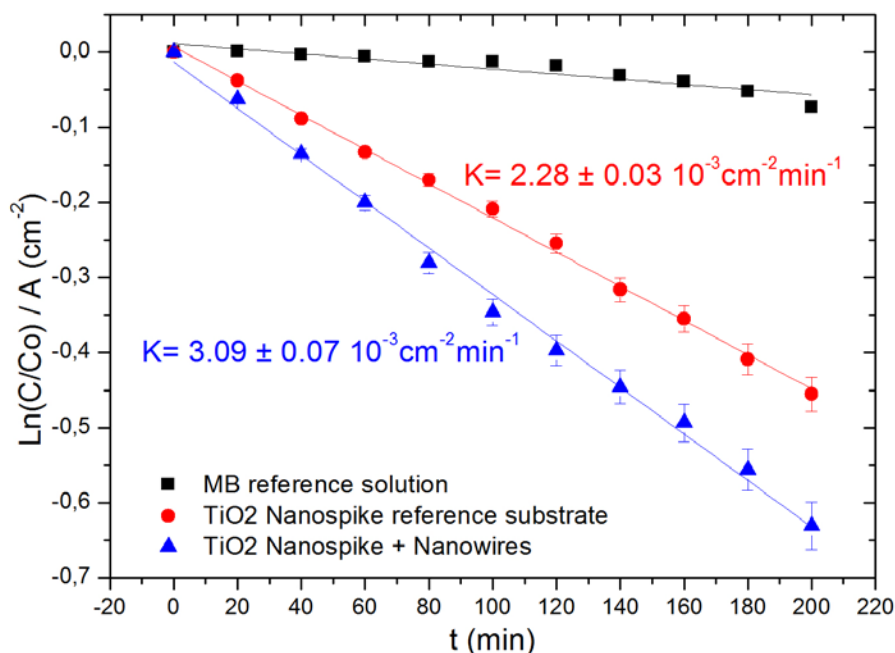
Figure 5.9 – Photocatalytic activity of: TiO_2 NWs grown on a nanospikes substrate ((blue trianlges); the reference substrate of nanospikes without NWs (red dots); and the reference MB solution.

substrate. Therefore, the presence of the NWs resulted in enhancement of about 40% in the photonic efficiency.

5.3.4 Photocatalytic activity of Fe^+ implanted TiO_2 thin film

The photocatalytic activity of the iron implanted films was also evaluated by the degradation of the methylene blue both under UV (350–400 nm wavelength range) and VIS (420–470 nm wavelength range) irradiation. The results are reported in **Fig. 5.10** (for the UV data) and **Fig. 5.11** (for the VIS data). They illustrate the photocatalytic rate constant of the MB, normalized to the value obtained for the MB decomposition in the absence of any catalyst materials, for the different samples, both under UV and VIS light irradiation. On the abscissa axis, MB indicates the MB decomposition in the absence of catalyst that is always 1 due to the normalization done (i.e., k/k_{MB}); TiO_2 refers to the MB decomposition in the presence of a pure TiO_2

film; as-implanted indicates the MB decomposition in the presence of Fe^+ implanted TiO_2 films; etc.

Under UV irradiation (**Fig. 5.10**), the better response in terms of photodegradation of MB was displayed by the pure TiO_2 films. The photocatalytic efficiency decreased considerably in the case of iron implanted TiO_2, suggesting that the defects induced by the ion implantation work as electron-hole recombination centers, which is different from what was reported by Anpo et al. [16]. Under VIS irradiation, the situation
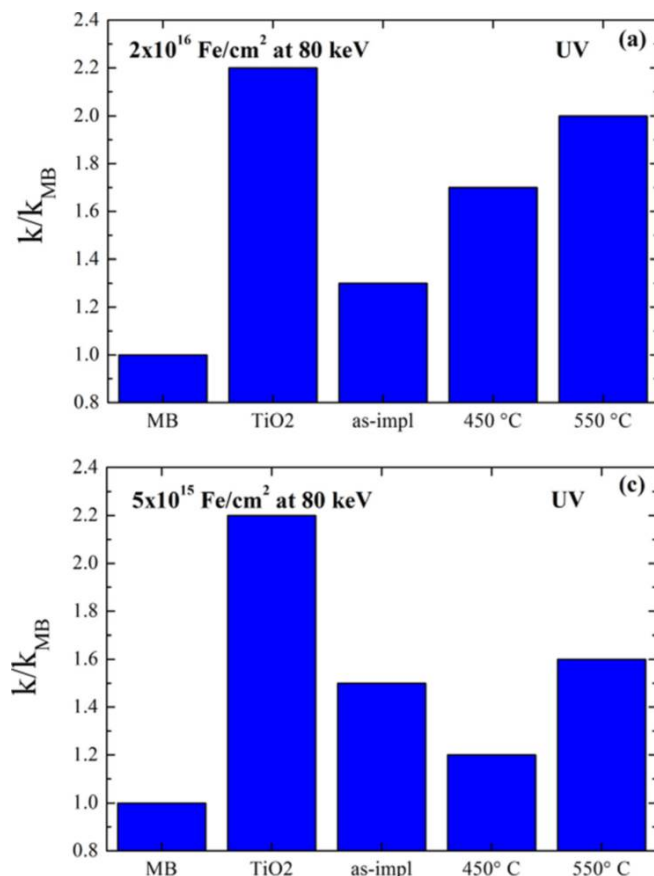

Figure 5.10 - Photocatalytic rate of MB, normalized to the value obtained for MB in the absence of the photocatalyst, for different Fe^+ implanted films: 2×10^{16} cm^{-2} (a), 5×10^{15} cm^{-2} (c), under UV light irradiation [17].

reversed. In particular, the samples implanted with the high fluence (F**ig. 5.11b**) show no photocatalytic activity just after the implantation process, but an improvement of 20% and 30% was obtained with the thermal treatments at 450 and 550 °C. These results can be interpreted as follows: the ion-implantation causes a remarkable optical absorption in the VIS range due to the introduction of defects responsible for the formation of energy levels inside the band-gap of the implanted titania. As a consequence, a significant amount of electron-hole couples are formed due to the VIS light irradiation. On the other hand, these energy levels can behave as active sites for the recombination of electron-hole photo-generated couples, decreasing in this way the photocatalytic performance of the material.

Thus, our results suggest that ion implantation with a fluence of 2×10^{16} cm^{-2} is, on one hand, responsible for the reactivity of the material to the VIS light (as showed in the absorbance plot in Chapter 3), but, on the other hand, the defects induced by the ion implantation cause strong electron-hole recombination, compromising the photocatalytic activity of the as-implanted films. However, with the reduction of defects by annealing (see Chapetr 3), an increased photocatalytic activity is observed with VIS light.

The films implanted with the low fluence (**Fig. 5.11d**) show a more dramatic increase in photocatalytic activity under the VIS irradiation, prior to annealing: an increase of 80% with respect to the pure TiO_2 film. After annealing at 450 °C, such an increase is 50%, while it disappears after annealing at 550 °C. Following the same reasoning as reported above, the results for the low fluence suggest that the ion implantation introduces defects into the material, which are responsible for VIS light absorption (see the absorbance plot in Chapter 3), but now the amount of defects is not as high as to negatively affect the efficiency of the mineralization process (through electron-hole recombination). With increasing of the annealing temperature, the efficiency decreases because of the low level of defects: at 550 °C, the defect level is low (as showed from the XRD plot in Chapter 3) and no energy levels are present inside the band-gap. As a consequence, the implanted and annealed films cannot give anymore a photocatalytic response in the VIS (see the absorbance plot in Chapter 3).
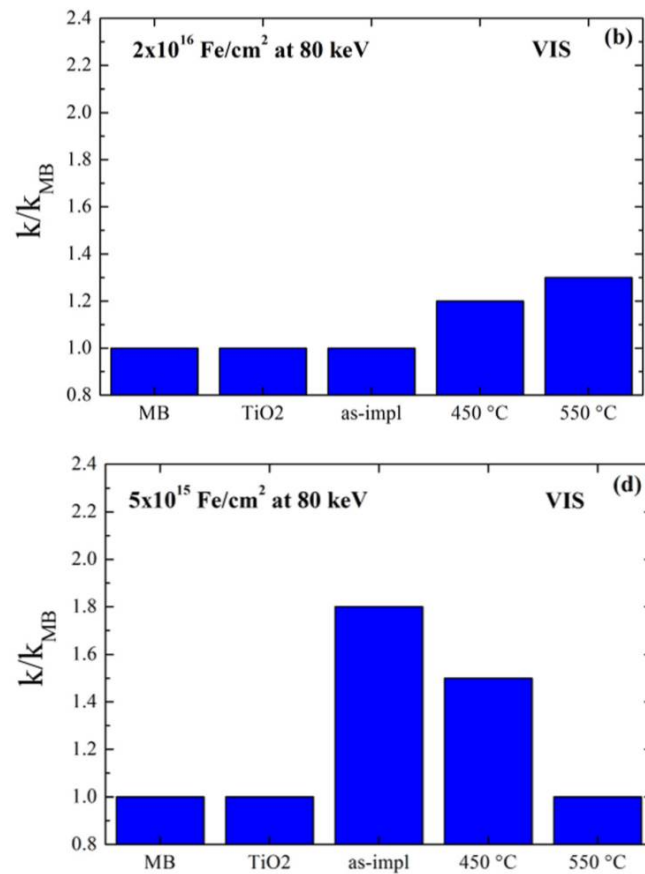
Figure 5.11 – Photocatalytic rate of MB, normalized to the value obtained for MB in the absence of the photocatalyst, for different Fe^+ implanted films: 2×10^{16} cm^{-2} (b), 5×10^{15} cm^{-2} (d), under VIS light irradiation [17].

5.3.4 – Antibacterial activity of TiO$_2$ NWs

The antibacterial activity was tested on *Escherichia coli*, a well-known Gram-negative bacterium representative of coliforms and considered to be an indicator of fecal contamination in drinking water. Hence, E. coli

112

has been chosen as a model organism to evaluate the bactericidal activity of the samples by the colony forming unit (CFU) method.

The antibacterial test consists on measuring the survival rate of *E. coli* after exposure to UV light activated samples. Our test was performed on *E. coli* ATCC 25922 strain. A single colony was inoculated in 50 ml of Luria-Bertani (LB) broth and grown overnight at 37 °C by constant agitation at 180 rpm under aerobic conditions. The following day, the bacterial growth was measured by optical density at 600 nm. Bacteria were diluted up to 10^5 CFU/ml in phosphate buffer saline (PBS) and 100 μl were added onto the titania samples. In order to test antibacterial activity, photocatalysis was induced by exposition to the same UV light previously used for the MB photo-degradation. Untreated bacteria and bacteria exposed to UV only (not in contact with the TiO_2 samples) were treated in parallel as control samples. Aliquots were collected at 15 and 60 min respectively, conveniently diluted by serial dilutions 1:10 and plated in LB Agar Petri dishes. Plates were incubated overnight at 37 °C. CFU were counted the following day.

Results of the antibacterial activity test on the TiO_2 sample of nanospike and NWs thermally grown on top of the nanospike are presented
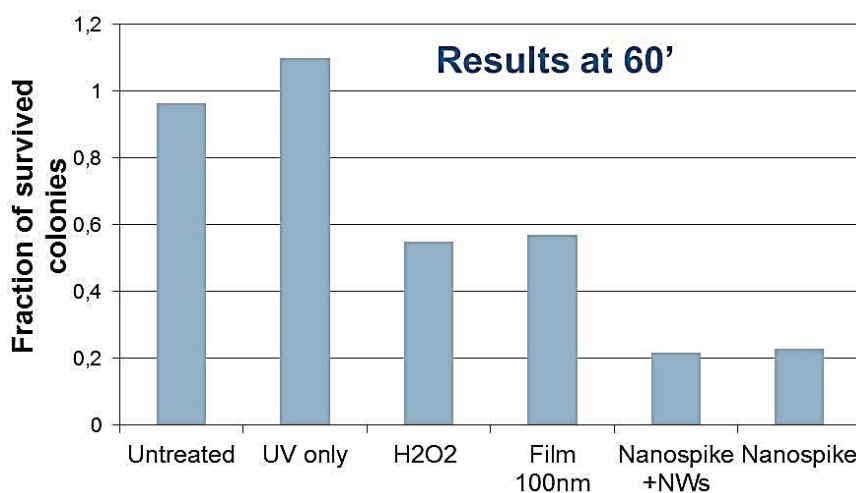

Figure 5.12 –Fraction of survived colonies of *E.Coli* in contact with the TiO_2 studied samples (i.e. TiO_2 nanospikes and TiO_2 nanospikes with NWs grown on top) after 1h of UV light exposure.

in **Fig. 5.12**. After one hour of exposure to UV, the survival percentage of *E. coli* in contact with the nanospikes and the nanospikes with nanowires samples is reduced to 22% and 23%, respectively. Hence, the nanospikes and nanospikes with nanowires show similar antibacterial activity, which is higher if compared to the activity showed by a 100 nm thick TiO_2 film substrate sample (~ 57% colonies reduction) or to the one exhibited by the typical bactericide as H_2O_2 (~ 56% colonies reduction). *E. coli* exposure to UV light only showed a fraction of survived colonies of 1.1, which – considering an experimental error of ca. 0.15 – corresponds to a trivial damage due to the UV. A similar comment can be done for the result of untreated bacteria (0.96 fraction of survived colonies). Therefore, the major reason for the antibacterial effect is due to the presence of TiO_2 nanostructures.

5.4 – Conclusions

In this Chapter we have studied the photocatalytic activity of different TiO_2 samples on various substrates synthetized by the thermal seed assisted method (as illustrated in Chapter 1) and on the doped TiO_2 samples described in Chapter 3. The photocatalytic performance of the samples were assessed applying the well established protocol ISO 10678:2010 [5] of the international standards organization, the world's leading developer and publisher of international standards (counting a network of the national standards institutes of 162 countries). This standard propose the use of the Methylene blue (MB) dye, a very popular test pollutant in semiconductor photocatalysis, by measuring the rate of photocatalytic bleaching of the dye in aqueous solution via UV/vis spectrophotometry while the photocatalytic sample is immersed in the solution. The MB degradation process followed the pseudo first order kinetic law, by which we calculated the photocatalytic rate constant. In fact, plotting the log (C/Co), where C is the MB concentration and Co the MB initial concentration, versus the UV exposure time, the slope of the curve gives the rate constant. The photonic efficiency was also estimated as recommended in the ISO 10678:2010 document [5].

First we analyzed the photocatalytic activity of TiO_2 NWs on Ti foil, measuring the MB degradation on: TiO_2 foil with NWs grown at 800°C for 4h with a mixed flow of Ar at 10 lpm and O_2 at 7,5 lpm, namely the optimal growth conditions discussed in Chapter 2; TiO_2 foil with these same processed NWs and with an additional annealing in forming gas at 500°C for 2h, as discussed in Chapter 3; a TiO_2 reference foil without NWs, processed with the same annealing conditions of the NWs sample (a part from the gold deposited layer). Next, we analyzed the case of the Ti thin film substrate, performing MB measurement on TiO_2 NW_S grown on the thin film substarte, and for comparison reasons, on a reference substrate created using the Ti thin film treated with the same annealing process used to synthetize the NWs. Then, the MB degradation test was also applied to the sample of NWs grown on the nanospike substrate and, as a reference to the bare nanospike sample (without NWs).

A strong improvement in the photocatalytic activity due to the presence of the NWs was found in every case. The **Table 5.2** sum up the percentage of improvements obtained in the photocatalytic rate constant per unit area and in the photonic efficiency, for the different substrate cases. The photocatalytic rate constant of the samples with NWs is from 36% up to 67% higher than the one obtained from the corresponding substrates without NWs. whereas for the photonic efficiency these improvement values go from 25% up to 60%. A very important result is represented by the role of the forming gas annealing treatment in the NWs grown on Ti foil substrate. The treatment in forming gas doubled the photonic efficiency of the NWs sample compared to the one of the same substrate without NWs. Similarly, the photocatalytic rate constant was triplicated. In addition, these NWs samples with and without FG treatment, exhibited the same reflectance (**Fig.5.6**) at the same light wavelengths range of the employed UV source, thus the increased photocatalytic efficiency of the NWs sample annealed in forming gas should be related to intrinsic factors, such as extended carrier life-times, and not due to antireflective effects due to their morphology.

Table 5.2 – Sum up table of the improvement effect of the presence of NWs in the different analyzed samples, compared to the relative bare substrate, on the photocatalytic parameters (photonic efficiency and photocatalytic rate constant per unit area).

Sum up of the NWs effect on the photocatalytic parameters of the samples:	Improvement of the Photonic efficiency (ζ_{MB})	Improvement of the Photocatalytic rate constant per unit area (K/A)
TiO$_2$ foil + NWs	+25%	+67%
TiO$_2$ foil + NWs + FG	+78% (vs NWs) +100% (vs foil)	+58% (vs NWs) +200% (vs foil)
TiO$_2$ film + NWs	+60%	+50%
Nanospikes + NWs	+40%	+36%

Moreover, this increase in the photocatalytic activity after the forming gas annealing correlates also with the results obtained by deep level transient spectroscopy discussed in Chapter 4, that showed a disappearance of a deep level recombination centre that could have suppressed the catalytic effect of the photon-induced electron-hole pairs. It may be a defect of dangling bond character being passivated by hydrogen during the forming gas annealing.

We also investigated the effect of Fe$^+$ implantation into TiO$_2$ thin films of ~ 100 nm in thickness (already presented in Chapter 3) in terms of its photocatalytic activity in the degradation of MB under UV or VIS light irradiation. The iron doped film revealed a marked increase in the photomineralization efficiency under VIS light irradiation (80% higher than the one obtained for pure TiO$_2$ films), without the help of any additional thermal treatments. We demonstrated that the photocatalytic activity in the degradation of organic compounds strongly depends on the amount of defects induced by the ion-implantation process.

Finally, we reported a first antibacterial test performed on *E.Coli* bacterium. We measured the survival rate of *E. coli* after exposure to UV light activated TiO$_2$ samples. The antibacterial activity of nanostructured titania is higher with respect to thin TiO$_2$ film or typical bactericide as H$_2$O$_2$.

References

[1] Mills A., Lee S.K., J. Photochem. Photobiol. A: Chem., 152, 1–3 (2002) 233-247.

[2] ISO 22197-1: 2007, 'Fine ceramics, advanced technical ceramics – test method for air-purification performance of semiconducting photocatalytic materials – part 1: removal of nitric oxide', ISO, Geneva, 2007.

[3] ISO 27448: 2009, 'Fine ceramics, advanced technical ceramics – test method for self-cleaning performance of semiconducting photocatalytic materials – measurement of water contact angle', ISO, Geneva, 2009.

[4] ISO 27447: 2009, 'Fine ceramics, advanced technical ceramics – test method for antibacterial activity of semiconducting photocatalytic materials', ISO, Geneva, 2009.

[5] ISO 10678: 2010, 'Fine ceramics, advanced technical ceramics – determination of photocatalytic activity of surfaces in an aqueous medium by degradation of methylene blue', ISO, Geneva, 2010.

[6] ISO 10676: 2010, 'Fine ceramics, advanced technical ceramics – test method for water purification of semiconducting photocatalytic materials by measurement of forming ability of active oxygen', ISO, Geneva, 2010.

[7] ISO 10677: 2011, 'Fine ceramics, advanced technical ceramics – ultraviolet light source for testing semiconducting photocatalytic materials', ISO, Geneva, 2011.

[8] ISO 22197-2: 2011, 'Fine ceramics, advanced technical ceramics – test method for air-purification performance of semiconducting photocatalytic materials – part 2: removal of acetaldehyde', ISO, Geneva, 2011.

[9] ISO 22197-3: 2011, 'Fine ceramics, advanced technical ceramics – test method for air-purification performance of semiconducting photocatalytic materials – part 3: removal of toluene', ISO, Geneva, 2011.

[10] R.W. Matthews, J. Chem. Soc. Faraday Trans. 85 (1) (1989) 1291.

[11] Mills A., Hill C., Robertson P.K.J., J. Photochem. Photobiol. A: Chem., 237 (2012) 7-23.

[12] McNaught AD., Wilkinson A., *Compendium of Chemical Terminology, The "Gold Book", 2nd edition*. Oxford: Blackwell; 1997.

[13] Fàbrega C., Andreu T., Guell F., Prades J.D., Estradé S., Rebled J.M., Peirò F. and Morante J.R., Nanotechnology, 22 (2011) 235403.

[14] Wang G., Wang H., Ling Y., Tang Y., Yang X., Fitzmorris R. C., Wang C., Zhang J. Z. and Li Y., Nano Lett., 11 (2011) 3026-3033.

[15] Serpone N. and Salinaro A., Pure Appl. Chem. 71 (1999) 303.

[16] Anpo M. and Takeuchi M., J. Catal. 216, 505 (2003).

[17] Impellizzeri G., Scuderi V., Romano L., Sberna P.M., Arcadipane E., Sanz R., Scuderi M., Nicotra G., Bayle M., Carles R., Simone F. and Privitera V., J. Appl. Phys., Vol. 116, pp.173507, 2014.

Conclusions and outlooks

This thesis explored the synthesis of titanium dioxide nanowires by seed assisted thermal growth in the temperature range between 600-1000 °C. In order to improve the photocatalytic performances of TiO_2 NWs, we modified the samples applying two approach: doping by ion implantation of Fe^+ and annealing in forming gas (H_2 5% in N_2).

Annealing at temperature below 700°C revealed very rare and short NW_S. With increasing temperature, NWs grew in length and in density. At 1000°C a mechanism of micrograins growth appeared in competition with the NWs evolution. The NWs length increased with increasing the annealing time, while no relevant density change was observed up to 900°C, indicating that the nucleation occurs at 700°C. Concerning the annealing atmosphere, an increase in gas flow rates improved the nanowires coverage, while varying the mixture of Ar and O_2 did not give relevant changes. XRD measurements of the NWs revealed a TiO_2 rutile crystalline phase with a main peak of the (110) orientation. TEM analysis indicated that the NWs are pure TiO_2 monocrystalline. The *in situ* thermal growth in water vapor atmosphere at 800°C for about 2h, showed that the rate of NWs growth in length and density is higher in the first 20-40 minutes (length up to 10-20 µm); subsequently the oxidation rate decrease and the NWs tent to shorten and became wider in their base, creating a more wide rods/grains shapes (length of few µm). Therefore, at high temperature (1000°C) the surface mobility favours the 2D grain growth so we observed a decrease of NWs density. At low temperature (700°C), the nucleation process is activated but the growing rate is low so we observed very short NWs. At medium temperature (800°C) we got the best compromise. Since NWs are not nucleated without gas carrier (in vacuum) we can conclude that the nucleation mecanism cannot be only supported by the surface migration of Ti from the substrate but a certain amount of Ti has to be transported in the gas phase. Moreover, the uniformity of NWs coverage of the substrate improves when the gas carrier contains oxygen. This means that the formation of pure Ti NWs is not energetically or kinetically favoured in the full range of explored temperatures (600-1000 °C). According to this observation the Au-Ti phase diagram cannot be taken unto account to depict

the VLS mecanism with the help of eutectic alloys. Moreover, without catalyst the NWs growth is very difficult to be induced and controlled, only few NWs are observed in small isolated areas of the sample with no reproducibility. In conclusion, the seed assisted growth of TiO_2 NWs is a very complex synthesis mecanism, as it is assisted by Ti-Au interdiffusion, Ti migration, gas carrier transport and oxygen gas reaction.

We demonstrared that the same method of TiO_2 NWs growth can be applied to different type of Ti substrates, opening new possibilities for different kind of applications.

Fe^+ ion implantion induced an absorbance of ~ 12% for VIS light in TiO2 thin films, with an effective band-gap lowering from 3.2 eV to 1.6–1.9 eV, without the help of any additional thermal treatments. Implantation-induced defects formed energy levels inside the band-gap of the material, but it is crucial to keep their amount below a certain limit, as they act as recombination centres for electrons and holes. The same approach was extended to TiO_2 nanowires by tuning the ion implantation energy, NWs showed to change their morphology as a consequence of ion implantation damage by bending like in the case of ion hammering effect reported in literature for Si and Ge nanowires.

Four peaks were clearly resolved in DLTS spectra of samples with TiO_2 NWs, with energy level below the conduction band at $E_C - E_T$ respectively of: 0.11 eV, 0.30 eV, 0.45eV and >0.6 eV. The latter E_4 peak disappears in the spectrum of the samples of NWs treated with forming gas, which also exhibits a considerably higher amplitude of the shallow E_1 peak than the other samples, while the E_2, E_3 peaks are substantially weaker.
The identity of the E_1, E_2, E_3 and E_4 levels is not known and previous DLTS data in the literature on deep levels in TiO_2 NWs are scarce (if any). However, the loss of the E_4 level after the FG treatment can be correlated with the samples photocatalytic activity.

We assessed the photocatalytic activity of different TiO_2 NWs on various substrates by measuring the rate of photocatalytic bleaching of the MB dye in aqueous solution via UV spectrophotometry and the photonic efficiency. The MB degradation process followed the pseudo first order kinetic law, by which we calculated the photocatalytic rate constant. The photocatalytic rate constant of the samples with NWs is from 36% up to 67%

120

higher than the one obtained from the corresponding substrates without NWs. Whereas for the photonic efficiency these values go from 25% up to 60%.

A very important result is represented by the role of the forming gas annealing treatment. The treatment in forming gas doubled the photonic efficiency of the NWs sample compared to the one of the same substrate without NWs. Similarly, the photocatalytic rate constant was triplicated. In addition, these NWs samples with and without FG treatment, exhibited the same reflectance at the same light wavelengths range of the employed UV source, thus the increased photocatalytic efficiency of the NWs sample annealed in forming gas should be related to intrinsic factors, such as extended carrier life-times, and not due to antireflective effects due to their morphology. Moreover, this increase in the photocatalytic activity after the forming gas annealing correlates with the results obtained by deep level transient spectroscopy that showed a disappearance of a deep level (E_4) that could act as a competing charge carrier recombination center suppressing the catalytic effect of the photon-induced electron-hole pairs. It is tempting to make an association with a defect of dangling bond character being passivated by hydrogen during the FG annealing.

In conclusion, a general model of seed assisted growth is still lacking and our experimental results revealed a very complex interplay of several growth parameters, which is hard to disentangle without the help of theoretical understanding that allows to design the right experiment. Moreover, the observed relevance of defects, which can affect the light absorption in the VIS region or improve the photocatalytic efficiency, is still under debate and deserves a dedicated systematic study by employing several characterizations in order to identify the defect configuration and properties. The most difficult part is to translate a well tested characterization on bulk samples to nanostructured substrates. New measurements methodologies – some have been attempted here - have to be developed in order to specifically deal with nanostructures and producing significant data. Photocatalysis is a complex mechanism that is very difficult to characterize by disentangling secondary effects. Additional degradation rate analyses with different sensing molecules and correlated optical analyses, such as photoluminescence, are necessary for assessing the

photocatalytic efficiency of nanowires, and for clarifying the role of structural defects, recombination properties, water environment and nanostructured surface.

List of publications

- J. Bonkerud*, **E. Arcadipane*,** C. Bhoodoo, L. Vines, L. Romano, and B.G. Svensson, "Electrically active defects in TiO2 thin films and nanowires", to be submitted in Journal of Applied Physics.

- **E. Arcadipane**, R. Sanz, G. Amiard, G. Impellizzeri, V. Privitera, J. Bonkerud, C. Bhoodoo, L. Vines, B. G. Svensson and L. Romano, "Synthesis and characterization of Single-crystal TiO_2 Nanowires by seed assisted thermal oxidation of Ti", submitted in Nanotechnology.

- G. Impellizzeri, V. Scuderi, L. Romano, P.M. Sberna, **E. Arcadipane**, R.Sanz, M.Scuderi, G. Nicotra, M. Bayle, R. Carles, F. Simone and V. Privitera, "Fe ion-implanted TiO_2 thin film for efficient visible-light photocatalysis", J. Appl. Phys., Vol. 116, pp.173507, 2014.

- **E. Arcadipane**, R. Sanz, M. Miritello, G. Impellizzeri, M. G. Grimaldi, V. Privitera, L. Romano, "TiO_2 nanowires on Ti thin film for water purification", Materials Science in Semiconductor Processing, Available online 30 July 2015, ISSN 1369-8001.